

Constraining Hydrate-Mediated Transfer of the Greenhouse Gases CO₂ and CH₄ to the Ocean at Controlled Thermodynamic and Hydrodynamic Forcing

Dissertation
zur Erlangung des Doktorgrades
der Mathematisch-Naturwissenschaftlichen Fakultät
der Christian-Albrechts-Universität
zu Kiel



vorgelegt von
Nikolaus Bigalke

Kiel, 2008

Referent:Prof. Dr. Klaus Wallmann
Korreferent: Prof. Dr. Gregor Rehder
Tag der mündlichen Prüfung:21.11.2008
Zum Druck genehmigt:

Der Dekan

Hiermit erkläre ich, dass ich die vorliegende Doktorarbeit selbständig und ohne unerlaubte Hilfen erstellt habe. Ferner habe ich weder diese noch eine ähnliche Arbeit an einer anderen Abteilung oder Hochschule im Rahmen eines Prüfungsverfahrens vorgelegt, veröffentlicht oder zur Veröffentlichung vorgelegt.

Kiel, den 23.10.2008

Nikolaus Bigalke

Dank

Herrn Prof. Dr. Klaus Wallman möchte ich danken, dass ich diese Dissertation in der Arbeitsgruppe Marine Geosysteme am Leibniz-Institut für Geowissenschaften an der Universität Kiel anfertigen konnte.

Ganz herzlich danke ich Prof. Dr. Gregor Rehder, der in allen Phasen der Arbeit durch fachlichen Rat, Diskussionsbereitschaft und nicht zuletzt auch durch stete Motivation einen entscheidenden Anteil am Gelingen dieser Arbeit hatte. Dank auch an Prof. Dr. Giselher Gust, der die notwendigen Voraussetzungen für die Durchführung der Hochdruckexperimente schuf und die Arbeit mit Ideenreichtum und engagierter Diskussion sehr bereicherte.

Ohne die kompetente technische Unterstützung durch Andreas Meyer, Florian Michl und Klaus Wiczorek wäre der Betrieb des Drucklabors und somit die Datenakquise unmöglich gewesen. Ich bedanke mich herzlich für großartiges Engagement und die unkomplizierte Arbeitsatmosphäre. Die MitarbeiterInnen der genutzten analytischen Einrichtungen standen mir stets mit Rat und Tat zur Seite, insbesondere danke ich Karen Stange, Markus Faulhaber und Peggy Wefers.

Den "Anwohnern" der Lithothek danke ich für ihre Geduld und Toleranz den oft erhöhten Geräuschpegel bei Betrieb der Laborklimaanlage zu ertragen.

Jens Schneider möchte ich für fachliche Diskussionen, insbesondere für erhellende Lehrstunden zum Thema Hydroakustik danken. Darüber hinaus schulde ich ihm und all meinen anderen Freunden am IFM-GEOMAR dank für ein gutes Arbeitsklima und die vielen heiteren Momente der letzten dreieinhalb Jahre.

Meinen Eltern schulde ich großen Dank für das in mich gesetzte Vertrauen den eingeschlagenen Weg erfolgreich abzuschließen. Mein größter Dank gilt meiner Freundin Ruth, die mich trotz meiner Launenhaftigkeit, insbesondere während der Endphase dieser Arbeit, unermüdlich unterstützt hat: Danke!

Preface

This thesis consists of a general introduction (Chapter 1), and three stand-alone papers (Chapters 2 to 4). Each of the Chapters 2 to 4 contains a separate introduction, description of methods, presentation of data and discussion as well as a separate reference list. Chapter 3 has already been published by *Environmental Science & Technology*. Chapter 2 has been submitted to *Marine Chemistry* and Chapter 4 will be submitted to *Geophysical Research Letters*.

The titles and authors of the papers and manuscripts are briefly listed below:

Chapter 2	Methane hydrate dissolution rates in undersaturated seawater under controlled hydrodynamic forcing
Authors	N. K. Bigalke, G. Rehder, G. Gust
Status	submitted to <i>Marine Chemistry</i>
Chapter 3	Experimental investigation of the rising behavior of CO ₂ droplets in seawater under hydrate-forming conditions
Authors	N. K. Bigalke, G. Rehder, G. Gust
Status	published by <i>Environmental Science & Technology</i>
Chapter 4	Terminal velocities of pure and hydrate coated CO ₂ droplets and CH ₄ bubbles rising in a simulated oceanic environment
Authors	N. K. Bigalke, L. I. Enstad, G. Alendal, G. Rehder, G. Gust
Status	in preparation for <i>Geophysical Research Letters</i>

I contributed to these papers as follows: acquisition and processing of all experimental data, interpretation and graphical presentation of the data, writing and preparation of the manuscripts.

Contents

Kurzfassung	xv
Abstract	xix
1 Introduction	1
1.1 Methane and carbon dioxide in the system of the earth	1
1.1.1 Physical properties of methane and carbon dioxide and their role in the atmosphere	1
1.1.2 Evolution of atmospheric methane and carbon dioxide con- centrations in the Phanerozoic	1
1.1.3 Methane and carbon dioxide in recent times: sources, sinks and risks	3
1.2 Clathrate hydrates of methane and carbon dioxide	5
1.2.1 Structure and stoichiometry	5
1.2.2 Methane	6
1.2.3 Carbon dioxide	9
References	14
2 Dissolution of methane hydrate in undersaturated seawater	25
Abstract	25
2.1 Introduction	26
2.2 Dissolution theory	28
2.3 Experimental set-up and procedure	31
2.4 Results	35
2.5 Discussion	38
2.5.1 Mass transfer	38
2.5.2 Pure gas dissolution experiments	40
2.5.3 Validity of experimental approach	41

2.5.4	Comparison to earlier data and postulations	42
	Implications	43
	Acknowledgments	44
	References	44
3	Rising behavior of CO₂ droplets in seawater	49
3.1	Introduction	50
3.2	Experimental set-up and procedure	52
3.3	Results and Discussion	53
3.3.1	Droplet shape and motion characteristics	53
3.3.2	Rise velocity	56
3.3.3	Behavior of non-hydrate coated droplets	59
	Acknowledgments	62
	References	62
4	Terminal velocity of pure and hydrate coated particles	65
4.1	Introduction	66
4.2	Experimental	69
4.2.1	CO ₂ droplets	69
4.2.2	CH ₄ bubbles	69
4.3	Mathematical Approach	71
4.4	Discussion	75
4.4.1	CH ₄ Bubble Data	75
4.4.2	Data Simulations	76
4.5	Summary	79
	Acknowledgments	79
	References	80
A	Supporting Information to Chapter 2	85
A.1	Preparation of the experiments	85
B	Supporting Information to Chapter 3	87
B.1	Description of experimental set-up and mode of operation	87
B.2	Image analysis	89
B.3	Aspect ratios of droplets rising within the field of hydrate stability.	90
	References	90

List of Tables

2.1	Properties of seawater at experimental conditions.	32
2.2	C_{sat} and k_d as determined from dissolution experiments.	38
3.1	Experimental P -/ T -conditions and corresponding liquid CO_2 and seawater densities.	53
4.1	E_o and M_o of CH_4 bubbles and CO_2 droplets.	74

List of Figures

1.1	Phase diagram of CO ₂ , CH ₄ and seawater.	6
1.2	Options of CO ₂ sequestration by direct ocean storage.	11
2.1	Sketch of the microcosm used in CH ₄ hydrate dissolution experiments.	31
2.2	CH ₄ solubilities in seawater.	34
2.3	Shift of the optical appearance of hydrate during a typical dissolution experiment.	36
2.4	Transfer of CH ₄ into seawater from dissolving CH ₄ hydrate.	37
2.5	Transfer of CH ₄ into seawater across a pure gas/seawater interface. .	39
2.6	k_d/u^* -correlation determined from CH ₄ hydrate dissolution.	40
2.7	z/u^* -correlation determined from CH ₄ hydrate dissolution.	40
3.1	Phase diagram of CO ₂ and seawater.	51
3.2	Aspect ratio of CO ₂ droplets.	54
3.3	Spreading of a hydrate skin around a CO ₂ droplet.	55
3.4	u_T of CO ₂ droplets rising at hydrate forming conditions.	57
3.5	Comparison of u_T of hydrate-coated and pure liquid CO ₂ droplets. .	60
4.1	Phase diagram of seawater, CH ₄ and CO ₂	67
4.2	u_T and aspect ratios of CH ₄ bubbles.	70
4.3	Comparison of parameterized and observed rise velocities of hydrate coated and pure liquid CO ₂ droplets.	77
4.4	Comparison of parameterized and observed rise velocities of CH ₄ bubbles.	78
B.1	Schematic diagram of the inner assembly.	88
B.2	Aspect ratios of droplets rising within the field of hydrate stability. .	90

Kurzfassung

Methan und Kohlendioxid bilden im Ozean bei Druck und Temperaturbedingungen in wenigen hundert m Wassertiefe Struktur-I Klathrat-Hydrate (auch: Gashydrate). Unter hydratbildenden Bedingungen werden Freisetzung und Wanderung der o.a. Gase in bzw. durch die Wassersäule durch die thermodynamische und kinetische Stabilität der Gashydrate beeinflusst. Ein besseres Verständnis der Stabilität von Gashydraten sowie des hydratbeeinflussten Transfers der beiden wichtigsten Treibhausgase in den Ozean ist essentiell um den Beitrag submariner Methanquellen auf den Klimawandel, um das Gefahrenpotential submariner Hydratvorkommen für die immer wichtiger werdende Offshore-Produktion von Öl und Gas sowie um Durchführbarkeit und Umweltbeeinflussung durch Einlagerung anthropogenen Kohlendioxids in den marinen Raum besser abschätzen zu können.

Die vorliegende Arbeit beschäftigt sich mit der laborgestützten Untersuchung des hydratkontrollierten Transfers beider Gase in den Ozean. Zu diesem Zweck wurden Experimente durchgeführt, um bestehende Unsicherheiten bezüglich Hydratbildung und -zersetzung in der bodennahen Grenzschicht sowie des hydratkontrollierten Transports in der Wassersäule auszuräumen bzw. einzugrenzen.

Zur Simulation der abyssalen Umweltbedingungen wurde ein Druckbehälter eingesetzt, in dem der gewählte experimentelle Aufbau autoklaviert werden konnte. Das System ermöglichte Untersuchungen bei Druck- und Temperaturbedingungen von maximal 40 MPa und minimal 1 °C. Abhängig von der Fragestellung und dem jeweiligen experimentellen Aufbau konnten somit marine Bedingungen bis in eine Wassertiefe von etwa 4000 m simuliert werden.

In Kapitel 2 dieser Arbeit wird die Stabilität von Methanhydrat anhand von Experimenten bei P -/ T -Koordinaten innerhalb des thermodynamischen Stabilitätsfeldes in Anwesenheit von an Methan untersättigtem Salzwasser untersucht. Die Untersuchung erforderte die Simulation der Umweltbedingungen, unter denen

natürliche Gashydrate an der Sedimentoberfläche in der Tiefsee anstehen. Neben den notwendigen Druck- und Temperaturbedingungen erforderte die Simulation die Erzeugung eines homogenen Strömungsfeldes an der Hydrat/Wasser Grenzschicht. Es wurde beobachtet, dass die Geschwindigkeit der Hydratlösung durch untersättigtes Wasser bei P -/ T -Bedingungen im Hydratstabilitätsfeld ausschließlich von der Geschwindigkeit der tangential an die Hydratoberfläche angelegten Strömung des Wassers abhängig ist. Dies zeigt, dass unter den genannten Bedingungen die Lösung von Methanhydrat von der Diffusion der Methanmoleküle abhängig ist und nicht etwa von der Desorptionsrate der Methanmoleküle aus dem Hydratkristallverband. Ferner ist unter den genannten Bedingungen der Massentransfer von Methan aus sich zersetzendem Methanhydrat proportional zur Differenz aus Hintergrundkonzentration und der durch P , T und S kontrollierten Sättigungskonzentration im Salzwasser. Mit Hilfe der Ergebnisse wurde eine Korrelation des Massentransferkoeffizienten und der Reibungsgeschwindigkeit gefunden, die bei bekannten Konzentrationsdifferenzen eine präzise Berechnung der Lösungsgeschwindigkeiten für beliebige natürliche P , T , S und Bodenwasserströmungen von direkt an der Sedimentoberfläche anstehenden planaren Methanhydraten ermöglicht. Die gefundene Beziehung erlaubt ferner die Abschätzung der minimalen Hydratbildungsrate, die für den Erhalt von unregelmäßig geformten, an der Sedimentoberfläche anstehenden Methanhydraten notwendig ist.

Kapitel 3 widmet sich der Untersuchung der Aufwärtsbewegung hydratummantelter, flüssiger CO_2 Tropfen in synthetischem Meerwasser bei Druck- und Temperaturbedingungen entlang eines natürlichen, ozeanischen Hydrotherms. Der umfangreiche, experimentelle Datensatz erlaubte die eindeutige Validierung einer gängigen Parametrisierung des Strömungswiderstandskoeffizienten hydratummantelter CO_2 Tropfen. Vergleichsexperimente außerhalb des Hydratstabilitätsfeldes zeigten, dass Tropfen ohne Hydrathaut um bis zu 50% schneller aufsteigen als hydratummantelte Tropfen gleicher Größe. Entgegen Beobachtungen in natürlicher Umgebung konnte ein ähnlicher Effekt auch für Methanblasen beobachtet werden (s. hierzu Kapitel 4). Die Fälle ausbleibender Hydratbildung um CO_2 Tropfen und die infolgedessen erhöhten registrierten Steiggeschwindigkeiten nahmen innerhalb des Hydratstabilitätsfeldes mit Annäherung an die Phasengrenze zu. Dies dürfte sowohl Lebensdauer als auch zurückgelegte Wegstrecke einzelner

Tropfen signifikant beeinflussen und sollte in künftigen Modellen zur Risikoabschätzung von marinen Sequestrierungsvorhaben berücksichtigt werden.

Gegenstand von Kapitel 4 ist die Entwicklung einer allgemeingültigen Parametrisierung des Strömungswiderstandskoeffizienten hydratummantelter CO_2 Tropfen (Kapitel 3) und CH_4 Bläschen. Die Parametrisierung beruht auf physikalischen Grundsätzen zur Charakterisierung der Tropfen- bzw. Blasenform und erlaubt die Vorhersage der Steiggeschwindigkeiten für ein Größenintervall zwischen 0 und 1 cm Radius bei beliebigen ozeanischen P -/ T -Bedingungen. Unter Einbezug existierender Modelle zur Lösungskinetik ermöglicht sie die präzise Berechnung vertikaler Laufstrecken einzelner, hydratummantelter Blasen/Tropfen, die für eine quantitative Abschätzung der vertikalen Verteilung der jeweiligen Gase nach ihrer Freisetzung in der Wassersäule notwendig ist.

Die vorliegende Arbeit kann die Ausbreitung von Methan und Kohlendioxid im Ozean nicht allumfassend behandeln. Speziell die Vorgänge, die zur Verteilung der Gase im dreidimensionalen Raum führen, bleiben unberührt. Die Arbeit liefert jedoch Validierungsdaten für jene Modellierbereiche, die für eine Bilanzierung des vertikalen Transfers der beiden wichtigen klimarelevanten Gase CH_4 und CO_2 von der Sediment/Wasser Grenzschicht bis ins Oberflächenwasser und damit in die Atmosphäre in Frage kommen.

Abstract

Pressures and temperatures prevailing in the ocean at a few hundred meters depth cause methane and carbon dioxide to form structure-I clathrate hydrates (or simply gas hydrates). At these conditions release and migration of methane and carbon dioxide into and within the water column are significantly influenced by the thermodynamic and kinetic stability of gas hydrates. A better understanding of hydrate stability and the hydrate-mediated transfer of the two most important greenhouse gases to oceanic waters is essential to assess the contribution of submarine methane seepage to climate change, the hazard potential of submarine gas hydrate deposits to ever-increasing offshore drilling activities for oil and gas and the feasibility and environmental impact of anthropogenic carbon storage in the marine environment.

The present survey deals with laboratory-based investigations of hydrate-controlled transfer and transport processes of the two gases in the ocean. The experiments conducted aimed at constraining hydrate formation and -decomposition at the sediment/seawater interface as well as at constraining hydrate-controlled motion characteristics of methane bubbles and carbon dioxide droplets in an oceanic water column.

The objective of the experiments required simulation of deep-sea conditions as closely as possible. These were realized inside a thermostatted pressure vessel equipped with an inner assembly specifically designed to meet experimental demands. The system allowed investigations at pressures of up to 40 MPa and temperatures as low as 1 °C, enabling simulation of marine conditions at seawater depth of up to 4000 mbsl.

Chapter 2 presents results of investigations concerning the stability of methane hydrate in seawater strongly undersaturated with methane, yet at P -/ T -conditions within the hydrate stability field. The investigation required simulation of conditions under which natural gas hydrates outcrop the sea-floor surface at depth.

Thus, apart from establishing necessary pressure and temperature conditions, a homogeneous and adjustable flow field at the interface of newly formed methane hydrate and seawater was generated. The experiments show that inside the hydrate stability field the dissolution rate of methane hydrate is exclusively dependent on the velocity of the undersaturated seawater flowing tangentially across the hydrate surface. This shows that at aforementioned conditions dissolution of methane hydrate is controlled by the diffusive flux of methane molecules off the hydrate/seawater interface and not by the rate methane (and water) molecules desorb from the hydrate crystal. Furthermore it was noted that the mass transfer of methane from decomposing methane hydrate is proportional to the concentration difference of methane in bulk seawater and the saturation concentration governed by pressure, temperature and salinity. The data thus yield a correlation of mass transfer coefficients and flow velocities, which may be used to accurately calculate dissolution rates of clean, planar methane hydrate surfaces for any P , T and S conditions encountered in a natural setting. It also provides a means to estimate the minimum rate of reformation needed to maintain irregularly shaped hydrate outcrops at the seafloor.

In Chapter 3 an extensive data set on the upward motion of hydrate-forming, liquid CO_2 is presented and analyzed. Rise velocities of CO_2 droplets in synthetic seawater were obtained for a variety of pressures and temperatures along a simulated oceanic hydrotherm. The data validated an empirical parameterization of the drag coefficient developed to suit hydrate-coated CO_2 droplets. Inter-comparison experiments outside the field of hydrate stability revealed that droplets without a hydrate coating rise up to 50% faster than their equally sized hydrate-coated counterparts. In contrast to observations made in a natural setting, a similar effect could be observed for methane bubbles, as discussed in Chapter 4. Within the hydrate stability field, the number of droplets failing to develop a hydrate skin increased as P -/ T -conditions approached hydrate phase equilibrium. The enhanced velocity of these droplets significantly affects both lifetime and vertical distance traveled. This finding should be taken into consideration in future models aiming at assessing feasibility and risk of fossil fuel derived CO_2 storage in the oceanic environment.

Chapter 4 details the development of a drag parameterization suitable to predict the rise velocity of both methane bubbles and CO_2 droplets within their respective hydrate stability fields. The parameterization presented relies on physical princi-

ples and may be used to assess both shape and friction of hydrate-coated particles of 0 to 1 cm radius for almost any oceanic P -/ T -conditions. Validation of the theory is provided by the data gained in Chapter 3 as well as by rise rates of hydrate-coated methane bubbles presented in Chapter 4. Coupled with theories adequately describing dissolution of hydrate-coated CO_2 droplets or methane bubbles, the parameterization allows predicting bubble and droplet lifetime, which is necessary to quantitatively assess the vertical distribution of the respective gas after its release to the water column.

The present investigation cannot provide an entire treatment of the mechanisms governing migration of methane and carbon dioxide in the water column. The mechanisms responsible for spreading the gases in three dimensions in particular are not addressed. The investigation rather stresses the importance of water column processes on the fate of gases released at the sediment/seawater interface and fills a gap in the data basis needed to model the balance of the vertical transfer of the two most important greenhouse gases in the ocean.

1 Introduction

1.1 Methane and carbon dioxide in the system of the earth

1.1.1 Physical properties of methane and carbon dioxide and their role in the atmosphere

Atmospheric carbon dioxide (CO₂) and methane (CH₄) are two of the most important gases that influence the radiation budget and consequently the climate of the earth. Due to human activity, the atmospheric concentrations of CO₂ and CH₄ have increased from pre-industrial values of 280 ppmv and 0.75 ppmv to a recent (2005) 379 and 1.78 ppmv, respectively (Forster et al., 2007). In the recent atmosphere, the climate forcing of CH₄ exceeds that of CO₂ by a factor of 26 on a mole-per-mole basis (Lelieveld and Crutzen, 1992). Hence, out of a total radiative forcing change of 2.63 W m⁻² (relative to the start of the industrial era) from all long lived greenhouse gases combined, the contribution from CH₄ is 0.48 W m⁻² compared to 1.66 W m⁻² from CO₂ (Forster et al., 2007). It is therefore extremely likely that the increase in atmospheric CO₂ and CH₄ since the beginning of the industrial revolution around 1750, human activities have contributed substantially to the presently registered warming of the global climate.

1.1.2 Evolution of atmospheric methane and carbon dioxide concentrations in the Phanerozoic

Atmospheric greenhouse gas concentrations have varied on all time scales throughout the history of the earth. The long-term evolution of atmospheric greenhouse gases during the Phanerozoic is poorly constrained for lack of direct geological evidence. In case of CO₂, there is evidence for very high concentrations (>3000 ppmv) in periods between 570 and 400 Ma and between 200 and 150 Ma BP (Berner, 1997, and references therein). The net effect of the balance between sources and sinks throughout the Phanerozoic has been to reduce concentrations of atmospheric CO₂

to the low pre-industrial levels (for a detailed discussion of the evolution of atmospheric CO₂ during the Phanerozoic consult, for example, Berner, 2006). On a multi-million year time scale CO₂ concentrations are determined by the balance of sinks like silicate rock weathering with subsequent inorganic carbon burial in calcareous sediments, burial of organic matter and sources like aerobic oxidation of organic matter, its thermal breakdown via diagenesis and thermal breakdown of carbonates by magmatic and metamorphic processes (Berner, 2001). Natural sources of atmospheric CH₄ are wetlands, plants, termites, oceans and volcanic emissions (Etiope and Milkov, 2004; Keppler et al., 2006). The most important sink is the troposphere, in which CH₄ is oxidized to CH₃ by OH radicals. Minor removal of atmospheric CH₄ is due to oxidation in soils as well as to reaction with Cl in the marine boundary layer. While most sources of atmospheric CH₄ have probably been identified, their source strengths are not well quantified due to the high variability of individual sources (Ehhalt et al., 2001). In an attempt to reconstruct the evolution of atmospheric *p*CH₄ during the Phanerozoic, Bartdorff et al. (2008) developed a model focusing mainly on biological methane sources. Since wetlands are considered to be the strongest natural source of methane (Etiope and Milkov, 2004), Bartdorff et al. (2008) propose high *p*CH₄ levels for periods in which large continental areas were covered by wetlands: 10 ppmv during the Carboniferous and 1.5 ppmv during the Jurassic and Cretaceous periods. The model does not consider effects from sudden, large-scale dissociation of massive amounts of CH₄ hydrates. These events are held responsible for negative δ¹³C anomalies in marine sediments of the Early Toarcian and Aptian (Hesselbo et al., 2000), the Late Paleocene (Dickens et al., 1995) and the Late Pleistocene (Kennett et al., 2000) and might have transferred a large amount of CH₄ into the atmosphere, causing a rapid warming of the climate by radiative forcing (Dickens et al., 1995; Kennett et al., 2003).

More recent geological records suggesting a close link between atmospheric temperatures and greenhouse gas concentrations are provided by Antarctic ice cores recording climate history of the past 420 ka. There is a close correlation between CH₄ and CO₂ concentrations in the air entrapped in vesicles in the ice and δ*D*_{ice}, a proxy for the local temperature (Petit et al., 1999). At the low temperatures of glacial periods CH₄ and CO₂ concentrations were low (0.32, 180 ppmv, respectively) while during the warmer interglacials concentrations rose to 0.77 and 300 ppmv, respec-

tively (Petit et al., 1999). Glacial/interglacial cycling is driven by the Milankovic cycles (i.e. the periodicities of the orbital parameters precession, obliquity and eccentricity; Imbrie et al., 1992). While greenhouse gases can act as strong amplifiers of the orbital forcing (Shackleton et al., 2000), the mechanisms for fluctuations in atmospheric greenhouse gas concentrations remain controversial (for a discussion cf. Prentice et al., 2001). During the past 10 ka (until the start of industrial activities in 1750 AD, of course), greenhouse gas concentrations in the atmosphere varied between 260 and 280 ppmv CO₂ and around 0.65 ppmv CH₄ (Denman et al., 2007; Dlugokencky et al., 2003). Since 1750, the growth rate of both gases increased dramatically in the atmosphere. Of the 600 Tg of CH₄ estimated to be currently emitted to the atmosphere per year, some 60% are derived from anthropogenic sources (Ehhalt et al., 2001). Major anthropogenic contributions are from rice agriculture, livestock, landfills, waste treatment, biomass burning, fossil fuel production and -combustion (Denman et al., 2007). Despite a large variability, the growth rate has recently been decreasing from peak values of about 0.014 ppmv a⁻¹ at the beginning of the 1980s to around zero from 1999 to 2005 (Dlugokencky et al., 2003). The reason for the decline is not fully understood although the quasi-stable concentration of the most significant sink (OH radicals in the atmosphere) indicates a recent stabilization of the emissions (Forster et al., 2007).

1.1.3 Methane and carbon dioxide in recent times: sources, sinks and risks

In the 10 years from 1995 to 2005 the CO₂ concentration increased by about 19 ppmv. This is the highest average growth rate recorded for any decade since direct atmospheric CO₂ measurements began in the 1950s (Forster et al., 2007). The increase in global atmospheric CO₂ since the industrial revolution is mainly due to CO₂ emissions from the combustion of fossil fuels, deforestation and cement production. After entering the atmosphere, CO₂ is rapidly taken up by the terrestrial biosphere or dissolves into the surface ocean from where it is eventually transferred into the deep ocean. Thus, atmospheric concentrations currently increase at about 55% of the rate of fossil fuel emissions, which in the period between 2000 and 2005 total on average 7.2 Pg C a⁻¹ (Denman et al., 2007).

The addition of CO₂ to the ocean results in a reduction of the ocean's capacity to buffer an increasing concentration of H⁺ ions and consequently, in the acidification

of the ocean water. This leads to a decrease in the saturation state of CaCO_3 , which might inhibit the production of carbonate shells by calcifying organisms (Orr et al., 2005; Riebesell et al., 2000). The surface pH of contemporary ocean water ranges from 7.9 and 8.25 (Royal Society, 2005). Ecological changes due to the expected decrease in pH may be severe for corals in tropical and cold waters (Gattuso et al., 1999; Kleypas et al., 1999; Langdon et al., 2003; Roberts et al., 2006) and for pelagic organisms (Tortell et al., 2002; Royal Society, 2005). Since the beginning of the industrial revolution, sea surface pH has dropped by about 0.1 pH units to 7.9. If the trend continues, the ocean pH is expected to decrease within a few centuries to a value estimated to have last occurred a few hundred million years ago (Caldeira and Wickett, 2003; Key et al., 2004).

The present-day concentrations of atmospheric methane and carbon dioxide exceed the pre-industrial values by factors of 1.4 in the case of CO_2 and 2.5 in the case of CH_4 . For both gases, these concentrations are unprecedented in the last 650 ka (Spahni et al., 2005; Siegenthaler et al., 2005). Pearson and Palmer (2000) in fact infer that today's CO_2 concentrations have not been exceeded during the past 20 Ma (Prentice et al., 2001). Based on different drivers such as demographic development, socio-economical development and technological changes, the Intergovernmental Panel on Climate Change (IPCC) developed a set of emission scenarios to estimate emission rates and greenhouse gas concentrations in the atmosphere until the year 2100 (IPCC, 2005). While all scenarios predict rising emissions until 2050 at least, annual emissions at the end of the century are estimated to range between 50% and 250% of current rates. However, the emissions growth rate since the beginning of this century, is higher than even the most fossil-fuel intensive emission scenario of the IPCC (A1F1) predicts for the same period of time (Rau-pach et al., 2007). Depending on the scenario, a stabilization to CO_2 concentrations between 450 and 750 ppmv requires the prevention of emissions in the order of 10^2 - 10^3 Gt CO_2 (IPCC, 2005).

Although presently the ocean is a net sink rather than a source for atmospheric CO_2 and the recent contribution of CH_4 from the ocean into the atmosphere is estimated to be only 4% (Wuebbles and Hayhoe, 2002) of the total input, the radiative forcing of greenhouse gases in the current atmosphere and its expected increase within the 21st century add to the concern that the coherent rise of atmospheric and ocean temperatures will lead to a destabilization of a significant portion of the present gas

hydrate inventory (cf. Section 1.2) and thus to a massive expulsion of greenhouse gases from the ocean to the atmosphere.

1.2 Clathrate hydrates of methane and carbon dioxide

1.2.1 Structure and stoichiometry

Gas hydrates are ice-like, non-stoichiometric compounds of water and certain guest molecules (GM). The guest molecules are incorporated in cavities of a framework structure of hydrogen-bonded H₂O molecules. Gas hydrates are also known as clathrate hydrates, or simply clathrates, the name of which is derived from the popular depiction of the polyhedral cavities hosting the guest molecules (*clatratus* (lat.) = cage). Natural gas hydrates crystallize in two, possibly three structure types: two cubic structures, sI (space group Pm $\bar{3}$ m, CsCl structure type) and sII (Fd $\bar{3}$ m, diamond structure type) and a hexagonal sH structure (P6/mmm), whose existence depends on the abundance of small and very large guest molecules in a certain mixing ratio. The structure type in general is determined by guest molecule species, cage occupancy, mixing ratio of the different guest species in the compound and sometimes formation conditions. Both, CH₄ and CO₂ crystallize in the sI structure if the gas or liquid is not significantly contaminated by other possible guests. The sI structure offers two different cage types: a smaller pentagonal dodecahedron and a larger tetradecahedron. Both cages may be occupied by either a CH₄ or a CO₂ molecule, although the guests typically show a preference for the larger cage. A unit cell of the sI structure type offers two small and six large cages and furthermore accompanies 46 H₂O molecules in a total cell volume of 12³ Å³. This yields an ideal unit cell formula of 1 GM · 5.75 H₂O and a density of 918.7 kg m⁻³ for ideal CH₄ and 1134 kg m⁻³ for ideal CO₂ hydrate. Thus, a volume of 1 L of ideal CH₄ hydrate contains 172 L CH₄ gas (STP). However, real hydrate crystals have more H₂O molecules per GM than dictated by the ideal unit cell formula. De Roo et al. (1983) for instance determined a H₂O/CH₄ ratio as high as 7.4. The cage occupancy is strongly influenced by *P*, *T* and the guest composition and may be determined by enthalpy differences around the ice point and the Clausius-Clapeyron equation (Handa, 1986).

1.2.2 Methane

Gas hydrate occurrence in nature

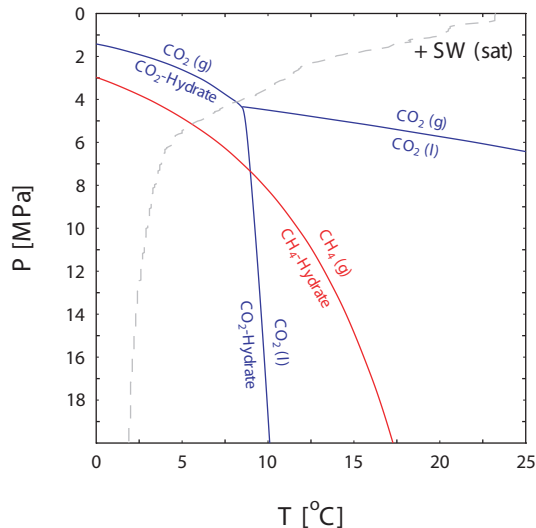


Figure 1.1: Phase diagram of CO_2 (blue lines), CH_4 (red lines) and seawater ($S=35$) saturated with respect to either one of the two gases. Dashed line delineates a P -/ T -profile in the Pacific Ocean at 35°N , 142°E (Schlitzer, 2007). Phase boundaries calculated after Sun and Duan (2005).

Natural gas hydrates are stable at low temperatures and high pressures. This stability constraint limits the occurrence of marine gas hydrates to continental permafrost environments and deep-sea sediments. Since the main guest species in most marine gas hydrates is biogenic CH_4 , hydrates are typically found in regions with high accumulation rates of organic carbon such as continental shelves or enclosed seas. Methane is also the dominant constituent of gas hydrates of thermogenic origin but in contrast to biogenic hydrates, these may also contain significant proportions (up to 40%) of higher hydrocarbons (Brooks et al., 1986; Ginsburg and Soloviev, 1994), enough to

stabilize sII structure hydrates. The phase diagram for CH_4 hydrate in Figure 1.1 illustrates that in mid latitudes water depths of at least 500 m are necessary to stabilize CH_4 hydrates in the marine environment. In most marine settings, gas hydrates are deeply buried and finely dispersed in (on average 3.5% of; Klauda and Sandler, 2005) the pore space of sediments. As a rule of thumb, the sediment cover can be estimated to be ten times as thick as the depth where dissolved CH_4 is converted to carbonate by anaerobic oxidation of CH_4 (Paull et al., 2005). Exceptions have been identified at locations where the flux of CH_4 from below is high enough to maintain hydrates near or even at the immediate seafloor surface (e.g. Ginsburg and Soloviev, 1998; Suess et al., 2001; MacDonald et al., 1994; Ginsburg et al., 1992; Chapman et al., 2004; Ginsburg et al., 1993; Brooks et al., 2000). Estimations of the global inventory of hydrate fixed CH_4 are not well defined.

On average, estimations had to be corrected downward continuously since natural

gas hydrates were first reported in 1965 (Makogon, 1965). However, even according to the more conservative estimations recently published (Soloviev, 2002; Milkov, 2004), gas hydrates hold more hydrocarbon energy than all other conventional gas reserves combined. For this reason, gas hydrates have aroused considerable interest in energy, climate and geohazard related issues.

Methane oxidation and transport

Enhanced discharge of methane-rich fluids at high intensity submarine seep sites (such as those where surface-near gas hydrates have been located) may generate plumes of methane-rich seawater hundreds of meters in height and several kilometers wide (Suess et al., 1999). At water depths inside the hydrate stability field, even in anoxic waters, dissolved CH_4 is usually oxidized before reaching the water-atmosphere interface (Boetius et al., 2000). Rising bubbles of free CH_4 gas may bypass microbial consumption in the sediment as well as in the water column and provide a means to transport the greenhouse gas even to surface waters and the atmosphere (Sauter et al., 2006). Gas hydrate skins crystallizing at the bubble interface during the rise have been shown to considerably impede bubble dissolution, thereby increasing the ease for bubbles to reach shallow water depths relative to bubbles without hydrate coatings (Rehder et al., 2002). McGinnis et al. (2006) detect exceptionally high bubble plumes (1300 m) in the Black Sea, attributing bubble longevity to the presence of hydrate skins. Assessing what fraction of the methane emitted on the seafloor reaches the atmosphere thus requires a detailed understanding of the nature of the hydrate skin. Despite the wealth of field observations (of which only a few have been cited here) and complementary laboratory studies (such as Maini and Bishnoi, 1981), the exact nature of the skin, the conditions under which it forms and its influence on mass transfer and bubble hydrodynamics is not well understood. With respect to the latter the data presented in Chapter 4 fills a knowledge gap by clearly highlighting the influence of the hydrate skin on bubble motion in oceanic waters.

Economic potential of natural hydrate reservoirs

The production of hydrocarbon gas from hydrates has so far been realized only in two locations. Both are located in permafrost environments of northern Siberia

and northern Canada (Messoyakha and Mallik gas hydrate fields, respectively). Due to the generally fine dispersal of methane hydrate in ocean sediments (3.5%, Klauda and Sandler, 2005) the cost of tapping marine hydrates is currently too high to warrant gas production on a large scale. However, easily accessible conventional gas reserves continue to deplete. The growing uncertainty of furnishing the rising demand of natural gas in future has motivated a number of emerging and established economies (Japan, South Korea, China, India) to initiate extensive support programs aiming at the large-scale extraction of hydrocarbon gas from marine hydrate deposits within a time frame of 10 years from now.

Marine gas hydrates as a geohazard

Marine slumping has been discussed as a mechanism to transfer CH_4 both fixed in gas hydrates as well as free gas bubbles toward surface waters and also the atmosphere (Kvenvolden, 1999; Paull et al., 2003). Slope failures arise at locations where high sedimentation rates pile up instable sedimentary columns. Slope failures can be triggered for example by earthquakes or gas hydrate destabilization following rising water temperatures or falling sea levels (Kvenvolden, 1999). The Storegga Slide in the Norwegian continental margin is a submarine landslide presumably caused by gas hydrate destabilization following rising ocean temperatures (Vogt and Jung, 2002; Sultan et al., 2004). With a swath stretching half-way from Norway to Greenland, the site is one of the largest submarine landslides exposed in the ocean. Based on a hydrate content of 10% of the pore volume, Paul (1978) estimated a release of 5 Gt CH_4 -carbon to the atmosphere. Archer (2007) attests CH_4 release following submarine land slides in general a significant but not "apocalyptic" effect on the climate. However, submarine slope failures leading to debris flows, slumps, slides, and possible tsunamis are an immediate threat on local and regional scale. As seabed resources in ever-deepening waters of coastal oceans become more and more attractive to exploit, the vulnerability of gas hydrate to temperature and sea level changes enhances the risk for human activities and installations in these settings.

Role of gas hydrates in climate change

The rise of deep water temperatures in the oceans to levels high enough to destabilize marine gas hydrates similar to those events inferred for the LPTM (Dickens et al., 1995) or the Late Quaternary interstadials (Kennett et al., 2003) is a common concern. Since the current ocean is colder than during the Paleocene, it is very likely that the current gas hydrate reservoir is larger than during any time of the Paleocene (Buffett and Archer, 2004). Destabilizing a fraction as little as 10% of a hydrate reservoir holding 5000 Gt CH₄-carbon within a timescale of a few years would have an impact on the earth's radiation budget equivalent to a factor of 10 increase in atmospheric CO₂ (Archer, 2007). Considering that the time scale for the release of CH₄ into the atmosphere at the LPTM was on the order of 10³ a, the occurrence of a scenario like the aforementioned is not likely. In fact, since oceans are deeper today than during the LPTM, the recent deep marine hydrate reservoir is better insulated against atmospheric warming and therefore even less prone to destabilization than during the end of the Paleocene (Dickens, 1999). Recent gas hydrate deposits responding more directly to the current rise of atmospheric temperatures are located in shallow seawater depths or terrestrial permafrost environments in or close to the Arctic. A recent example for the release of CH₄ from deposits like these is observed along the northern coastline of Siberia (Shakhova et al., 2005). The emission rates of CH₄ from these terrestrial or shallow marine hydrate deposits are much lower than necessary to cause the catastrophic greenhouse effect arising from an abrupt and massive expulsion of hydrate-CH₄ (Archer, 2007). However, even if not catastrophic, the emissions are likely to cause an increase in the steady-state concentration of CH₄ in the atmosphere, adversely influencing atmospheric temperatures on the long term. Finally, perturbations such as the LPTM serve as an analogue for understanding how the global carbon cycle and coupled systems respond to a release of carbon as massive as the current combustion of fossil fuels accounts for.

1.2.3 Carbon dioxide

Occurrence of CO₂ hydrates in nature

The occurrence of natural hydrates hosting CO₂ as dominant guest molecule is restricted to submarine vent sites of CO₂-rich fluids. Venting of these fluids is anec-

dotal and associated with seafloor hydrothermal systems. CO₂ droplet seepage has been identified in the Okinawa Trough, between Taiwan and the island of Okinawa (Shitashima et al., 2008; Sakai et al., 1990), as well as on a Mariana Arc volcano (Lupton et al., 2006). While natural venting of liquid CO₂ is too rare to significantly affect the global balance of CO₂ between ocean and atmosphere, these sites serve as an ideal natural laboratory where local and short-term consequences of liquid CO₂ discharge to the marine ecosystem can be studied. This is a key focus of current research in context of deliberate carbon storage in the ocean, which will be discussed below.

Carbon dioxide disposal

The rising awareness of the climate impact ascribed to steeply increasing levels of anthropogenic CO₂ in the atmosphere has fueled efforts to identify and evaluate means to sequester the greenhouse gas from the atmosphere or the exchangeable carbon reservoir.

Geological storage Among all options conceived so far, geological storage in saline aquifers, unminable coal seams or oil and gas fields has received most attention and is, sporadically, in place already (Benson et al., 2005). The retention time of CO₂ in geological storage sites can be estimated from natural oil or gas reservoirs, which have been in place for millions of years (Bradshaw and Dance, 2004). Given ideal conditions geological storage of CO₂ may thus be regarded as a permanent form of sequestration. Nevertheless, due to the slope of the geothermal gradient in the continental crust, temperatures in geological storage sites are inevitably higher than the fusion temperatures of CO₂ and exceed the critical temperature of CO₂ (31.1 °C; Lide, 2006) at depths >1000 m. At *P*-/*T*-conditions of geological storage sites such as those presently used CO₂ is less dense than the formation fluid. Consequently, the buoyant CO₂ migrates upward. Geological storage sites thus require impermeable cap rocks structurally trapping the injected CO₂ before, on time scales of up to thousands of years, it is completely dissolved in the formation fluid (solubility trapping; cf. Ennis-King and Paterson, 2003) and subsequently consumed by chemical reactions with the host rock (mineral trapping; cf. Gunter and Perkins, 1993). Abandoned hydrocarbon reservoirs normally do not meet this requirement,

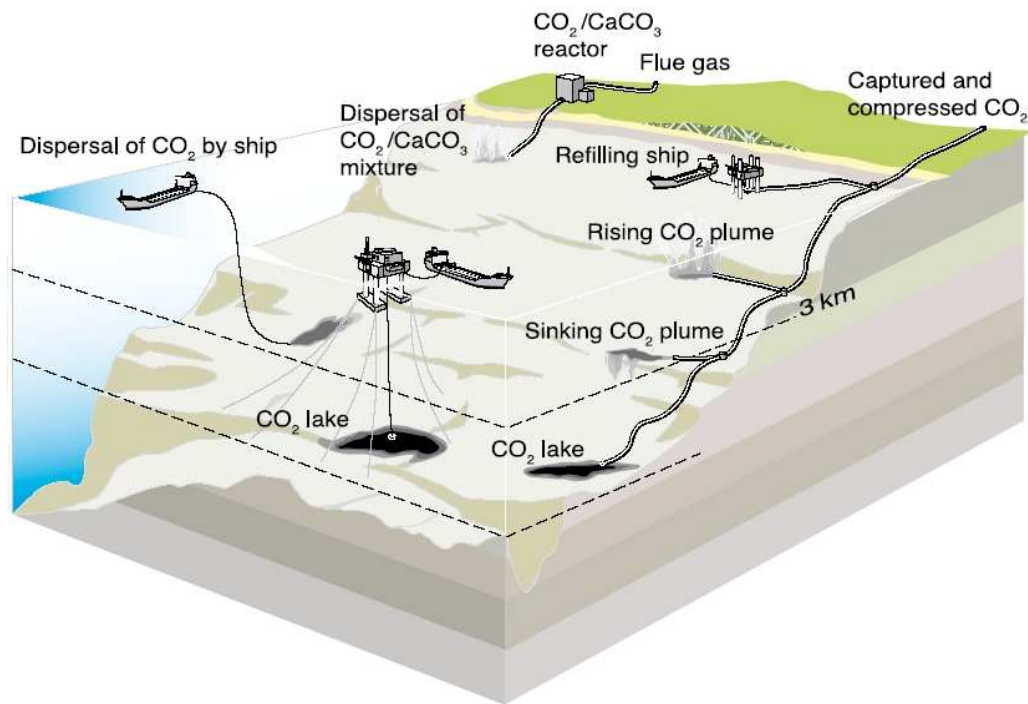


Figure 1.2: Options of CO₂ sequestration by direct ocean storage. Source: IPCC (2005).

since extraction holes provide an ideal pathway for the supercritical fluid to the surface, unless carefully plugged. Therefore, even if feasibility studies indicate the suitability of a site for CO₂ storage, the risk of leakage to the surface persists, requiring site-monitoring for several centuries.

Ocean storage In contrast to geological storage, the negative slope of the hydrotherm in the ocean provides P -/ T -conditions for a gas-liquid transition of CO₂ at depths around 400 mbsl (Figure 1.1), depending on the local temperature. At intermediate depths, the liquid CO₂ is less dense than seawater. The comparatively high compressibility of liquid CO₂ leads to a density ratio inversion of CO₂ and seawater at depths around 2800 mbsl, depending on the local thermal conditions (Figure 3.1). At an average depth of 3800 mbsl and covering an area of 70% of the surface of the earth, the ocean offers several options for direct CO₂ storage at depths below the mixed layer, i.e. the upper layer of the ocean, which equalizes with the atmosphere on a timescale of one year or less (Figure 1.2). Of all options depicted

in the figure, the creation of gravitationally stable pools of CO₂ in morphological depressions on the sea floor at depths below the density ratio inversion might be the most long-lasting scenario (Oshumi, 1995). *P-/T*-conditions prevailing at these depths are suitable for the formation of CO₂ hydrate (Figure 1.1). The hydrate is expected to cover the pool, additionally increasing the isolation by retarding dissolution into the overlying seawater by a factor of 2.7 (Fer and Haugan, 2003). The lifetime of a CO₂ lake largely depends on local hydrodynamic conditions (Haugan and Alendal, 2005) and would be longest in confined environments with low bottom current speeds. Estimations by Fer and Haugan (2003) yield a depth loss of 12 cm a⁻¹ for a mean current speed of 0.05 m s⁻¹ and 170 cm a⁻¹ for an ocean bottom storm of 0.20 m s⁻¹. These predictions have to rely on numerical simulations, since experiments under controlled hydrodynamic and thermodynamic conditions have not been performed yet.

Another option proposes dispersing liquefied CO₂ into the water column at depths between the density inversion and the gas/liquid transition. This scenario is technologically and economically most feasible (Caldeira et al., 2005). The injected CO₂ creates plumes of ascending droplets that dissolve as they rise. The fate of the droplets has been assessed in a number of modeling studies (Sato et al., 2000; Chen et al., 2003; Alendal and Drange, 2001; Zhang, 2005; Gangstø et al., 2005) as well as laboratory (Hirai et al., 1996; Ozaki et al., 2001; Haljasmaa et al., 2005) and ocean (Brewer et al., 2002; Tsouris et al., 2004; Brewer et al., 2006) experiments. Governing factors are droplet dissolution rate and rise velocity. While an exhaustive treatment of the rise velocities of hydrate coated CO₂ droplets is given by Chapters 3 and 4 of this thesis, dissolution rates have not been sufficiently constrained and yet have to rely on simplifying assumptions.

Regardless of the storage options depicted in Figure 1.2, CO₂ initially concentrated to isolated injection sites will, on time scales of millennia, mix with ocean water and equilibrate with the atmosphere (Kheshgi et al., 1994). The retention time of CO₂ dispersed into the water at intermediate depth will be significantly shorter than in the lake scenario and depend on the overturning time of water masses in the basin (300-1000 a; Orr, 2004). Thus, ocean storage must be regarded as a means to accelerate the natural uptake of atmospheric CO₂ across the air/sea interface, which without human interference occurs over many centuries (Sabine et al., 2004). Relative to emissions to the atmosphere, direct ocean storage nevertheless offers (a)

an attenuation of the currently registered rise rates as well as (b) a reduction of the peak values of atmospheric CO₂ concentrations over the next several centuries (Khesghi, 2004). Direct ocean storage could therefore help to alleviate climate effects attributed to the increasing rate of greenhouse gas concentrations currently registered.

As an option to permanently store CO₂ in the oceanic environment, it has recently been suggested to inject liquefied CO₂ in abyssal sediments several hundreds of meters below the sediment/seawater interface (House et al., 2006). According to the authors, at seawater depths >3000 m, *P*-/*T*-conditions in oceanic sediments provide gravitational stability and hydrate forming framework conditions, while a sufficiently thick sedimentary cover prevents the CO₂ from migrating to the free water in significant quantities. A similar suggestion couples gas production to sequestration of liquefied CO₂ by transformation of CH₄ hydrates in natural deposits to CO₂ hydrates (Park et al., 2006; Kvamme et al., 2007). The latter suggestion followed successful laboratory-scale demonstrations of the gas exchange in the cages of the hydrate structure. As a difference to the former scenario, large-scale transformation of CH₄- to CO₂ hydrates is not restricted to the abyssal environment and might therefore not offer permanent retention of CO₂. Nevertheless, the transformation of methane hydrates to thermodynamically more stable CO₂ hydrates (Figure 1.1) might considerably reduce the geological hazard potential of gas hydrates in sediments of submarine slopes. The feasibility of storage of CO₂ in marine sediments requires an understanding of how the injected CO₂ affects diagenetic processes. So far, little is known on the behavior of CO₂, CO₂-rich brines and the formation of CO₂ hydrates in marine sediments, although research activity has increased considerably and is expected to rise still in future.

The relevance of methane and carbon dioxide as agents accelerating atmospheric warming will continue to rise, particularly as countries like China, India and Brazil rapidly evolve to major economic powers. The vast methane hydrate reservoirs could be used not only to produce natural gas but also to safely store CO₂ from conventional fossil fuel power plants. The condensed forms of CO₂ and CH₄ thus provide applications in (1) mitigation schemes of anthropogenic climate change and (2) strategies to meeting the rising demand of energy. As such gas hydrates are key factors in the discussion of two of the most pressing issues of our time. The data presented in the following chapters provide an important contribution to this

evolving field in marine geoscience.

References

- Alendal, G.; Drange, H. Two-phase near-field modeling of purposefully released CO₂ in the ocean. *J. Geophys. Res.*, 106, **2001**, 1085–1096.
- Archer, D. Methane hydrate stability and anthropogenic climate change. *Biogeosciences*, 4, **2007**, 521–544.
- Bartdorff, O.; Wallmann, K.; Latif, M.; Semenov, V. Phanerozoic evolution of atmospheric methane. *Global Biogeochem. Cycles*, 22, **2008**, GB1008, doi:10.1029/2007GB002985.
- Benson, S.; Anderson, J.; Bachu, S.; Bashir, H.; Biswajit, B.; Bradshaw, J.; Deguchi, G.; Gale, J.; von Goerne, G.; Heidug, W.; Holloway, S.; Kamal, R.; Keith, D.; Lloyd, P.; Rocha, P.; Senior, B.; Thomson, J.; Torp, T.; Wildenborg, T.; Wilson, M.; Zarlenga, F.; Zhou, D. Underground Geological Storage. In Metz, B.; Davidson, O.; de Coninck, H.; Loos, M.; Meyer, L. (eds.), *IPCC Special Report on Carbon Dioxide Capture and Storage*. Cambridge University Press, Cambridge **2005**, 195–276.
- Berner, R. A. The rise of plants and their effect on weathering and atmospheric CO₂. *Science*, 276, **1997**, 544–546.
- Berner, R. A. GEOCARB III: A revised model of atmospheric CO₂ over Phanerozoic time. *Am. J. Sci.*, 301, **2001**, 182–204.
- Berner, R. A. GEOCARBSULF: A combined model for Phanerozoic atmospheric O₂ and CO₂. *Geochim. Cosmochim. Acta*, 70, **2006**, 5653–5664.
- Boetius, A.; Ravenschlag, K.; Schubert, C. J.; Rickert, D.; Widdel, F.; Gieseke, A.; Amann, R.; Jørgensen, B. B.; Witte, U.; Pfannkuche, O. A marine microbial consortium apparently mediating anaerobic oxidation of methane. *Nature*, 407, **2000**, 623–626.
- Bradshaw, J. B.; Dance, T. Mapping geological storage prospectivity of CO₂ for the world sedimentary basins and regional source to sink matching. In *Conference on Greenhouse Gas Control Technologies*. Vancouver, Canada **2004**, 583–592.

- Brewer, P. G.; Chen, B.; Warzinski, R.; Baggeroer, A.; Peltzer, E. T.; Dunk, R. M.; Walz, P. Three dimensional acoustic monitoring and modeling of a deep-sea CO₂ droplet cloud. *Geophys. Res. Lett.*, **33**, **2006**, L23607.
- Brewer, P. G.; Peltzer, E. T.; Friederich, G.; Rehder, G. Experimental determination of the fate of rising CO₂ droplets in sea water. *Environ. Sci. Technol.*, **36**, **2002**, 5441–5446.
- Brooks, J. M.; Bryant, W. R.; Bernard, B. B.; Cameron, N. R. The nature of gas hydrates on the Nigerian continental slope. In Holder, G. D.; Bishnoi, P. R. (eds.), *Gas Hydrates: Challenges for the Future.*, vol. 912. Annals of the New York Academy of Sciences, New York **2000**, 76–93.
- Brooks, J. M.; Cox, H. B.; Bryant, W. R.; Kennicutt, M. C.; Mann, R. G.; McDonald, T. J. Association of gas hydrates and oil seepage in the Gulf of Mexico. *Org. Geochem.*, **10**, **1986**, 221–234.
- Buffett, B.; Archer, D. Global inventory of methane clathrate: sensitivity to changes in the deep ocean. *Earth Planet. Sci. Lett.*, **227**, **2004**, 185–199.
- Caldeira, K.; Akai, M.; Brewer, P. G.; Chen, B.; Haugan, P. M.; Iwama, T.; Johnston, P.; Keshgi, H.; Q., L.; Oshumi, T.; Pörtner, H.; Sabine, C.; Shirayama, Y.; Thomson, J. Ocean Storage. In Metz, B.; Davidson, O.; De Coninck, H.; Loos, M.; Meyer, L. (eds.), *IPCC Special Report on Carbon Dioxide Capture and Storage*. Cambridge University Press, Cambridge, U.K. **2005**, 277–318.
- Caldeira, K.; Wickett, M. E. Anthropogenic carbon and ocean pH. *Nature*, **452**, **2003**, 365–368.
- Chapman, N. R.; Pohlman, J. W.; Coffin, R. B.; Chanton, J. P.; Lapham, L. Thermogenic gas hydrates in the northern Cascadia Margin. *EOS*, **85**, **2004**, 361–365.
- Chen, B.; Song, Y.; Nishio, M.; Akai, M. Large-eddy simulation of double cloud formation induced by CO₂ dissolution in the ocean. *Tellus*, **55**, **2003**, 723–730.
- De Roo, J. L.; Peters, C. J.; Lichtenthaler, R. N.; Diepen, G. A. M. Occurrence of methane hydrate in saturated and undersaturated solutions of sodium-chloride and water in dependence of temperature and pressure. *AIChE J.*, **29**, **1983**, 651–657.

- Denman, K.; Brasseur, G.; Chidthaisong, A.; Ciais, P.; Cox, P. M.; Dickinson, R. E.; Hauglustaine, D.; Heinze, C.; Holland, E.; Jacob, D.; Lohmann, U.; Ramachandran, S.; da Silva Dias, P. L.; Wofsy, S. C.; Zhang, X. Couplings Between Changes in the Climate System and Biogeochemistry. In Solomon, S.; Qin, D.; Manning, M.; Chen, Z.; Marquis, M.; Averyt, K. B.; Tignor, M.; Miller, H. L. (eds.), *Climate Change 2007: The Physical Science Basis. Contribution of Working Group I to the Fourth Assessment Report of the Intergovernmental Panel on Climate Change*. Cambridge University Press, Cambridge, New York **2007**.
- Dickens, G. R. Carbon cycle - The blast in the past. *Nature*, *401*, **1999**, 752–755.
- Dickens, G. R.; O’Neil, J. R.; Rea, D. K.; Owen, R. M. Dissociation of oceanic methane hydrate as a cause of the carbon-isotope excursion at the end of the Paleocene. *Paleoceanography*, *10*, **1995**, 965–971.
- Dlugokencky, E. J.; Houweling, S.; Bruhwiler, L.; Masarie, K. A.; Lang, P. M.; Miller, J. B.; Tans, P. P. Atmospheric methane levels off: Temporary pause or a new steady state. *Geophys. Res. Lett.*, *30*, **2003**, doi:10.1029/2003GL018126.
- Ehhalt, P.; Prather, M.; Dentener, F.; Derwent, R.; Dlugokencky, E. J.; Holland, E.; Isaksen, I.; Katima, J.; Kirchhoff, V.; Matson, P.; Midgley, P.; Wang, M. Atmospheric Chemistry and Greenhouse Gases. In Houghton, J. T.; Ding, Y.; Griggs, D. J.; Noguera, M.; van der Linden, P. J.; Xiaosu, D. (eds.), *The Scientific Basis. Contribution of Working Group I to the Third Assessment Report of the Intergovernmental Panel on Climate Change*. Cambridge University Press, Cambridge **2001**.
- Ennis-King, J. P.; Paterson, L. Role of convective mixing in the long-term storage of carbon dioxide in deep saline formations. In *Society of Petroleum Engineers Technical Conference and Exhibition*. Denver, Colorado **2003**.
- Etioppe, G.; Milkov, A. V. A new estimate of global methane flux from onshore and shallow submarine mud volcanoes to the atmosphere. *Environ. Geol.*, *46*, **2004**, 997–1002.
- Fer, I.; Haugan, P. M. Dissolution from a liquid CO₂ lake disposed in the deep ocean. *Limnol. Oceanogr.*, *48*, **2003**, 872–883.
- Forster, P.; Ramaswamy, V.; Artaxo, P.; Bernsten, T.; Betts, R.; Fahey, D. W.; Haywood, J.; Lean, J.; Lowe, D. C.; Myhre, G.; Nganga, J.; Prinn, R.; Raga, G.; Schulz,

- M.; van Dorland, R. Changes in Atmospheric Constituents and in Radiative Forcing. In Solomon, S.; Qin, D.; Manning, M.; Chen, Z.; Marquis, M.; Averyt, K. B.; Tignor, M.; Miller, H. L. (eds.), *Climate Change 2007: The Physical Science Basis. Contribution of Working Group I to the Fourth Assessment Report of the Intergovernmental Panel on Climate Change*. Cambridge University Press, Cambridge, New York 2007.
- Gangstø, R.; Haugan, P. M.; Alendal, G. Parameterization of drag and dissolution of rising CO₂ drops in seawater. *Geophys. Res. Lett.*, 32, 2005, L10612, doi:10.1029/2005GL022637.
- Gattuso, J.-P.; Allemand, D.; Frankignoulle, M. Photosynthesis and calcification at cellular, organismal and community levels in coral reefs: a review on interactions and control by carbonate chemistry. *Am. Zool.*, 39, 1999, 160–183.
- Ginsburg, G.; Guseynov, R.; Dadashev, A.; Invanova, G.; Kazantsev, S.; Soloviev, V.; Telepnev, E.; Askeri-Nasirov, R.; Yesikov, A. Gas hydrates of the southern Caspian. *Int. Geol. Rev.*, 34, 1992, 765–782.
- Ginsburg, G.; Soloviev, V. *Submarine Gas Hydrates*. VNIIOkeangeologia, St. Petersburg 1998.
- Ginsburg, G. D.; Soloviev, V. A. Russian research on submarine gas hydrate geology. In *International Conference on Natural Gas Hydrates.*, vol. 715 of *Annals of the New York Academy of Sciences*. 1994, 484–486.
- Ginsburg, G. D.; Soloviev, V. A.; Cranston, R. E.; Lorenson, T. D.; Kvenvolden, K. A. Gas hydrates in the continental-slope, offshore Sakhalin Island, Okhotsk Sea. *Geo-Mar. Lett.*, 13, 1993, 41–48.
- Gunter, W. D.; Perkins, E. H. Aquifer Disposal of CO₂-Rich Gases - Reaction Design for Added Capacity. *Energy Convers. Manage.*, 34, 1993, 941–948.
- Haljasmaa, I. V.; Vipperman, J. S.; Lynn, R. J.; Warzinski, R. P. Control of a fluid particle under simulated deep-ocean conditions in a high-pressure water tunnel. *Rev. Sci. Instrum.*, 76, 2005, 025111.1–025111.11.
- Handa, Y. P. Compositions, enthalpies of dissociation, and heat capacities in the range of 85-K to 270-K for clathrate hydrates of methane, ethane and propane,

- and enthalpy of dissociation of isobutanehydrate, as determined by a heat-flow calorimeter. *J. Chem. Thermodyn.*, **18**, 1986, 915–921.
- Haugan, P. M.; Alendal, G. Turbulent diffusion and transport from a CO₂ lake in the deep ocean. *J. Geophys. Res.*, **110**, 2005, C09S14.
- Hesselbo, S. P.; Gröcke, D. R.; Jenkyns, H. C.; Bjerrum, C. J.; Farrimond, P.; Morgans Bell, H. S.; Green, O. R. Massive dissociation of gas hydrate during a Jurassic oceanic anoxic event. *Nature*, **406**, 2000, 392–395.
- Hirai, S.; Okazaki, K.; Araki, N.; Yazawa, H.; Ito, H.; Hijikata, K. Transport phenomena of liquid CO₂ in pressurized water flow with clathrate hydrate at the interface. *Energy Convers. Manage.*, **37**, 1996, 1073–1078.
- House, K. Z.; Schrag, D. P.; Harvey, C. F.; Lackner, K. S. Permanent carbon dioxide storage in deep-sea sediments. *Proc. Natl. Acad. Sci. U.S.A.*, **103**, 2006, 12291–12295.
- Imbrie, J.; Boyle, E. A.; Clemens, S. C.; Duffy, A.; Howard, W. R.; Kukla, G.; Kutzbach, J.; Martinson, D. G.; McIntyre, A.; Mix, A. C.; Peterson, L. C.; Pisias, N. G.; Prell, W. L.; Raymo, M. E.; Shackleton, N. J.; Toggweiler, J. R. On the structure and origin of major glaciation cycles. Linear responses to Milankovic forcing. *Paleoceanography*, **7**, 1992, 701–738.
- IPCC, . *IPCC Special Report on Carbon Dioxide Capture and Storage*. Cambridge University Press, Cambridge, New York 2005.
- Kennett, J. P.; Cannariato, K. G.; Hendy, I. L.; Behl, R. J. Carbon isotopic evidence for methane hydrate instability during Quaternary interstadials. *Science*, **288**, 2000, 128–133.
- Kennett, J. P.; Cannariato, K. G.; Hendy, I. L.; Behl, R. J. *Methane Hydrates in Quaternary Climate Change: The Clathrate Gun Hypothesis*. The American Geophysical Union, Washington, DC 2003.
- Keppler, F.; Hamilton, J. T. G.; Braß, M.; Röckmann, T. Methane emissions from terrestrial plants under aerobic conditions. *Nature*, **439**, 2006, 187–191.
- Key, R. M.; Kozyr, A.; Sabine, C. L.; Lee, K.; Wanninkhof, R.; Bullister, J. L.; Feely, R. A.; Millero, F. J.; Mordy, C.; Peng, T.-H. A global ocean carbon climatology:

- Results from Global Data Analysis Project (GLODAP). *Global Biogeochem. Cycles*, **18**, **2004**, GB4031, doi:10.1029/2004GB002247.
- Kheshgi, H. S. Ocean carbon sink duration under stabilization of atmospheric CO₂: A 1,000-year timescale. *Geophys. Res. Lett.*, **31**, **2004**, –.
- Kheshgi, H. S.; Flannery, B. P.; Hoffert, M. I.; Lapenis, A. G. The effectiveness of marine CO₂ disposal. *Energy*, **29**, **1994**, 967–975.
- Klauda, J. B.; Sandler, S. I. Global distribution of methane hydrate in ocean sediment. *Energy Fuels*, **19**, **2005**, 459–470.
- Kleypas, J. A.; Buddermeier, R. W.; Archer, D.; Gattuso, J.-P.; Langdon, C.; Opdyke, B. N. Geochemical consequences of increased atmospheric carbon dioxide on coral reefs. *Science*, **284**, **1999**, 118–120.
- Kvamme, B.; Graue, A.; Buanes, T.; Kumetsoua, T.; Ersland, G. Storage of CO₂ in natural gas hydrate reservoirs and the effect of hydrate as an extra sealing in cold aquifers. *Int. J. Greenhouse Gas Control*, **1**, **2007**, 236–246.
- Kvenvolden, K. A. Potential effects of gas hydrates on human welfare. *Proc. Nat. Acad. Sci. U.S.A.*, **96**, **1999**, 3420–3426.
- Langdon, C.; Broecker, W. S.; Hammond, D. E.; Glenn, E.; Fitzsimmons, K.; Nelson, S. G.; Peng, T.-H.; Hajdas, I.; Bonani, G. Effect of elevated CO₂ on the community metabolism of an experimental coral reef. *Global Biogeochem. Cycles*, **17**, **2003**, doi:10.1029/2002GB001941.
- Lelieveld, J.; Crutzen, P. J. Indirect chemical effects of methane on climate warming. *Nature*, **355**, **1992**, 339–342.
- Lide, D. R. (ed.). *CRC Hand Book of Chemistry and Physics*. B&T, Boca Raton, 87th ed. **2006**.
- Lupton, J.; Butterfield, D.; Lilley, M.; Evans, L.; Nakamura, K.; Chadwick, W.; Resing, J.; Embley, R.; Olson, E.; Proskurowski, G.; Baker, E.; de Ronde, C.; Roe, K.; Greene, R.; Lebon, G.; Young, C. Submarine venting of liquid carbon dioxide on a Mariana Arc volcano. *Geochem. Geophys. Geosyst.*, **7**.

- MacDonald, I. R.; Guinasso, N. L.; Sassen, R.; Brooks, J. M.; Lee, L.; Scott, K. T. Gas hydrate that breaches the sea floor on the continental slope of the Gulf of Mexico. *Geology*, *22*, **1994**, 699–702.
- Maini, B. M.; Bishnoi, P. R. Experimental investigation of hydrate formation behaviour of a natural gas bubble in a simulated deep sea environment. *Chem. Eng. Sci.*, *36*, **1981**, 183–189.
- Makogon, Y. F. A gas hydrate formation in the gas saturated layers under low temperature. *Gas. Ind.*, *5*.
- McGinnis, D. F.; Greinert, J.; Artemov, Y.; Beaubien, S. E.; Wüest, A. Fate of rising methane bubbles in stratified waters: How much methane reaches the atmosphere? *J. Geophys. Res.*, *111*, **2006**, C09007, doi:10.1029/2005JC003183.
- Milkov, A. V. Global estimates of hydrate-bound gas in marine sediments: how much is really out there? *Earth-Sci. Rev.*, *66*, **2004**, 183–197.
- Orr, J. C. Modelling of ocean storage of CO₂ - The GOSAC study, Report PH4/37. In *Greenhouse Gas R&D Programme*. International Energy Agency, Cheltenham, U.K. **2004**, 96.
- Orr, J. C.; Fabry, V. J.; Aumont, O.; Bopp, L.; Doney, S. C.; Feely, R. A.; Gnanadesikan, A.; Gruber, N.; Ishida, A.; Joos, F.; Key, R. M.; Lindsay, K.; Maier-Reimer, E.; Matear, R.; Monfray, P.; Mouchet, A.; Najjar, R. G.; Plattner, G. K.; Rodgers, K. B.; Sabine, C. L.; Sarmiento, J. L.; Schlitzer, R.; Slater, R. D.; Totterdell, I. J.; Weirig, M. F.; Yamanaka, Y.; Yool, A. Anthropogenic ocean acidification over the twentyfirst century and its impact on calcifying organisms. *Nature*, *437*, **2005**, 681–686.
- Oshumi, T. CO₂ storage options in the deep sea. *Mar. Technol. Soc. J.*, *29*, **1995**, 58–66.
- Ozaki, M.; Minamiura, J.; Kitajima, Y.; Mizokami, S.; Takeuchi, K.; Hatakenaka, K. CO₂ sequestration by moving ships. *J. Mar. Sci. Technol.*, *6*, **2001**, 51–58.
- Park, Y.; Kim, D.-Y.; Lee, J.-W.; Huh, D.-G.; Park, K.-P.; Lee, J.; Lee, H. Sequestering carbon dioxide into complex structures of naturally occurring gas hydrates. *Proc. Nat. Acad. Sci. U.S.A.*, *103*, **2006**, 12690–12694.

- Paul, A. Z. The effect of benthic biological processes on the CO₂ carbonate system. In Andersen, N. R. (ed.), *The Fate of Fossil Fuel CO₂ in the Oceans*, vol. 345. Plenum Press 1978.
- Paull, C. K.; Brewer, P. G.; Ussler, W. I.; Peltzer, E. T.; Rehder, G.; Clague, D. An experiment demonstrating that marine slumping is a mechanism to transfer methane from seafloor gas-hydrate deposits into the upper ocean and atmosphere. *Geo-Mar. Lett.*, 22, 2003, 198–203.
- Paull, C. K.; Ussler, W. I.; Lorenson, T.; Winters, W.; Dougherty, J. Geochemical constraints on the distribution of gas hydrates in the Gulf of Mexico. *Geo-Mar. Lett.*, 25, 2005, 273–280.
- Pearson, P. N.; Palmer, M. R. Atmospheric carbon dioxide concentrations over the past 60 million years. *Nature*, 406, 2000, 695–699.
- Petit, J.; Jouzel, J.; Raynaud, D.; Barkov, N.; Barnola, J.-M.; Basile, I.; Bender, M.; Chappellaz, J.; Davis, M.; Delaygue, G.; Delmotte, M.; Kotlyakov, V.; Legrand, M.; Lipenkov, V.; Lorius, C.; Pépin, L.; Ritz, C.; Saltzman, E.; Stievenard, M. Climate and atmospheric history of the past 420,000 years from the Vostok ice core, Antarctica. *Nature*, 399, 1999, 429–436.
- Prentice, I. C.; Farquhar, G. D.; Fasham, M. J. R.; Goulden, M. L.; Heimann, M.; Jaramillo, V. J.; Kheshgi, H. S.; Le Quéré, C.; Scholes, R. J.; Wallace, D. W. R. The Carbon Cycle and Atmospheric Carbon Dioxide. In Houghton, J. T.; Ding, Y.; Griggs, D. J.; Noguer, M.; van der Linden, P. J.; Xiaosu, D. (eds.), *The Scientific Basis. Contribution of Working Group I to the Third Assessment Report of the Intergovernmental Panel on Climate Change*. Cambridge University Press, Cambridge 2001.
- Raupach, M. R.; Marland, G.; Ciais, P.; Le Quéré, C.; Canadell, J. G.; Klepper, G.; Field, C. B. Global and regional drivers of accelerating CO₂ emissions. *Proc. Natl. Acad. Sci. U.S.A.*, 104, 2007, 10288–10293.
- Rehder, G.; Brewer, P.; Peltzer, E. T.; Friederich, G. Enhanced lifetime of methane bubble streams within the deep ocean. *Geophys. Res. Lett.*, 29, 2002, 1731, doi: 10.1029/2001GL013966.

- Riebesell, U.; Zondervan, I.; Rost, B.; Tortell, P. D.; Zeebe, R. E.; Morel, F. M. M. Reduced calcification of marine plankton in response to increased atmospheric CO₂. *Nature*, 407, **2000**, 364–367.
- Roberts, J. M.; Wheeler, A. J.; Freiwald, A. Reefs of the deep: The biology and geology of cold-water coral ecosystems. *Science*, 312, **2006**, 543–547.
- Royal Society. Ocean Acidification Due to Increasing Atmospheric Carbon Dioxide. **2005**.
- Sabine, C. L.; Feely, R. A.; Gruber, N.; Key, R. M.; Lee, K.; Bullister, J. L.; Wanninkhof, R.; Wong, C. S.; Wallace, D. W. R.; Tilbrook, B.; Millero, F. J.; Peng, T. H.; Kozyr, A.; Ono, T.; Rios, A. F. The oceanic sink for anthropogenic CO₂. *Science*, 305, **2004**, 367–371.
- Sakai, H.; Gamo, T.; Kim, E. S.; Tsutsumi, M.; Tanaka, T.; Ishibashi, J.; Wakita, H.; Yamano, M.; Oomori, T. Venting of Carbon-Dioxide Rich Fluid and Hydrate Formation in Mid-Okinawa Trough Backarc Basin. *Science*, 248, **1990**, 1093–1096.
- Sato, T.; Jung, R.-T.; Abe, S. Direct simulation of droplet flow with mass transfer at interface. *J. Fluids Eng.*, 122, **2000**, 510–516.
- Sauter, E. J.; Muyakshin, S. I.; Charlou, J.-L.; Schlüter, M.; Boetius, A.; Jerosch, K.; Damm, E.; Foucher, J.-P.; Klages, M. Methane discharge from a deep-sea submarine mud volcano into the upper water column by gas hydrate coated methane bubbles. *Earth Planet. Sci. Lett.*, 243, **2006**, 354–365.
- Schlitzer, R. Ocean Data View **2007**.
- Shackleton, N. J.; Hall, M. A.; Vincent, E. Phase relationships between millennial-scale events 64,000–24,000 years ago. *Paleoceanography*, 15, **2000**, 565–569.
- Shakhova, N.; Semiletov, I.; Panteleev, G. The distribution of methane on the Siberian Arctic shelves: Implications for the marine methane cycle. *Geophys. Res. Lett.*, 32, **2005**, L09601, doi:10.1029/2005/GL022751.
- Shitashima, K.; Maeda, Y.; Koike, Y.; Oshumi, T. Natural analogue of the rise and dissolution of liquid CO₂ in the ocean. *Int. J. Greenhouse Gas Control*, 2, **2008**, 95–104.

- Siegenthaler, U.; Stocker, T. F.; Monnin, E.; Lüthi, D.; Schwander, J.; B., S.; Raynaud, D.; Barnola, J.-M.; Fischer, H.; Masson-Delmotte, V.; Jouzel, J. Stable carbon cycle-climate relationship during the Late Pleistocene. *Science*, **310**, **2005**, 1313–1317.
- Soloviev, V. A. Global estimation of gas content in submarine gas hydrate accumulations. *Russian Geol. Geophys.*, **43**, **2002**, 609–624.
- Spahni, R.; Chappellaz, J.; Stocker, T. F.; Loulergue, L.; Hausammann, G.; Kawamura, K.; Flückiger, J.; Schwander, J.; Raynaud, D.; Masson-Delmotte, V.; Jouzel, J. Atmospheric methane and nitrous oxide of the Late Pleistocene from Antarctic ice cores. *Science*, **310**, **2005**, 1317–1321.
- Suess, E.; Torres, M. E.; Bohrmann, G.; Collier, R. W.; Greinert, J.; Linke, P.; Rehder, G.; Trehu, A.; Wallmann, K.; Winckler, G.; Zuleger, E. Gas hydrate destabilization: enhanced dewatering, benthic material turnover and large methane plumes at the Cascadia convergent margin. *Earth Planet. Sci. Lett.*, **170**, **1999**, 1–15.
- Suess, E.; Torres, M. E.; Bohrmann, G.; Collier, R. W.; Rickert, D.; Goldfinger, C.; Linke, P.; Heuser, A.; Sahling, H.; Heeschen, K.; Jung, C.; Nakamura, K.; Greinert, J.; Pfannkuche, O.; Trehu, A.; Klinkhammer, G.; Whiticar, M. J.; Eisenhauer, A.; Teichert, B.; Elvert, M. Sea Floor Methane Hydrates at Hydrate Ridge, Cascadia Margin. In Paull, C. K.; Dillon, W. P. (eds.), *Natural Gas Hydrates: Occurrence, Distribution, and Detection.*, vol. 124 of *Geophysical Monograph Series*. American Geophysical Union, Washington, DC **2001**, 87–98.
- Sultan, N.; Cochonat, P.; Foucher, J. P.; Mienert, J. Effect of gas hydrates melting on seafloor stability. *Mar. Geol.*, **213**, **2004**, 379–401.
- Sun, R.; Duan, Z. H. Prediction of CH₄ and CO₂ hydrate phase equilibrium and cage occupancy from ab initio intermolecular potentials. *Geochim. Cosmochim. Acta*, **69**, **2005**, 4411–4424.
- Tortell, P. D.; DiTullio, G. R.; Sigmann, D. M.; Morel, F. M. M. CO₂ effects on taxonomic composition and nutrient utilization in an Equatorial Pacific phytoplankton assemblage. *Mar. Ecol-Prog. Ser.*, **236**, **2002**, 37–43.
- Tsouris, C.; Brewer, P. G.; Peltzer, E. T.; Walz, P.; Riestenberg, D.; Liang, L.; West, O. R. Hydrate composite particles for ocean carbon sequestration: Field verification. *Environ. Sci. Technol.*, **38**, **2004**, 2470–2475.

Vogt, P. R.; Jung, W. Y. Holocene mass wasting on upper non-Polar continental slopes - due to post-glacial ocean warming and hydrate dissociation? *Geophys. Res. Lett.*, 29, **2002**, 1341, doi: 10.1029/2001GL013488.

Wuebbles, D. J.; Hayhoe, K. Atmospheric methane and global change. *Earth-Sci. Rev.*, 57, **2002**, 177–210.

Zhang, Y. Fate of rising CO₂ droplets in seawater. *Environ. Sci. Technol.*, 39, **2005**, 7719–7724.

2 Methane hydrate dissolution rates in undersaturated seawater under controlled hydrodynamic forcing

Nikolaus K. Bigalke^{*1}, Gregor Rehder², Giselher Gust³

Leibniz Institute of Marine Sciences at the University of Kiel, Wischhofstr. 1-3,
24114 Kiel, Germany

nbigalke@ifm-geomar.de

Abstract

The dissolution of in-situ generated methane hydrate in undersaturated, synthetic seawater ($S=35$) was investigated in a series of laboratory based experiments at P -/ T -conditions within the hydrate stability field. A controlled flow field was generated across the smooth hydrate surface to test if, in addition to thermodynamic variables, the dissolution rate is influenced by changing hydrodynamic conditions. The dissolution rate was found to be strongly dependent on the friction velocity, showing that hydrate dissolution in undersaturated seawater is a diffusion-controlled process. The experimental data was used to obtain diffusional mass transfer coefficients k_d , which were found to correlate linearly with u^* . The resulting k_d/u^* -correlation allows predicting the flux of methane from natural gas hydrate exposures at the sediment/seawater interface into the bulk water for a variety of

¹phone: +49 431 600-1410, fax:+49 431 600-1400

²Leibniz Institute for Baltic Sea Research at the University of Rostock, Seestr. 15, 18119 Rostock, Germany

³Hamburg University of Technology, Institute of Ocean Engineering, Schwarzenbergstr. 95, 21073 Hamburg, Germany

natural P , T and flow conditions. It also is a tool for estimating the rate of hydrate re-growth at locations where natural hydrate outcrops at the seafloor persist in contact with undersaturated seawater.

2.1 Introduction

Clathrate hydrates of natural gases (gas hydrates in the following) are widely distributed within sediments along active and passive continental margins. Gas hydrates and gas hydrate stability specifically have become an important field of study in the past decades for a number of reasons. Triggered by the occurrence of hydrate plugs clogging the conduit in pipelines for hydrocarbons, economical interest in gas hydrates increased further, since natural deposits are estimated to hold more hydrocarbon energy than all known conventional gas reservoirs combined (Buffett and Archer, 2004; Milkov, 2004). In order to mitigate adverse climate effects of yet another anthropogenic source of atmospheric CO_2 , it was recently suggested that the production of gas hydrate derived natural gas may be realized by large scale replacement of the cavity-occupying methane by fossil-fuel derived CO_2 (Park et al., 2006), which at similar equilibrium conditions forms clathrates of isotypical structure (Sloan and Koh, 2008). Recent scientific interest in natural gas hydrates is not only economically motivated, though. In the ambient atmosphere, methane, the main constituent of the gas fixed in natural hydrates, has 26x the global warming potential of CO_2 on a mole-per-mole base (Lelieveld and Crutzen, 1998). Rapid global warming during several episodes of the Phanerozoic has been linked to large scale release of methane from rapidly decomposing gas hydrates into ocean waters and eventually the atmosphere (Dickens et al., 1995; Kennett et al., 2000; Hesselbo et al., 2000). Furthermore, hydrate decomposition in sediments of continental margins has been suggested to trigger slope failures, releasing an even larger amount of the greenhouse gas from the free gas reservoir below (Katz et al., 1999; Paull et al., 2003).

The stability of methane hydrate depends on the physicochemical equilibrium between all other phases present in the system. Equilibrium requires the chemical potential of all these phases to be equal. By changing P , T or the chemical activities of the components in the system, the equilibrium is disturbed (Wedler, 2007). This results in a shift of phase proportions up to potential disappearance of a phase,

until a new, stable equilibrium is reached. In terms of P and T , the stability of methane hydrate is well constrained. A shift of P or T to coordinates outside the hydrate stability field (HSF) leads to dissociation, the rates of which are limited by the transfer of heat away from the dissociating front (Sloan and Koh, 2008). Heat transfer limitations are largely eliminated when hydrate decomposition occurs due to an undersaturation of dissolved methane (hydrate) in a coexisting liquid phase yet at P, T conditions within the HSF. Controls on the decomposition rates in these cases are not well constrained. Specifically, the flux of methane dissolving into ocean waters (which typically is highly undersaturated with respect to methane (Rehder et al., 1999; Heeschen et al., 2004) has yet to be quantified. This is especially true for hydrates that are exposed to flow, whether they are buried in marine sediment or whether they are exposed at the immediate sea-floor surface. Surface-near hydrates and hydrate exposures have been reported worldwide (Suess et al., 2001; MacDonald et al., 1994; Chapman et al., 2004). Assessment of the stability of these gas hydrates requires the test if in addition to thermodynamic variables, incorporation of hydrodynamic variables into numerical models is required to assess the flux of methane into the ocean. Quantifying the role of the flow field around gas hydrates is also required to predict the release of gas from floating hydrates, which have been observed in nature and been proposed to play a role in methane release from hydrate-bearing sediments after slope failure (Paull et al., 2003; Brewer et al., 2002).

Relevant experiments describing the flux of a solute species across a solid-liquid interface were carried out by Santschi et al. (1983, 1991) and Opdyke et al. (1987). In these studies the dissolution of smooth alabaster plates in natural seawater and distilled water respectively was measured. Santschi et al. (1983) showed that dissolution of alabaster was limited by diffusion rather than by the rate of release of ions from the crystal lattice. This finding was confirmed by Opdyke et al. (1987), who established a relationship between the decomposition rate of the alabaster plates and the friction velocity u^* induced by unidirectional, hydrodynamic smooth turbulent flow. In a discussion of the stability of gas hydrates outcropping on the sea floor Egorov et al. (1999) also use a diffusive boundary layer model with a fixed boundary layer thickness to calculate dissolution of the hydrates in a flow of undersaturated seawater. Rehder et al. (2004) report on observations of dissolution rates of CO_2 and CH_4 hydrates in an open ocean experiment. Synthetic hydrate

specimens were dissolved at 1028 mbsl well within the HSF. The authors observed that the dissolution rate ratio of the CH₄ and CO₂ hydrate specimens matched the solubility ratio of the two gases in seawater and concluded that hydrate decomposition due to an undersaturation in coexisting seawater is a diffusion-controlled process. Very recently, Hester et al. (2008) showed that the dissolution rate of the synthetic samples in Rehder et al. (2004) agree well with observed dissolution rates of natural gas hydrates observed at Barkley Canyon, off Vancouver Island, and also suggest diffusion-controlled dissolution kinetics. The data of Rehder et al. (2004) was also used in a model by Nihous and Masutani (2006) who combine the diffusion of the hydrate guest species into the bulk water with the intrinsic decomposition of the hydrate within a liquid desorption layer between the diffusive boundary layer and the solid hydrate phase. The authors question the applicability of the formulas employed for intrinsic hydrate decomposition to the conditions of the ocean experiment, since calculations failed to mirror the observed proportionality of decomposition rate and solubility for CO₂ and CH₄ hydrates. Due to a lack of accurate experimental data obtained under controlled thermodynamic and hydrodynamic conditions, effects of flow on the decomposition of gas hydrates have still not been sufficiently constrained. Here, we report mass transfer rates gained in measurements on the decomposition of in-situ generated methane hydrate exposed to precisely adjusted friction velocities at selected *P-/T*-conditions within the HSF and show that hydrate decomposition is indeed an entirely diffusion-controlled process under the conditions investigated. The experiments were carried out in an autoclaved flux chamber characterized as *microcosm* in Tengberg et al. (2004).

2.2 Dissolution theory

The dissolution of methane hydrate in undersaturated seawater can be expected to follow the reverse order of hydrate crystallization from an oversaturated aqueous solution outlined by Sloan and Koh (2008). Accordingly, dissolution undergoes two steps: (1) desorption of water and methane molecules in a thin layer adjacent to the solid hydrate and (2) diffusive and eddy transport of the methane and water molecules away from the desorption layer, into the bulk seawater. In the turbulent flow regime distal to the hydrate surface eddy diffusion is the dominating form of methane transport. Closer to the hydrate surface, the flow regime changes from

turbulent to laminar. At the transition, the eddy diffusion coefficient is drastically reduced and decreases further to values below that of the molecular diffusion coefficient with proximity to the hydrate surface. The film in which diffusion is the dominating form of transport is termed diffusive sub- or boundary layer (Gundersen and Jørgensen, 1990). Its thickness is a function of the friction exerted on the hydrate surface by the seawater current and the surface roughness. Water directly in contact with the hydrate layer should be saturated with methane. Thus, a concentration gradient exists across desorption and diffusive sublayers. Since desorption of the molecules in the desorption layer generally occurs at different rates than diffusion in the diffusive boundary layer, the gradient shows a kink at the interface of the two layers. Consequently, thermodynamic driving forces causing methane molecules to migrate from the regions of high concentrations toward regions of low concentrations in the bulk seawater assume different magnitudes in the desorption and diffusive boundary layers. The number of methane molecules, n , transferred across the two layers per time increment is given by Sloan and Koh (2008) as

$$\frac{dn}{dt} = K' A (C_{\text{sat}} - C_{\text{bulk}}) \quad (2.1)$$

Here, C_{sat} is the equilibrium saturation concentration of methane in seawater, C_{bulk} the methane concentration in the bulk liquid, A the area of the hydrate/seawater interface and K' the overall transfer coefficient. The latter is introduced to simplify the description of the combined transport determined by desorption of molecules from the hydrate crystal and diffusion into the bulk seawater. It relates desorption rate constant, k_r , and the diffusional mass transfer coefficient, k_d , via

$$\frac{1}{K'} = \frac{1}{k_r} + \frac{1}{k_d} \quad (2.2)$$

(cf. Sloan and Koh, 2008). Note that $k_d = D/z$, where z is the thickness of the diffusive boundary layer and D the molecular diffusivity of methane. In a closed system, $dn/dt = dC/dt * m_{\text{SW}}$, where m_{SW} is the total mass of the seawater in the system and C the methane concentration in mol kg^{-1} . Thus, Equation 2.1 becomes

$$\frac{dC}{dt} = K' \frac{A}{m_{\text{SW}}} (C_{\text{sat}} - C) \quad (2.3)$$

Equations 2.1, 2.2, 2.3 state that the rate of hydrate decomposition is dependent on the desorption rate and on the time the methane molecules need to cross the diffusive sublayer. The equations furthermore illustrate that dissolution is essentially diffusion controlled if $k_r \gg k_d$ (i.e. if desorption is much faster than diffusional mass transfer), and reaction controlled if $k_d \gg k_r$. Differentiating between diffusion and reaction controlled dissolution thus necessitates observation if dC/dt is changed by altering either k_d or k_r . k_r of a given soluble solid is exclusively temperature dependent. A detailed treatment of methane hydrate dissociation kinetics and an empirical correlation of k_r and T is provided by Kim et al. (1987). Diffusional mass transfer was extensively studied in alabaster ($\text{CaSO}_4 \cdot 2\text{H}_2\text{O}$) experiments carried out by Santschi et al. (1983, 1991) and Opdyke et al. (1987). In the experiments by Opdyke et al. (1987) k_d was shown to be strongly influenced by the friction velocity u^* and governed by the following relationship:

$$k_d = 280.8\text{Sc}^{-2/3}u^*. \quad (2.4)$$

Here, $\text{Sc} = \mu/(\rho D)$, where Sc is the dimensionless Schmidt number, μ and ρ the dynamic viscosity and the density of the solvent, respectively. Although an influence of T on k_d can be expected through the temperature dependence of Sc , Opdyke et al. (1987) showed this to be insignificant. Any dissolution process is diffusion-controlled, if it can be shown that the dissolution rate increases with the stress imparted by the flow of seawater on the solid surface. Since k_r is unaffected by u^* , the reaction-related term in Equations 2.1, 2.2, 2.3 can be neglected and K' assumes the value for k_d . Equation 2.3 then takes the standard form describing mass transfer in a diffusive boundary layer model, according to which dC/dt increases proportionally with k_d or, equivalently, with z^{-1} . In case of steady seawater flow across a smooth surface u^* can be converted to bottom current speeds via

$$u_{200} = \frac{u^*}{0.044}, \quad (2.5)$$

where u_{200} is the seawater current speed 200 cm above the surface (Santschi et al., 1991).

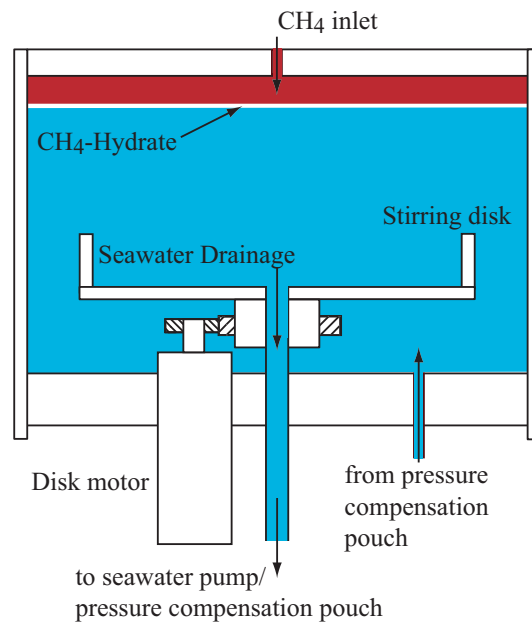


Figure 2.1: Sketch of the microcosm used in the present experiments.

2.3 Experimental set-up and procedure

Necessary P -/ T -conditions were established in a pressure laboratory designed to simulate marine conditions at depths of up to 5500 mbsl. Central part of the facility is a stainless steel autoclave measuring 1.4 m inner height and 0.3 m inner diameter. The vessel was filled with tap water to convey temperature and hydrostatic pressure to the seawater-filled ($S=35$ PSU) experimental chamber and its periphery. The experimental chamber consisted of a cylindrical microcosm (Tengberg et al., 2004), which measured 100 mm in height and 200 mm in diameter connected via a bore-hole in the bottom to a 3 L flexible, pressure-compensating pouch (Figure 2.1). A calibrated flow field was generated by combining the rotating action of a stirring disk with a simultaneous suction of seawater through a tube incorporated in the rotational axis of the disk. To match the requirements of our experiments, the microcosm flume was mounted upside-down. The hydrate was created in the microcosm as a layer between a free gas phase and seawater (Figure 2.1). At a density around 0.92 g cm^{-3} (the value varies depending on cage occupancy; Sloan and Koh, 2008), methane hydrate is less dense than seawater at the P -/ T - and salinity condi-

T [°C]	ρ_{SW} [kg m ⁻³]	μ_{SW} [mPa s]	$D_{CH_4} \times 10^5$ [cm ² s ⁻¹]	$C_{sat}^{(1)}$ [mmol kg ⁻¹]	$C_{sat}^{(2)}$ [mmol kg ⁻¹]	$C_{sat}^{(3)}$ [mmol kg ⁻¹]
2.0	1042	1.726	9.306	57.4	55.3 / 209.9*	50.5 / 208.6*
3.7	1041	1.638	9.859	64.4	61.4 / 204.4*	56.3 / 203.2*
9.0	1040	1.408	11.53	87.9	85.8 / 189.4*	79.2 / 188.3*

Table 2.1: Properties of the seawater used in the experiments. $P=30$ MPa, $S=35$ PSU. Seawater densities, ρ_{SW} , and dynamic viscosities, μ_{SW} , calculated according to procedures outlined in Siedler and Peters (1986), diffusion coefficients (D) after Jähne et al. (1987). Methane saturation concentrations were determined by averaging the saturation concentrations of all three isothermal experiments of a u^* set, ⁽¹⁾, and by calculations according to Tishchenko et al. (2005), ⁽²⁾, and Sun and Duan (2007), ⁽³⁾. Saturation concentrations calculated for systems where hydrate is metastably absent are marked *.

tions of our experiments. The hydrate therefore covered the surface of the seawater near the lid of the microcosm. Details of the periphery, equipped with an internal storage cylinder for methane, illumination, a monitoring camera, temperature sensors and a recirculation pump to ensure an even temperature distribution are given in Bigalke et al. (2008). The pressure laboratory with a description of the autoclave unit, the peripherals and system control will be presented elsewhere.

Preparation of the experiments is outlined in the Supporting Information Section (Appendix A). Prior to starting each experiment by applying the desired friction to the hydrate layer over a selected time interval, the initial methane concentration in the seawater, was determined. In all experiments, the initial methane concentration was less than 5% of the calculated saturation value (Table 2.1). During dissolution, hydrate continuously recrystallized at the interface, consuming methane from the gaseous methane reservoir above (Figure 2.1). To stabilize the seawater/hydrate interface at the same vertical level in the microcosm, the shrinkage of the gaseous methane reservoir had to be compensated by refilling gas from the interim storage 2-3 times over the duration of the experiment. The flux of methane from the dissolving hydrate into the seawater was determined from its concentration increase. The concentrations were measured by controlled degassing-sampling a volume of 20 mL fluid (gas + seawater) in a graded, gas-tight glass syringe calibrated to 0.2 mL accuracy. Syringe and tubing connecting sampling port and microcosm were flushed with water from the microcosm prior to taking a sample. To determine gas and seawater volumes the syringes were mounted perfectly upright in a rack specifically constructed for this purpose. Parallax errors were eliminated by reading off the gas and water volumes against a mirror fixed onto the back wall of

the rack, behind the glass syringes. Head-space samples were randomly taken from the glass syringes for chromatographic analyses to check methane concentrations in the gas phase. Analyses of fresh samples revealed molar methane fractions of around 0.96 immediately after sampling. The samples were furthermore checked for salinity using a WTW LF197 salinometer (accuracy 0.1 PSU) to assure that no leakage occurred in the experimental chamber. Depending on the selected friction velocity, samples were taken in regular time intervals of 60, 75 or 90 minutes over the entire duration of the experiment of 45-60 h, although gaps could not be avoided at later stages of the experiments. The amount of seawater drained from the system per sampling iteration was determined by linearly relating the drained seawater mass to the length of the respective sampling interval. The effect of the mass loss from sampling on the methane accumulation rate was accounted for by exchanging m_{SW} in Equation 2.3 for the linear relation $m_{SW0} - \bar{m}_L t$, where m_{SW0} is the initial mass of seawater, \bar{m}_L the average mass of seawater drained taking a sample and t a given point of time. A camcorder was mounted on top of the pressure vessel to record the optical appearance of the hydrate layer through a sight glass during one of the experiments. Images were recorded in a step modus at 1 s time increments.

The experiments were conducted at 30 MPa and at 2.0, 3.7 and 9.0 °C. P and T could be controlled to a precision of ± 0.1 bar and ± 0.1 °C, respectively. Temperatures were selected to cover the range of thermal conditions at locations where natural gas hydrates are reported as most abundant (Buffett and Archer, 2004). The 9.0 °C is close to conditions at the onset of the Late Paleocene Thermal Maximum, for which warming of bottom seawater temperatures (from initial ~ 10 °C to a maximum of ~ 15 °C) is suggested to have caused a massive dissociation of gas hydrates with large scale-release of methane to ocean and atmosphere (Dickens et al., 1995).

A pressure of 30 MPa was maintained in all experiments to ensure inter-comparability between the data sets. While P has a strong effect on the gas solubility outside the hydrate stability field, its effect on solubility within the HSF is small (Handa, 1990). T has a noticeable effect on the molecular diffusivity and therefore k_d . Furthermore, the effect of pressure on D in seawater can be neglected within the range from atmospheric pressure to 30 MPa (Boudreau, 1997). Here, experiments were run at friction velocities of 0.6, 1.0 and 1.2 cm s⁻¹ for each temperature, adding up to a total of 9 experimental runs of this type.

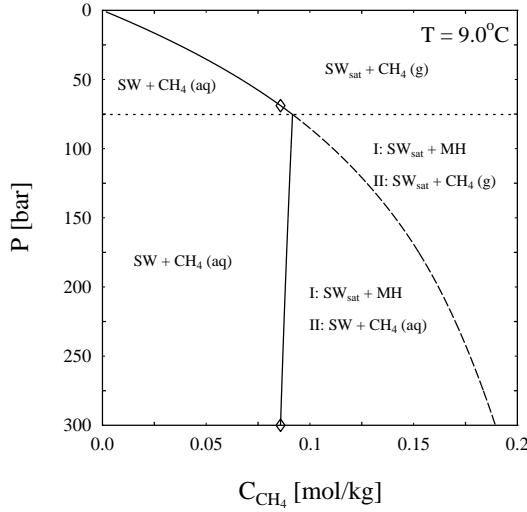


Figure 2.2: Methane solubilities in seawater (SW, $S=35$ PSU) at pressures up to 30 MPa and 9.0 °C. The dissociation pressure (P_{diss}) of methane hydrate (MH) is indicated by the dotted line. Saturation concentrations are indicated by the solid and dashed lines. At $P > P_{\text{diss}}$ and in presence of a hydrate phase (case I), the solubility decreases with pressure along the solid line. In absence of hydrate (case II) methane solubility continues to increase with pressure along the dashed line. Inter-comparison experiments to differentiate between methane transfer from dissolving hydrate and from gaseous methane were carried out at conditions marked by the two diamonds. At these pressures, methane saturation concentrations are identical, ensuring an equal thermodynamic driving force for dissolution. P_{diss} and case I saturation concentrations calculated after Tishchenko et al. (2005), saturation concentrations in the absence of hydrate after Duan and Mao (2006).

Two additional experiments outside the field of hydrate stability was carried out to study the differences between methane transfer from hydrate and pure gas/seawater interfaces. For these experiments, pressure and temperature were set to 6.9 MPa and 9.0 °C and methane transfer rates were determined with the operational settings of the microcosm set to establish friction velocities (u^*) of 0.6 and 1.2 cm s^{-1} at a no-slip interface. The methane solubility at the selected P -/ T -conditions equals that of the experiments carried out in presence of hydrate at 9.0 °C and 30 MPa. Thus it was ensured that the thermodynamic driving force (ΔC) for dissolution was identical in both scenarios (Figure 2.2).

The visually determined gas volumes in a sample were converted to moles of methane taking into account ambient room temperatures and pressures and the mole fraction of methane in the gas phase. Molar volumes of methane were

determined using the Soave modified version of the Redlich-Kwong Equation of State (Soave, 1972). The amount of methane in the liquid phase was calculated assuming gas saturation according to Duan and Mao (2006) for ambient pressures and temperatures and corresponding seawater densities. To obtain overall mass transfer coefficients (K') and saturation concentrations, the experimentally determined methane concentrations in the seawater were fitted to

$$C_t = C_{t0} + C_{\text{sat}} \left(1 - e^{-K't - \frac{A}{m_{\text{SW}}}} \right) \quad (2.6)$$

Equation 2.6 is derived from Equation 2.3 and gives the concentration of methane

in the seawater at any given point of time during an experiment. C_{t0} and C_t are the concentrations of methane in the seawater at the beginning and at time t of the experiment, respectively. For each experiment, K' and C_{sat} were obtained by minimizing the sum of residual squares between the experimental values of C_t and those calculated from Equation 2.6. The procedure was based on the Marquardt-Levenberg algorithm (Gill et al., 1982). The overall mass transfer coefficient K' in Equation 2.6 has the dimension $\text{kg h}^{-1} \text{m}^{-2}$. For better inter-comparability with literature data, K' was converted into mm h^{-1} by division with the seawater density at P , T and S conditions of the respective experiment.

2.4 Results

Experimental conditions, seawater densities (ρ_{SW}), diffusion coefficients and experimentally determined methane solubilities are listed in Table 2.1. The experimentally derived saturation concentration is the mean of the saturation calculated for the individual experiments at identical P -/ T -conditions for the three different friction velocities applied. For comparison, Table 2.1 also lists solubilities calculated according to methods proposed by Tishchenko et al. (2005) and Sun and Duan (2007). The listed diffusion coefficients were calculated from Schmidt numbers (Sc) after Jähne et al. (1987).

The calculated solubilities in Table 2.1 are given for seawater coexisting with a hydrate phase as well as for seawater in the absence of hydrate; i.e. when solubility is governed by equilibrium with the free gas phase. For the latter case, the algorithms outlined in Tishchenko et al. (2005) and Sun and Duan (2007) yield very similar results. The predicted equilibrium concentrations in the presence of a hydrate phase disagree by approx. 10%. Saturation concentrations derived from the fit of our data clearly indicate control by equilibrium with the hydrate phase and are only slightly higher than the values calculated according to Tishchenko et al. (2005). Discrepancy with the results obtained by the method of Sun and Duan (2007) is higher with a maximum of 8.1 mmol kg^{-1} absolute difference in the 3.7°C data set. Interestingly, our experimental data for C_{sat} are closer to the values calculated after Tishchenko et al. (2005), than the two published algorithms differ relative to each other.

Figure 2.3 shows exemplary images of a typical experimental run. After the build-

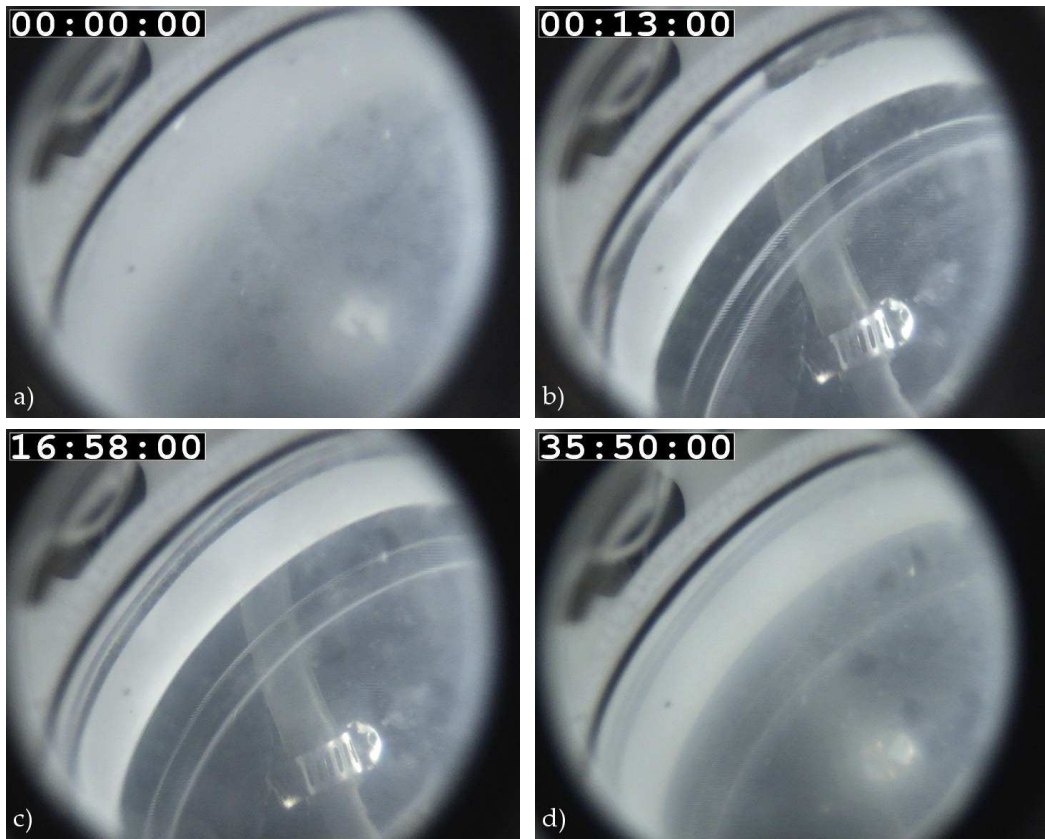


Figure 2.3: Representative images showing different stages of a typical experiment. The view is from top revealing a quadrant of the cylindrical microcosm and tubing below the device. Images 1-4 are described clockwise starting from the top left. Image 1: at zero friction velocity, just before starting the stirring mechanism, the hydrate is clearly visible as an opaque layer at the interface between gas and artificial seawater. After applying the friction to the hydrate layer, the interface gradually cleared and became perfectly transparent (Image 2). The slow recurrence of the opaque layer, indicated a thickening of the hydrate layer (Image 3). After approx. 36 h the hydrate layer was almost as thick as at the beginning of the experiment (Image 4). Experimental conditions: $P=30$ MPa, $T=3.7^{\circ}\text{C}$, $u^*=1.2\text{ cm s}^{-1}$.

up of a well visible hydrate layer during thermal adjustment to the selected conditions without shear stress (Figure 2.3 a)), the appearance of the hydrate layer gradually changed from opaque to perfectly translucent after starting the stirring mechanism (Figure 2.3 b)). In fact, visual evidence for the presence of hydrate was lacking at this stage of the experiment for at least 10 h (Figure 2.3 b), c)), at least within the limits of our relatively simple optical apparatus. The data gathered nevertheless clearly indicate that the perfect transparency was due to a mere thinning out of the hydrate layer, which apparently was still thick enough to (a) keep the surface in a no-slip condition, and (b) govern the solubility of methane in the liquid phase

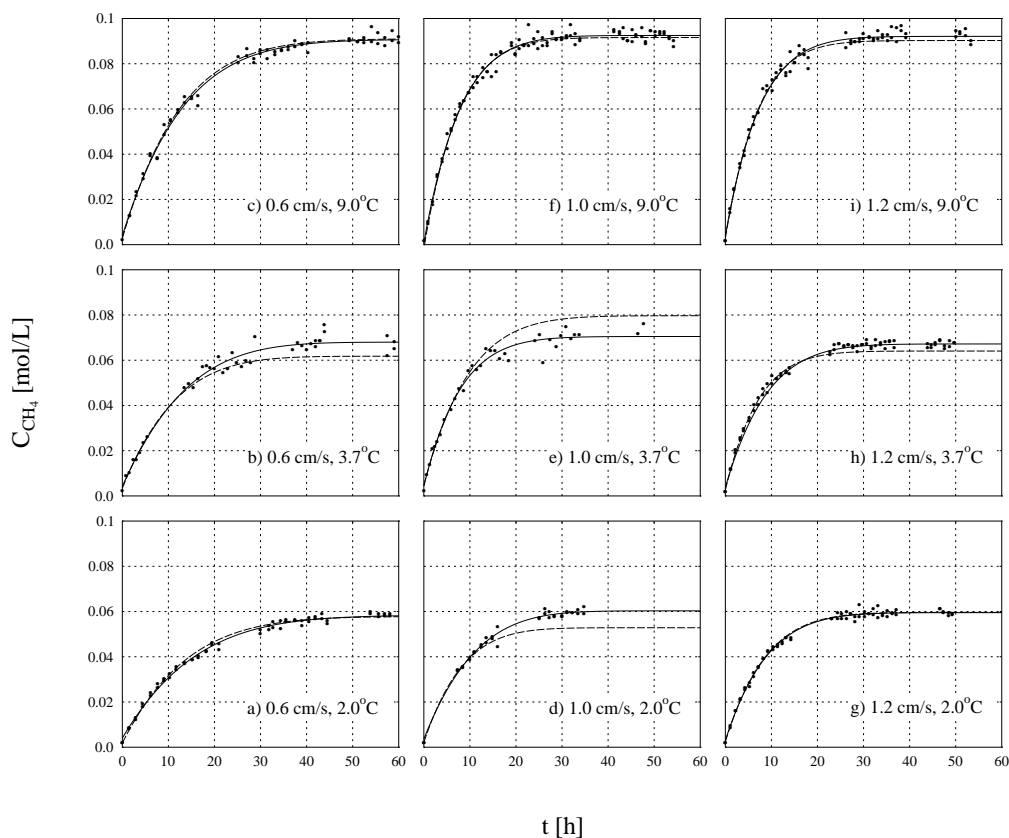


Figure 2.4: Increase of the methane concentration in seawater ($S=35$ PSU) as determined in the flux chamber experiments (dots). Corresponding curve fits (solid lines) were obtained using Equation 2.6. Dashed lines show optimized curves using the data points gained only within the first 10 h, during which a perfectly translucent interface gave no visual proof for the presence of hydrate (Figure 2.3). The match with the solid lines is generally good, indicating the presence of a rigid hydrate layer during this experimental period. Friction velocities and temperatures are indexed, P was kept constant at 30.0 MPa.

(see discussion). While transformation time of the hydrate layer appearance from opaque to translucent depended on friction velocity and methane solubility, it was limited to time increments shorter than taking the second sample, even at lowest friction velocities and thermodynamic driving force of dissolution (ΔC). With progressing time of the experiment, methane accumulated in the liquid phase and a gradual return of the opacity indicated a re-thickening of the hydrate layer (Figure 2.3 c), d)).

Experimental results and corresponding curve fits according to Equation 2.6 are shown in Figure 2.4. Values of K' and C_{sat} obtained by the optimization procedure

u^* [cm ⁻¹]	2.0 °C		3.7 °C		9.0 °C	
	C_{sat} [mmol kg ⁻¹]	k_d [mm h ⁻¹]	C_{sat} [mmol kg ⁻¹]	k_d [mm h ⁻¹]	C_{sat} [mmol kg ⁻¹]	k_d [mm h ⁻¹]
0.4	-	7.6	-	-	-	-
0.6	55.8(3)	12.6(3)	65.2(8)	13.8(8)	86.9(4) 84.5(5)*	14.7(3) 9.9(3)*
1.0	57.7(6)	17.9(4)	68.1(9)	21.1(14)	88.9(3)	24.5(6)
1.2	57.2(2)	21.1(6)	64.4(3)	23.1(5)	87.8(4) 88.1(25)*	27.4(7) 17.8(10)*

Table 2.2: Experimentally determined saturation concentrations and mass transfer coefficients. Quantities obtained at pressures outside the HSF (6.9 MPa) are marked *. All other data listed was obtained at 30 MPa.

are listed in Table 2.2. Observed saturation concentrations are all very close to the calculated values.

Results of the experiments conducted at P -/ T -conditions outside the HSF are shown in Figure 2.5. Also shown is the fit of the data for the corresponding experiments inside the HSF. The values of C_{sat} and k_d derived from the fit are also given in Table 2.2. While the saturation concentrations inside and outside the HSF match, k_d , obtained in the low-pressure experiments are lower by a factor of 1.5 with respect to those obtained within the HSF at identical operational settings of the microcosm.

2.5 Discussion

2.5.1 Mass transfer

The proportionality of K' on u^* clearly demonstrates that at hydrodynamic conditions similar to our experiments hydrate dissolution is a diffusion-controlled process and K' assumes the values for k_d supporting the conclusions of Rehder et al. (2004). The relationship between k_d and u^* is shown in Figure 2.6, which also shows the k_d/u^* -dependence calculated from Equation 2.4 (Opdyke et al., 1987).

The consistency between our results and Equation 2.4 is impressive, considering the dissimilarity of the materials and methods used in our experiments and in Opdyke et al. (1987), where dissolution rates of smooth alabaster plates are used to determine the relation between k_d and u^* . Apart from demonstrating the reliability

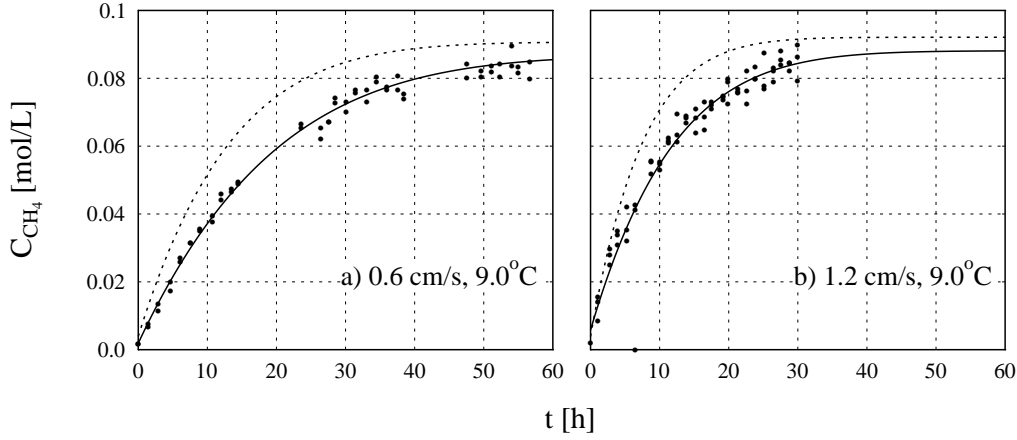


Figure 2.5: Increase of the methane concentration as determined in the experiments outside the field of hydrate stability (dots) and corresponding curve fits (solid lines). Dotted lines are curve fits corresponding to data gained at hydrate forming conditions but at equal solubility (Figures 2.4c, 2.4i). The experiments were carried out at 6.9 MPa.

of the experimental data the consistency also indicates the functional efficiency of the microcosm. Using the mass transfer coefficients and the molecular diffusion coefficients, the thickness of the diffusive boundary layer was calculated and related to the experimental friction velocities via the following empirical fit:

$$z = 0.0173u^{*-0.97} \quad (2.7)$$

Here, z is given in cm, u^* in cm s^{-1} . The graph of Equation 2.7 and the experimentally determined dbl thicknesses are shown in Figure 2.7. Since $K' = k_d = D/z$, Equations 2.1 and 2.7 can be re-written to yield a universally applicable expression for the flow-dependent transfer of methane from clean hydrate outcrops dissolving at the seafloor:

$$\frac{dn}{dt} = \frac{D}{0.0173u^{*-0.97}} A(C_{\text{sat}} - C_{\text{bulk}}) \approx \frac{D}{0.0173u^{*-0.97}} AC_{\text{sat}} \quad (2.8)$$

In most oceanic settings, the background concentration of methane in the seawater is close to zero and can be neglected. With Equation 2.8 allowing the calculation of the methane flux caused by dissolution of outcropping methane hydrates at the seafloor, it is just necessary to measure the bottom water methane concentration and u^* . Latter can be assessed from current meter data close to the seafloor and

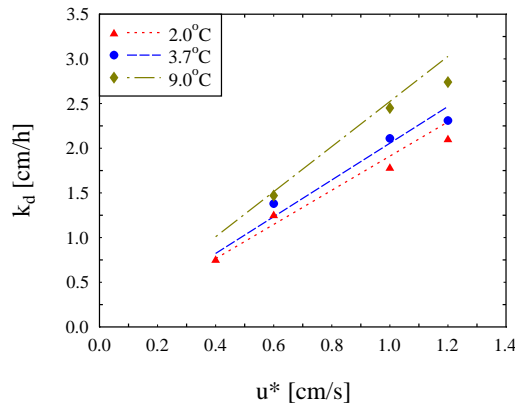


Figure 2.6: Dependence of the mass transfer coefficient, k_d , of methane from a hydrate film on the friction velocity u^* . Experimental observations are represented by the symbols, lines denote the relationship established by Opdyke et al. (1987, Equation 2.4).

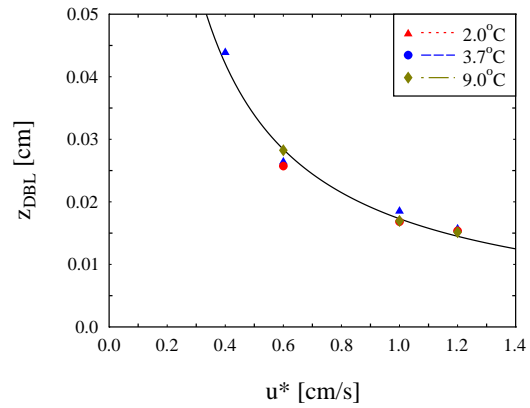


Figure 2.7: Dependence of the diffusive boundary layer thickness, z , on the friction velocity, u^* . Symbols as in Figure 2.6.

Equation 2.5. However, it has to be emphasized that methane hydrate outcrops at the seafloor are usually accompanied by the flux of methane-rich fluids and free gas, all adding to the total methane flux from such a natural setting. Another important implication of Equation 2.8 is its ability to quantitatively assess the minimal rate of continuous hydrate regrowth at natural hydrate outcrops. Rehder et al. (2004) stated that sustaining natural hydrates at the seafloor requires continuous reformation beyond compensation of hydrate dissolution, and that changes in the appearance of such hydrate formations on a yearly time scale (MacDonald et al., 1994, 2003) could be explained by changes in the reformation rate rather than by changes in the thermal regime or mechanical disruption of parts of the hydrate outcrop. The rate of hydrate formation for these settings has so far not been implemented in any model simulation.

2.5.2 Pure gas dissolution experiments

At identical saturation concentrations and microcosm flume settings, experimentally determined transfer of methane into the seawater was slower by a factor of 1.5 in a two-phase system consisting of methane gas and seawater compared to the case of the two phases separated by an additional hydrate layer (Figure 2.5, Table 2.2). In the presence of a hydrate layer, the interface between the watery phase

and the hydrate is immobile, i.e. no-slip conditions prevail. The calibrated control of u^* in the microcosm is based on an immobile interface. Without a solid layer, the interface between the watery phase and the gas phase experiences a slip condition. As a result, the transfer of momentum from the water to the gas will result in movements of the interface in direction of the shear stress vector, which results in a lowering of u^* at the interface. We therefore hypothesize that the factor of 1.5 reduction of gas transfer into the seawater in the absence of hydrate is due to a reduced friction between the two phases. For our experiments, the flow field is governed by the forcing of rotor and pump of the microcosm flume, and the calibration of u^* only holds for no-slip conditions at the interface. The slip boundary condition for a hydrate-free gas-water interface reduces the drag, and as a consequence, the transfer coefficient k_d .

2.5.3 Validity of experimental approach

The uptake rate of methane by the seawater in the experiments outside the HSF strongly indicates that for the experiments within the hydrate stability field, dissolution is indeed governed by hydrate-controlled solubility and a non-mobile interface, even in the time interval, where the hydrate layer was not detectable by our optical means (Figure 2.3). If hydrate had completely dissolved and left the system, transfer of methane into the seawater would have been governed by direct solution of the methane gas rather than by hydrate dissolution. Consequently, the appropriate methane saturation concentration would have corresponded to a system in which hydrate was absent, i.e. governed by equilibrium with the free gas phase. Since solubilities in this case would have been considerably higher than in the presence of hydrates (Table 2.1, Figure 2.2), an increase of dissolution rates should have been observed. If, in the early phase of the experiments within the HSF, the thinning or even a partial absence of hydrates at the interface had led to hydrate-controlled solubility but a moving interface, then reduced dissolution rates should have been observed. This is suggested by the results from outside the HSF. Both potential effects are inconsistent with the experimental findings. In fact, the curves obtained by fitting Equation 2.2 to the data points gathered exclusively in the first 10 h, in which optical evidence of a hydrate layer at the interface was missing, generally yield a very similar progression compared to the fit obtained using the whole data set (Figure 2.4). The comparison shows no systematic devi-

ation of the data from the fit to Equation 2.5. This implies that the hydrate layer must have been intact, without shear-induced motion, and effectively separating gas from liquid at all times of the experiments, validating this approach to derive hydrate dissolution rates.

2.5.4 Comparison to earlier data and postulations

Without experimental evidence, (Egorov et al., 1999) suggested diffusion-controlled hydrate dissolution. They calculated a flux rate of 50 m^3 of methane gas (STP) $\text{m}^{-2} \text{ a}^{-1}$ for methane hydrates that outcrop on the sea floor and are exposed to seawater flow, based on rough estimates of z (0.1 cm) and D ($10^{-5} \text{ cm}^2 \text{ s}^{-1}$). For the saturation concentration, they appear to have adopted a value of 1200 mL L^{-1} (i.e. $\sim 54 \text{ mmol L}^{-1}$), based on the equilibrium concentration at the three-phase boundary at the temperature of their working area, the Håkon Mosby Mud Volcano. If we follow this rather crude approach explicitly, we derive a flux of 38 m^3 of methane $\text{m}^{-2} \text{ a}^{-1}$; so apparently the result has been rounded to reflect the rather crude assumptions made. The postulated flow rate of 50 m^3 of methane gas (STP) $\text{m}^{-2} \text{ a}^{-1}$ surely matches the right order; however the diffusion control assumed in Egorov et al. (1999) was not justified by any experimental data at that time.

From the experiments carried out by Rehder et al. (2004), methane flux rates of $370 \mu\text{mol m}^{-2} \text{ s}^{-1}$ were derived from diameter shrinkages of cylindrical synthetic methane hydrate specimens exposed to cross flow of undersaturated seawater. The experiments were performed on the ocean floor at Monterey Bay at 10.48 MPa and 3.5°C . For these conditions Rehder et al. (2004) report a methane solubility of 69.8 mmol L^{-1} , and a corresponding molecular diffusion coefficient of $9.956 \cdot 10^{-6} \text{ cm}^2 \text{ s}^{-1}$ in accordance to Jähne et al. (1987). The current velocity was not measured. Recently, Hester et al. (2008) reinterpreted these data by applying an empirical correlation for transfer of heat from heated cylindrical specimens in a cross flow of air and derived a flow velocity of 1.75 cm s^{-1} around the hydrate specimens in Monterey Bay. Applying Equation 2.8, a friction velocity of 0.08 cm s^{-1} (obtained from a bottom water current speed of 1.75 cm s^{-1} and Equation 2.5), and the C_{sat} and D values reported in Rehder et al. (2004), we calculate a flux rate of $33.4 \mu\text{mol m}^{-2} \text{ s}^{-1}$ from hydrates that outcrop the seafloor and are exposed to an identical contour-following mean flow. The discrepancy in dissolution rate by an order of magnitude demonstrates the different hydrodynamic boundary conditions

resulting from cross flow (Rehder et al., 2004) an parallel boundary-layer flow (this work). The comparison illustrates the importance of a robust characterization of the local u^* and shape of a particular hydrate outcrop if its fate is to be assessed. Hydrate formation in excess of dissolution (the latter depending on the prevailing current regime) will lead to lateral but also vertical growth of the hydrate (MacDonald et al., 1994). The latter leads to an increased surface area, but also, and maybe more importantly, to enhanced local shear. The size and appearance of hydrate outcrops is thus governed by the balance of regrowth and dissolution. With the latter being flow-dependent, the methane dissolution rate under parallel flow thus determines the minimal formation rate required to maintain surface hydrates under the prevailing bottom current conditions for which numerical algorithms can be formulated now that the key variables and processes have been identified.

Implications

With the parameters chosen for our experiments, we cover the temperature range for almost all hydrate-bearing upper seafloor regions of the present ocean. The 9.0°C experiments also correspond to deep-ocean temperatures at the beginning of the carbon excursion of the LPTM, for which a rapid liberation of methane from the marine gas hydrate pool has been suggested (Dickens et al., 1995; Katz et al., 1999). Inside the hydrate stability field, the change in C_{sat} with P for a given T is small (Handa, 1990; Tishchenko et al., 2005; Sun and Duan, 2007). Based on the results presented here, a correlation was derived according to which the methane flux from dissolution of plain methane hydrates paving the seafloor can be calculated (Equation 2.8). The input parameters C_{sat} and D may be derived by the procedures outlined in (Tishchenko et al., 2005) or (Sun and Duan, 2007) and Jähne et al. (1987), respectively, while friction velocities can be derived from current speeds using Equation 2.5, if the flow is parallel to the decomposing hydrate surface.

As reasoned above, the calculation of the dissolution rate constrains the minimal rate of hydrate formation in settings where hydrates are exposed at the seafloor surface. Natural hydrate outcrops usually build elevations on the seafloor or are covered by thin sedimentary layers, thereby deviating from the ideal case of a smooth, clean hydrate surface considered here. Therefore, hydrate formation rates must be higher or lower, respectively than results derived from Equation 2.8 indicate. The

experimental proof that hydrate dissolution is diffusion controlled and the fact that our k_d/u^* relationship excellently agrees with an established correlation (Opdyke et al., 1987) indicate that the problem of assessing and modeling the methane flux from natural outcrops can be reduced to a sound description of the hydrodynamic conditions. However, experimental work is required to address the dissolution kinetics of non-pure methane hydrate, for which both the solubility and the understanding of the processes at the phase boundary during dissolution are less well constrained.

Acknowledgments

We thank Andreas Meyer for his skillful technical support during the experimental work. Funding was provided by the German Federal Ministry of Education and Science (BMBF) and German Research Foundation (DFG) (Grant 03G0600D) as well as by the European Union within the EU FP6 Integrated Project CARBOOCEAN (contract no. 511176).

Supporting Information Available

Auxiliary material consisting of a detailed description of the preparation of the experiments (cf. Appendix A).

References

- Bigalke, N. K.; Rehder, G.; Gust, G. Experimental investigation of the rising behavior of CO₂ droplets in seawater under hydrate forming conditions. *Environ. Sci. Technol.*, **42**, 2008, 5241–5246.
- Boudreau, B. P. *Diagenetic Models and their Implementation - Modelling Transport and Reactions in Aquatic Sediments*. Springer-Verlag, Berlin 1997.
- Brewer, P.; Paull, C. K.; Peltzer, E. T.; Ussler, W. I.; Rehder, G.; Friederich, G. Measurements of the fate of gas hydrates during transit through the ocean water column. *Geophys. Res. Lett.*, **29**, 2002, doi: 10.1029/2002GL014727.

- Buffett, B.; Archer, D. Global inventory of methane clathrate: sensitivity to changes in the deep ocean. *Earth Planet. Sci. Lett.*, 227, **2004**, 185–199.
- Chapman, N. R.; Pohlman, J. W.; Coffin, R. B.; Chanton, J. P.; Lapham, L. Thermogenic gas hydrates in the northern Cascadia Margin. *EOS*, 85, **2004**, 361–365.
- Dickens, G. R.; O'Neil, J. R.; Rea, D. K.; Owen, R. M. Dissociation of oceanic methane hydrate as a cause of the carbon-isotope excursion at the end of the Paleocene. *Paleoceanography*, 10, **1995**, 965–971.
- Duan, Z.; Mao, S. A thermodynamic model for calculating methane solubility, density and gas phase composition of methane-bearing aqueous fluids from 273 to 523 K and from 1 to 2000 bar. *Geochim. Cosmochim. Acta*, 70, **2006**, 3369–3386.
- Egorov, A. V.; Crane, K.; Vogt, P. R.; Rozhkov, A. N. Gas hydrates that outcrop on the seafloor: stability models. *Geo-Mar. Lett.*, 19, **1999**, 68–75.
- Gill, P. E.; Murray, W.; Wright, M. H. *Practical Optimization*. Academic Press, London **1982**.
- Gunderson, J. K.; Jørgensen, B. B. Microstructure of diffusive boundary layers and the oxygen uptake of the sea floor. *Nature*, 345, **1990**, 604–607.
- Handa, Y. P. Effect of hydrostatic pressure and salinity on the stability of gas hydrates. *J. Phys. Chem.*, 94, **1990**, 2652–2657.
- Heeschen, K.; Keir, R. S.; Rehder, G.; Klatt, O.; Suess, E. Methane dynamics in the Weddell Sea determined via stable isotope ratios and CFC-11. *Global Biogeochem. Cycles*, 18, **2004**, doi: 10.1029/2003GB002151.
- Hesselbo, S. P.; Gröcke, D. R.; Jenkyns, H. C.; Bjerrum, C. J.; Farrimond, P.; Morgans Bell, H. S.; Green, O. R. Massive dissociation of gas hydrate during a Jurassic oceanic anoxic event. *Nature*, 406, **2000**, 392–395.
- Hester, K.; Peltzer, E. T.; Dunk, R. M.; Walz, P.; Brewer, P. G. Can hydrate dissolution experiments predict the fate of a natural hydrate system? In *6th International Conference on Gas Hydrates*. Vancouver **2008**, 7.
- Jähne, B.; Heinz, G.; Dietrich, W. Measurement of the diffusion coefficients of sparingly soluble gases in water. *J. Geophys. Res.*, 92, **1987**, 10767–10776.

- Katz, M. E.; Pak, D. K.; Dickens, G. R.; Miller, K. G. The source and fate of massive carbon input during the Latest Paleocene Thermal Maximum. *Science*, 286, **1999**, 1531–1533.
- Kennett, J. P.; Cannariato, K. G.; Hendy, I. L.; Behl, R. J. Carbon isotopic evidence for methane hydrate instability during Quaternary interstadials. *Science*, 288, **2000**, 128–133.
- Kim, H. C.; Bishnoi, P. R.; Heidemann, R. A.; Rizvi, S. S. H. Kinetics of Methane Hydrate Decomposition. *Chem. Eng. Sci.*, 42, **1987**, 1645–1653.
- Lelieveld, J.; Crutzen, P. J. Changing concentration, lifetime and climate forcing of atmospheric methane. *Tellus*, 50, **1998**, 128–150.
- MacDonald, I. R.; Guinasso, N. L.; Sassen, R.; Brooks, J. M.; Lee, L.; Scott, K. T. Gas hydrate that breaches the sea floor on the continental slope of the Gulf of Mexico. *Geology*, 22, **1994**, 699–702.
- MacDonald, I. R.; Sager, W. W.; Peccini, M. B. Gas hydrate and chemosynthetic biota in mounded bathymetry at mid-slope hydrocarbon seeps: Northern Gulf of Mexico. *Mar. Geol.*, 198, **2003**, 133–158.
- Milkov, A. V. Global estimates of hydrate-bound gas in marine sediments: how much is really out there? *Earth-Sci. Rev.*, 66, **2004**, 183–197.
- Nihous, G. C.; Masutani, S. M. Notes on the dissolution rate of gas hydrates in undersaturated seawater. *Chem. Eng. Sci.*, 61, **2006**, 7827–7830.
- Opdyke, B. N.; Gust, G.; Ledwell, J. R. Mass transfer from smooth alabaster surfaces in turbulent flows. *Geophys. Res. Lett.*, 14, **1987**, 1131–1134.
- Park, Y.; Kim, D.-Y.; Lee, J.-W.; Huh, D.-G.; Park, K.-P.; Lee, J.; Lee, H. Sequestering carbon dioxide into complex structures of naturally occurring gas hydrates. *Proc. Nat. Acad. Sci. U.S.A.*, 103, **2006**, 12690–12694.
- Paull, C. K.; Brewer, P. G.; Ussler, W. I.; Peltzer, E. T.; Rehder, G.; Clague, D. An experiment demonstrating that marine slumping is a mechanism to transfer methane from seafloor gas-hydrate deposits into the upper ocean and atmosphere. *Geo-Mar. Lett.*, 22, **2003**, 198–203.

- Rehder, G.; Keir, R. S.; Suess, E.; Rhein, M. Methane in the northern Atlantic controlled by oxidation and atmospheric history. *Geophys. Res. Lett.*, **26**, **1999**, 587–590.
- Rehder, G.; Kirby, S. H.; Durham, W. B.; Stern, L. A.; Peltzer, E. T.; Pinkston, J.; Brewer, P. Dissolution rates of pure methane hydrate and carbon-dioxide hydrate in undersaturated seawater at 1000-m depth. *Geochim. Cosmochim. Acta*, **68**, **2004**, 285–292.
- Santschi, P. H.; Anderson, R. F.; Fleisher, M. Q.; Bowles, W. Measurements of diffusive sublayer thicknesses in the ocean by alabaster dissolution, and their implications for the measurements of benthic fluxes. *J. Geophys. Res.*, **96**, **1991**, 10641–10657.
- Santschi, P. H.; Brower, P.; Nyffeler, U. P.; Azevedo, A.; Broecker, W. S. Estimates of the resistance to chemical-transport posed by the deep-sea boundary-layer. *Limnol. Oceanogr.*, **28**, **1983**, 899–912.
- Siedler, G.; Peters, H. Properties of seawater, physical properties (general). In Sündermann, J. (ed.), *Landolt-Börnstein Oceanography; New Series V/3a*, vol. New Series V/3a. Springer-Verlag, Berlin **1986**, 233–264.
- Sloan, E. D.; Koh, C. A. *Clathrate hydrates of natural gases.*, vol. 119 of *Chemical Industries*. CRC Press, New York, 3rd ed. **2008**.
- Soave, G. Equilibrium Constants from a Modified Redlich-Kwong Equation of State. *Chem. Eng. Sci.*, **27**, **1972**, 1197–1203.
- Suess, E.; Torres, M. E.; Bohrmann, G.; Collier, R. W.; Rickert, D.; Goldfinger, C.; Linke, P.; Heuser, A.; Sahling, H.; Heeschen, K.; Jung, C.; Nakamura, K.; Greinert, J.; Pfannkuche, O.; Trehu, A.; Klinkhammer, G.; Whiticar, M. J.; Eisenhauer, A.; Teichert, B.; Elvert, M. Sea Floor Methane Hydrates at Hydrate Ridge, Cascadia Margin. In Paull, C. K.; Dillon, W. P. (eds.), *Natural Gas Hydrates: Occurrence, Distribution, and Detection.*, vol. 124 of *Geophysical Monograph Series*. American Geophysical Union, Washington, DC **2001**, 87–98.
- Sun, R.; Duan, Z. An accurate model to predict the thermodynamic stability of methane hydrate and methane solubility in marine environments. *Chem. Geol.*, **244**, **2007**, 248–262.

- Tengberg, A.; Stahl, H.; Gust, G.; Müller, V.; Arning, U.; Andersson, H.; Hall, P. O. J. Intercalibration of benthic flux chambers I. Accuracy of flux measurements and influence of chamber hydrodynamics. *Prog. Oceanogr.*, 60, **2004**, 1–28.
- Tishchenko, P.; Hensen, C.; Wallmann, K.; Wong, C. S. Calculation of the stability and solubility of methane hydrate in seawater. *Chem. Geol.*, 219, **2005**, 37–52.
- Wedler, G. *Lehrbuch der Physikalischen Chemie*. Wiley-VCH, Weinheim, 5th ed. **2007**.

3 Experimental investigation of the rising behavior of CO₂ droplets in pressurized seawater under hydrate forming conditions

Nikolaus K. Bigalke^{*1}, Gregor Rehder², Giselher Gust³

Leibniz Institute of Marine Sciences at the University of Kiel, Wischhofstr. 1-3,
24114 Kiel, Germany

nbigalke@ifm-geomar.de

Abstract

In a laboratory-based test series, seven experiments along a simulated Pacific hydrotherm at 152 °W, 40 °N were carried out to measure the rise velocities of liquefied CO₂ droplets under (clathrate) hydrate forming conditions. The impact of a hydrate skin on the rising behavior was investigated by comparing the results with those from outside the field of hydrate stability at matching buoyancy. A thermostatted high pressure tank was used to establish conditions along the natural oceanic hydrotherm. Under *P-/T*-conditions allowing hydrate formation, the majority of the droplets quickly developed a skin of CO₂ hydrate upon contact with seawater. Rise rates of these droplets support the parameterization by Chen et al. (2003), which is based on empirical equations developed to match momentum of hydrate covered, deformed droplets. Our data do not support other parameterizations recently suggested in the literature. In the experiments from 5.7 MPa, 4.8 °C to

¹phone: +49 431 600-1410, fax:+49 431 600-1400

²Leibniz Institute for Baltic Sea Research at the University of Rostock, Seestr. 15, 18119 Rostock, Germany

³Technical University Hamburg-Harburg, Department of Ocean Engineering, Schwarzenbergstr. 95, 21073 Hamburg, Germany

11.9 MPa, 2.8 °C positive and negative deviations from predicted rise rates occurred, which we propose were caused by lacking hydrate formation and reflect intact droplet surface mobility and droplet shape oscillations, respectively. This interpretation is supported by rise rates measured at P -/ T -conditions outside the hydrate stability field at same liquid CO₂-seawater density difference ($\Delta\rho$) matching the rise rates of the deviating data within the stability field. The results also show that droplets without a hydrate skin ascend up to 50% faster than equally buoyant droplets with a hydrate skin. This feature has a significant impact on the vertical pattern of dissolution of liquid CO₂ released into the ocean. The experiments and data presented considerably reduce the uncertainty of the parameterization of CO₂ droplet rise velocity, which in the past emerged partly from their scarcity and contradictions in constraints of earlier experiments.

3.1 Introduction

With the demand of energy from fossil fuels expected to rise throughout the first half of this century at least, stabilization of atmospheric CO₂ concentrations at levels of 450-750 ppmv requires prevention of CO₂ emissions into the atmosphere in the order of 10²-10³ Gt CO₂ within this century (IPCC, 2005). To meet this requirement, ocean storage of fossil fuel derived CO₂ is being considered among other carbon capture and storage (CCS) strategies (IPCC, 2005). Results of the following study address scenarios of liquid CO₂ release into the water column at depths between the CO₂/seawater density inversion and the CO₂ liquid/gas phase boundary (Figure 3.1). Liquid CO₂ release might occur either intentionally by direct injection into the water column or by accidental seepage from sub-sedimentarily stored CO₂. Figure 3.1 shows that for the depth range under consideration the P -/ T -conditions generally allow hydrate formation. Several investigators have observed that hydrate readily crystallizes at the interface between liquid CO₂ and seawater to form skins around the droplets (e.g. Brewer et al., 2006, 2002; Ozaki et al., 2001; Radhakrishnan et al., 2003; Holder et al., 1995; Hirai et al., 1997). The low density liquid creates plumes of ascending droplets with CO₂ dissolving into the surrounding seawater (Alendal and Drange, 2001). Among the factors influencing the vertical distribution of dissolved CO₂ is the droplets' terminal rise velocity, u_T . u_T has been modeled in a variety of approaches in several publications

(e.g. Chen et al., 2003; Holder et al., 1995; Hirai et al., 1997; Alendal and Drange, 2001; Gangstø et al., 2005; Zhang, 2005). However, experimental data on the behavior of CO_2 under controlled thermodynamic conditions is scarce. Observations made in a field experiment (Brewer et al., 2002) have been used repeatedly as a reference for model calculations of u_T . Brewer et al. (2002) used a simplified buoyancy equation adopted from Holder et al. (1995) to match the observed velocities. Zhang (2005) pointed out that this equation cannot be employed in general and used a function approximating the standard drag curve of a rigid sphere instead. This had been common practice in other works (Hirai et al., 1997), in which droplets were assumed to behave as rigid spheres upon formation of hydrate skins. It was shown by Ozaki et al. (2001) that deformation of hydrate-coated droplets does occur and this and follow-up studies (Chen et al., 2003; Gangstø et al., 2005) demonstrate that rise velocities can be overestimated using the rigid sphere theory. Gangstø et al. (2005) applied a model based on experiments with air bubbles and a variety of liquids under atmospheric pressure (Bozzano and Dente, 2001). Four out of five observational points in Brewer et al. (2002) were well matched; however, due to the limited depth range of the experiments, potential perturbations and the scarcity of observational points, the validity of this parameterization is uncertain. Furthermore, the model needs to be expanded in order to be valid for systems with a liquid (rather than gas) as dispersed phase. Chen et al. (2003) developed a semi-empirical parameterization of the rise velocity to successfully match observations made in tank experiments (Ozaki et al., 2001) at three different P -/ T -conditions, however outside

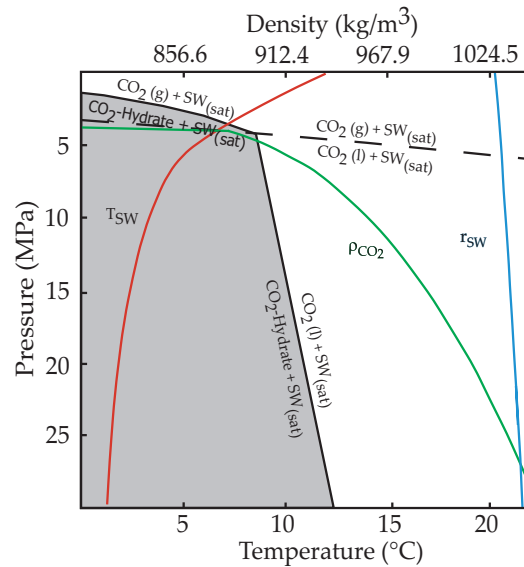


Figure 3.1: Phase diagram of CO_2 and seawater. The gray area marks the stability field of CO_2 clathrate hydrate. Also shown is the gas/liquid phase transition for pure CO_2 . The red line denotes a depth - temperature profile of the Pacific Ocean at 152°W , 40°N (WoceCTD station no. 6819) (Schlitzer, 2007). Green and blue lines denote densities of CO_2 and seawater (35.0 PSU), respectively at P -/ T -conditions given by the hydrotherm. Phase boundaries calculated after Sloan (1998); seawater and CO_2 densities after Siedler and Peters (1986) and Angus et al. (1976), respectively.

typical oceanic conditions. Considerable differences exist in both the experimental data as well as the different model parameterizations. This study addresses this inconsistency by presenting a comprehensive set of rise rates of CO₂ droplets at *P*-/*T*-conditions simulating oceanic conditions within the hydrate stability field as well as at conditions outside the field of hydrate stability. The data is used to re-evaluate the different parameterizations of u_T suggested in the literature.

3.2 Experimental set-up and procedure

Necessary *P*-/*T*-conditions for hydrate formation were realized in a pressure laboratory designed to simulate marine conditions at depths of up to 5500 mbsl. Central part of the facility is a stainless steel autoclave measuring 1.4 m inner height and 0.3 m inner diameter. The vessel was filled with tap water to convey temperature and hydrostatic pressure to the inner assembly selected for the experiments. Details of the pressure laboratory are presented in Rehder et al. (2004). The inner assembly, its mode of operation and the experimental set-up are described in Section A1 of the Supporting Information. The experiments took place in stagnant synthetic seawater of 35 PSU. *P*-/*T*-conditions were selected to match discrete depths along a marine hydrotherm of the Pacific Ocean at 152 °W, 40 °N (Figure 3.1, Table 3.1). A total of seven data sets was gathered within the field of hydrate stability. Three additional datasets outside the field of hydrate stability were collected. In order to assess the effect of hydrate skin formation on the rise velocity, *P* and *T* in the additional experiments were set to values to match density differences ($\Delta\rho$) between CO₂ and seawater (and thus buoyancy forces) of three experiments from within the field of hydrate stability. An overview of the experimental conditions is given in Table 3.1. Droplet rise rates and sizes were determined optically by means of two low resolution cameras fixed at a vertical distance of 34 cm from each other next to the rising chamber inside and one high resolution camcorder filming from outside of the pressure vessel, respectively. In the images recorded, droplets appeared as dark ellipses. Their sizes were expressed by the equivalent radius, r_e , which is defined by

$$r_e = \sqrt[3]{a^2b} \quad (3.1)$$

P [MPa]	T [°C]	ρ_{CO_2} [kg m ⁻³]	ρ_{SW} [kg m ⁻³]	$\Delta\rho$ [kg m ⁻³]	P_{diss} [MPa]	Mo $\times 10^{10}$
5.7	4.8	915.1	1030.3	115.2	2.6	5.9
8.3	3.6	943.9	1031.7	87.8	2.2	5.1
9.9	3.2	957.0	1032.4	75.4	2.1	4.6
11.9	2.8	971.1	1033.4	62.3	2.0	4.0
14.7	2.5	987.2	1034.7	47.5	1.9	3.1
17.5	2.0	1002.4	1036.1	33.7	1.8	2.3
20.2	1.9	1014.1	1037.3	23.2	1.8	1.6
18.3	13.1	958.8	1034.2	75.4	40.5	1.5
22.0	13.9	974.0	1036.3	62.3	48.9	1.1
24.8	13.1	989.5	1037.0	47.5	40.5	0.9

Table 3.1: Experimental P -/ T -conditions and corresponding liquid CO_2 and seawater densities. Conditions of the experiments run outside the hydrate stability field are listed in the bottom three lines. Calculations of seawater and CO_2 densities after Siedler and Peters (1986) and Angus et al. (1976), respectively. Three-phase equilibrium pressures (P_{diss}) calculated for experimental temperatures after Sloan (1998). $\text{Mo} = g \mu_{\text{SW}}^4 / (\rho_{\text{SW}}^2 \sigma^3)$ where μ_{SW} is the dynamic viscosity of seawater (Siedler and Peters, 1986) and $\sigma = 0.023 \text{ kg/s}^2$.

with a and b being major and minor semi-axis of the ellipse, respectively. Section A2 of the Supporting Information details the analysis of the high resolution video material.

3.3 Results and Discussion

3.3.1 Droplet shape and motion characteristics

In our experiments, droplet radii varied from 0.6 to 15.0 mm, with droplet shapes shifting from spherical at small radii via regular-ellipsoidal at intermediate to irregularly deformed ellipsoids at large radii. Figure 3.2 shows the relationship between equivalent radius r_e and aspect ratio of droplets rising inside and outside of the hydrate stability field. The aspect ratio is defined as the ratio of minor and major axes of the best fitting ellipse to the droplets. Most figures show an inflection at a droplet radius around 2 mm. The slope of the aspect ratio from 2 mm onward varies with ambient pressure and temperature. There is a trend toward stronger flattening at shallower simulated seawater depth. Accordingly, the smallest change of the aspect ratio throughout the whole range of droplet radii is observable at highest pressures within the hydrate stability field,

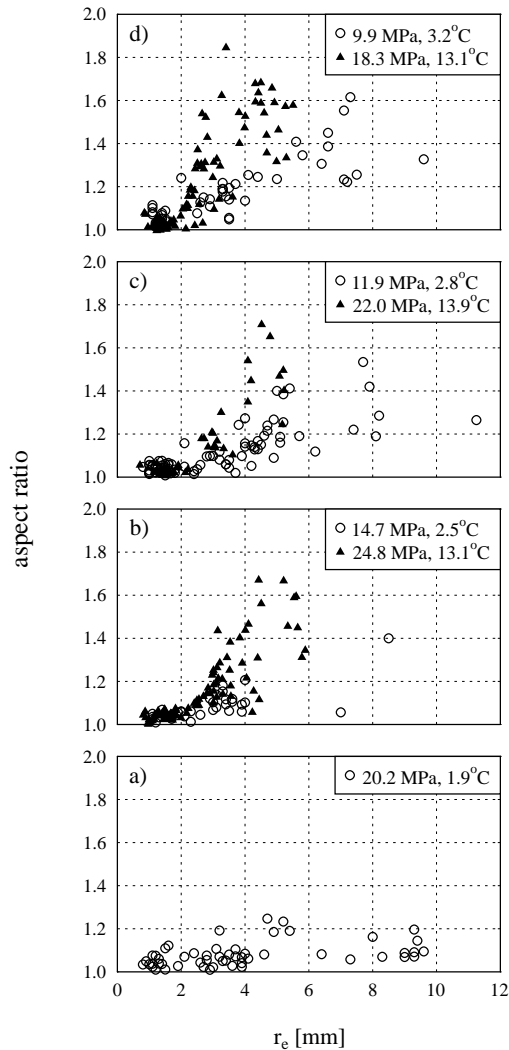


Figure 3.2: Aspect ratio, defined as the ratio of major and minor axis of droplets. Open circles and black triangles represent droplets released inside and outside the hydrate stability field, respectively. More data is available in Section A3 of the Supporting Information.

Lower buoyancy toward small diameters or high simulated seawater depths shifts droplets to more spherical shapes. Larger droplets and those released at shallower seawater depths have greater buoyancy and consequently are deformed toward ellipsoidal shapes. Droplets rising at conditions satisfying hydrate formation show less deformation than those released outside of the hydrate stability field (Fig-

at 20.2 MPa and 1.9 °C (Figure 3.2 a). Increased scatter is observed in the data sets from experiments outside the hydrate stability field. Droplet shapes can be described in terms of the relevant Morton and Eötvös numbers (Clift et al., 1978). At Morton numbers in the range of this study (Table 3.1) the shape of a droplet can be sufficiently characterized by the Eötvös number alone, which is proportional to buoyancy forces divided by interfacial tension forces (Clift et al., 1978). There seems to be no systematic investigation of the interfacial tension of CO₂ droplets in seawater at P -/ T -conditions in the range of interest in the literature. Ohmura and Mori (1998) estimate CO₂/seawater at a seawater depth of 3300 m to be 24 g/s² while Gangstø et al. (2005) set CO₂/seawater to the constant value of 23 g/s² for the range of seawater depths from 496.8 mbsl to 804.5 mbsl. We assume CO₂/seawater to be constant within the P -/ T -range of our experiments. Droplet buoyancy is proportional to the volume of the droplet and the density difference between CO₂ and seawater.

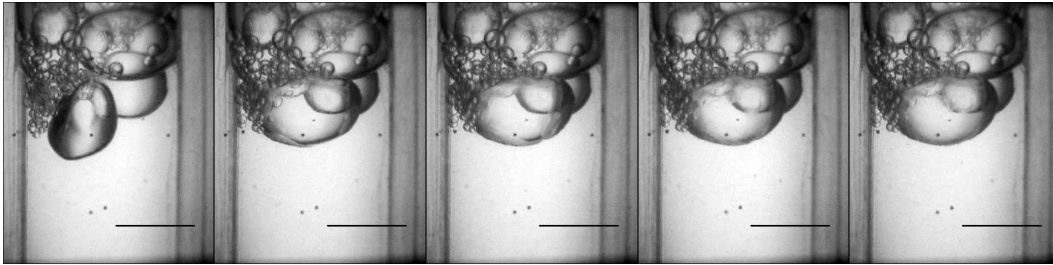


Figure 3.3: Lateral spreading of a hydrate skin around a droplet trapped under previously ascending droplets now clogging the conduit. Length scale at bottom right of each image is 10 mm, entire sequence duration is 3.4 s.

ures 3.2 b - d). This indicates that hydrate skins counter the deformation of droplets, which is in accordance with findings from field (Brewer et al., 2002) and laboratory experiments (Radhakrishnan et al., 2003). Oscillations were predominantly observed at P -/ T -conditions outside the field of hydrate stability. In general, the onset of shape oscillations coincides with vortex shedding from the wake of the droplets (Clift et al., 1978). Reynolds numbers, Re , at which vortex shedding sets in are often referred to as "lower critical Reynolds numbers", Re_{crit} . Outside of the hydrate stability field, shape oscillations set in at $r_e=3.1$ mm ($Re=670$) at 17.9 MPa, 13.1 °C; $r_e=3.5$ mm ($Re=710$) at 23.2 MPa, 13.9 °C and at $r_e=3.8$ mm ($Re=760$) at 24.3 MPa, 13.1 °C. Within the hydrate stability field oscillations were mostly suppressed. This suggests the formation of a rigid hydrate skin around the droplets. In our experiments, occasional oscillations were observed at conditions close to the phase boundary (from 5.7 MPa, 5.0 °C to 11.9 MPa, 2.8 °C). In some of these instances, droplets were seen to develop a hydrate skin only after they had come to rest under the lid of the rising tube (Figure 3.3). This indicates that significant hydrate formation did not occur before these droplets detached from the nozzle and had risen about 100 cm through the tube, even though the P -/ T -conditions were inside the hydrate stability field. In contrast, no oscillations were observed in experiments conducted at pressures higher than 14.7 MPa nor at advanced stages of the experiments. This indicates that at these conditions hydrate crystallization around droplets was significantly faster. The probability of a hydrate nucleus to reach a critical size that ensures thermodynamic stability and allows further growth is dependent on the concentration of the dissolved hydrate-forming gas species in the bulk fluid and the degree of supercooling (i.e. the distance in the P -/ T -diagram from the 3-phase boundary) (Sloan, 1998). Nucleation is considerably facilitated by

the presence of foreign bodies serving as seed crystals (e.g. microscopic dust particles) or water micro-structures which have been preserved in water that has been in contact with hydrates before (Sloan, 1998; Maini and Bishnoi, 1981). For methane bubbles released within the methane hydrate stability field in an open ocean experiment, it has been shown that already established shape oscillations were suppressed after hydrate formed at the interface, which could take several minutes from the time of release (i.e. several 10s of meters of rise) (Rehder et al., 2002). Our data clearly show that immediate formation of hydrate at the CO₂-seawater interface cannot be assumed for droplets released in undersaturated waters under P -/ T -conditions not too far from the three-phase boundary. A considerable part of the scatter in the records of droplet flatness can be attributed to droplets without a hydrate skin, allowing shape oscillations at $Re > Re_{crit}$. This is evident in Figure 3.2 by comparing the increased scatter of data from outside the hydrate stability field relative to the low scatter of the experiment farthest within the hydrate stability field, where immediate hydrate skin formation is furthermore evident from the high sphericity of the droplets throughout the entire radius range.

3.3.2 Rise velocity

All data on terminal velocities measured inside the CO₂ hydrate stability field are shown in Figure 3.4. The general trends show the expected increase in u_T with droplet radius for small radii, and a decrease of u_T with increasing simulated seawater depth. Terminal velocities increased to a radius of maximum velocity and slightly decreased with further increase of r_e . The general trend of the data sets is in accordance with the data presented by Ozaki et al. (2001). Deviations are detectable in the four data sets obtained at conditions from close to the phase boundary up to 11.9 MPa, 2.8 °C (Figures 3.4 a - d). While data points at $r_e \geq 4$ mm show a diffuse scatter, the deviations of smaller droplets appear to be systematic (Figures 3.4 a, d). The rise rates of these small sized outliers exceed those following the general trend by up to 50%. The terminal rise velocity u_T of the droplets can be derived by balancing buoyant and drag forces and reads

$$u_T = \sqrt{\frac{8gr_e(\rho_{SW} - \rho_{CO_2})}{3C_d\rho_{SW}}}, \quad (3.2)$$

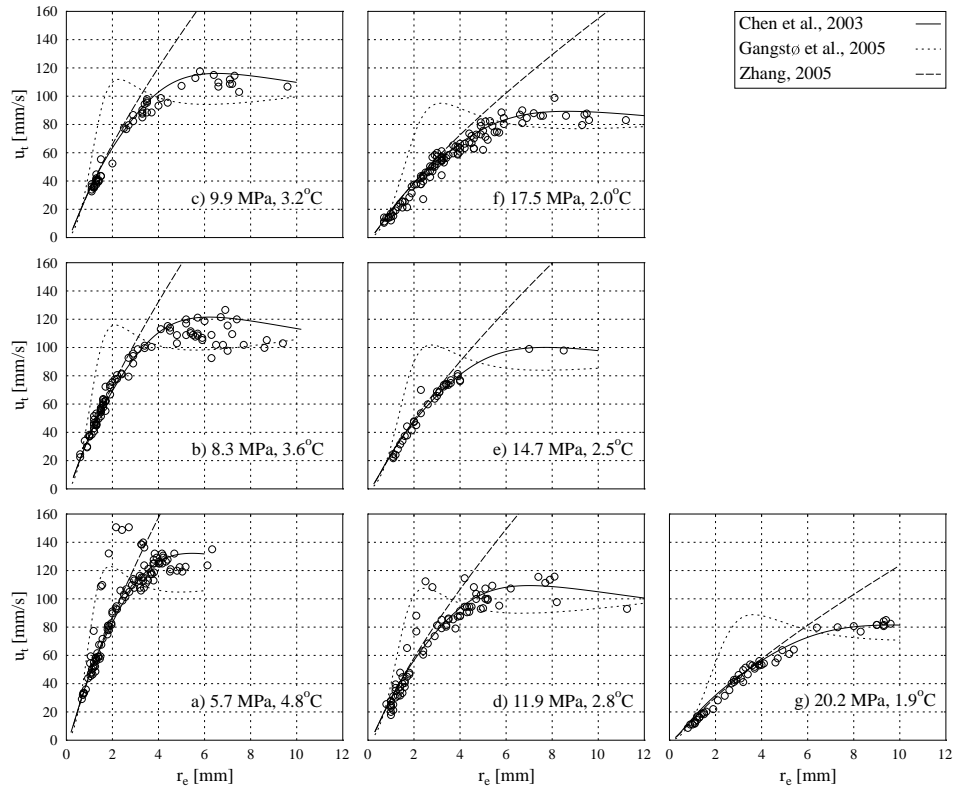


Figure 3.4: Terminal velocities of droplets rising at hydrate forming conditions. Circles represent observed velocities of individual droplets, lines denote calculated values according to drag parameterizations found in Chen et al. (2003); Gangstø et al. (2005); Zhang (2005) as indicated in the key.

where g is gravitational acceleration, r_e droplet radius, ρ_{SW} and ρ_C seawater and CO_2 density, respectively and C_d the drag coefficient. The main uncertainty is related to the prediction of C_d . For rigid, spherical and steadily moving particles, C_d can be correlated with Re using standard drag curves (Clift et al., 1978). While rise rates calculated on grounds of standard drag curves may be correct for spherical droplets with a rigid interface they will deviate from observed rise rates for flattened, oscillating droplets with a mobile interface.

Deformation effects

Droplet deformation to ellipsoidal shapes results in an increased flow resistance since the cross section perpendicular to the direction of motion increases. Effects arising from droplet deformation are evidenced by comparing our observations to the rise rates calculated according to Zhang (2005) who proposed a rigid sphere approach (Figure 3.4). While there is good agreement in the spherical size regime the limitations of the approach are clearly demonstrated by the negative deviations of observed rise rates from calculations as droplets deform to ellipsoid shapes.

Effect of surface mobility

A mobile surface significantly keeps the velocity gradient and thus friction at the interface of the fluid particle at a minimum and thus allows high rise velocities (Clift et al., 1978). A theory of the effect of hydrate skin formation on surface mobility has been proposed for methane bubbles by (McGinnis et al., 2006) and is adopted here. Hydrate that crystallizes at the surface of the droplet is swept to the south pole of the droplet and accumulates there to form a hydrate skin. As the skin grows upward along the interface, surface mobility of the droplet decreases and friction increases. Friction reaches a maximum when the entire droplet is coated by hydrate. Consequently, different parameterizations of droplet rise velocities for "clean" (i.e. mobile surface) and hydrate coated (immobile surface) droplets are required. Surface immobilization can also be caused by surface active contaminations (surfactants) in the continuous medium. Retardation of the interface mobility by surfactants is a result from tangential stress caused by local reductions of the surface tension (Clift et al., 1978; Leifer and Patro, 2002). Surface mobility can only be realized if effects arising from contaminations are negligible. While even minute contamination can have a major impact on the drag of gaseous bubbles in aqueous systems (Clift et al., 1978; Leifer and Patro, 2002), it is likely that the CO₂(l)/water system is less affected. This is due to the comparatively low surface tension reduction caused by most contaminants in liquid/liquid systems with respect to high systems such as gas/water (Clift et al., 1978).

Effects of oscillation

The effect of oscillations has been demonstrated in a number of bubble experiments in gas/liquid systems and it was shown that the onset of oscillations corresponds to a maximum in u_T and a minimum in C_d (Clift et al., 1978). For methane, it was observed that bubbles released within the methane hydrate stability field changed to a state with reduced shape oscillations and simultaneously, decreased dissolution rates. Both effects have been attributed to the formation of a hydrate skin (McGinnis et al., 2006). A hydrate skin at the CO₂ droplet surface similarly appears to prohibit oscillations by "freezing in" the shape. Given the ambiguity in the magnitude of parameters involved, several parameterizations of CO₂ droplet rise velocity are currently used in models describing the fate of CO₂ droplets rising in seawater (Chen et al., 2003; Gangstø et al., 2005; Zhang, 2005), which are contradictory in theoretical approach and partly rely on different experimental data bases (Brewer et al., 2002; Ozaki et al., 2001). Applying the velocity theories to the P -/ T -conditions of our experiments, the data of droplets with hydrate at the CO₂/water interface are in excellent agreement with the parameterization of C_d suggested by Chen et al. (2003) (Figure 3.4). Neither the approach by Gangstø et al. (2005) nor the deformation-neglecting approach Zhang (2005) are suitable to reproduce our results. The parameterization by Chen et al. (2003), shows good agreement over the entire range (P , T , r_e) of the data reported by Ozaki et al. (2001), as well as to the new data set presented here, covering the range of the hydrotherm from roughly 500 to 2000 mbsl. Thus, for droplets in the size range studied here, we strongly suggest the use of the parameterization of u_T developed by Chen et al. (2003) in models describing the rise of liquid CO₂ droplets for scenarios of mid-water CO₂ injection or leakage of CO₂ from sub-sedimentary storage into the ocean.

3.3.3 Behavior of non-hydrate coated droplets

The parameterization of Chen et al. (2003) is valid only if the interface is immobile, which apparently is the case for hydrate-coated droplets. As pointed out earlier, several data points from experiments within the hydrate stability field at pressures ≤ 11.9 MPa stray from the general trend and the parameterization by Chen et al. (2003, Figure 3.4 a - d). Negative deviations from calculated velocities could be correlated with shape oscillations. Our observations suggest that oscillations arose

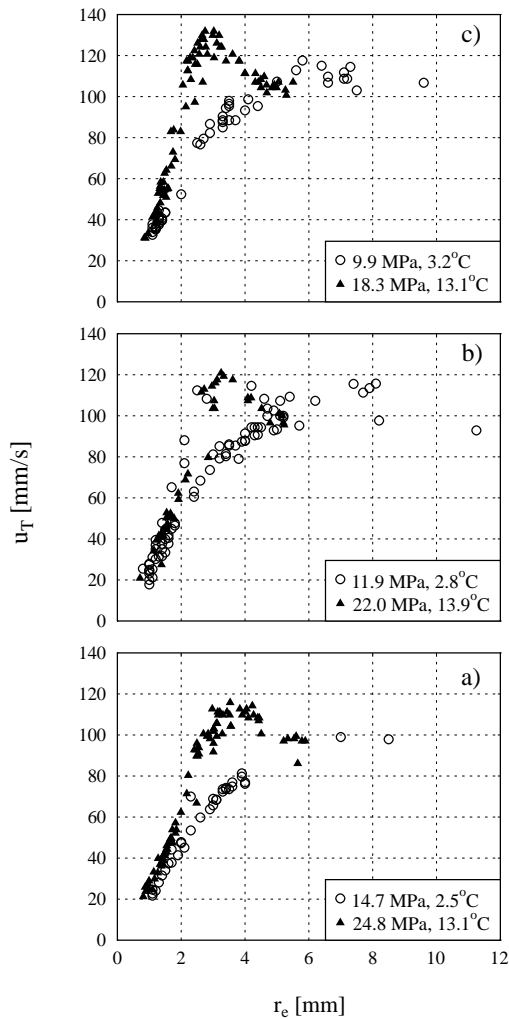


Figure 3.5: Pairs of measured droplet rise rates at P -/ T -conditions inside (circles) and outside (triangles) the field of hydrate stability. in a) 47.5 kg/m^3 , b) 62.3 kg/m^3 and c) 75.4 kg/m^3 .

from a lack of rigidifying hydrate at the CO_2 /water interface. This might have been due to hydrate nuclei having been shed from the interface at rates higher than the nucleation rate. Hydrate shedding from large CO_2 droplets has been described by Teng and Yamasaki (1999). Missing hydrate skins also seem to be the reason for higher than predicted velocities at smaller diameters. If hydrate coatings fail to develop in the non-oscillating regime, the surface mobility is left intact and droplets rise faster than their hydrate-covered counterparts. Results of our inter-comparison experiments in- and outside the hydrate stability field are shown in Figures 3.5 a - c. difference between the two sets of data for each , with small-sized droplets outside the hydrate stability field rising at higher velocities than the majority of the droplets exposed to hydrate-forming conditions. From smallest radii onward u_T quickly increased to a maximum at the onset of oscillations. Toward larger radii, velocities of droplets outside the hydrate stability field decreased and ultimately fell below values measured for droplets inside the hydrate stability field. The curve shapes of the former are typical for droplets and gas bubbles with mobile surfaces and intact internal circulation (Clift et al., 1978; Leifer and Patro, 2002). Given the similarity of execution of the experiments, these differences can only be attributed to the ability to form a hydrate skin at the interface. The data therefore not only demonstrate the impact of a hydrate skin on u_T , but also verify (a) that

the occurrence of the outliers was caused by a natural effect rather than experimental uncertainty or artifacts and (b) the successful exclusion of surface active contaminants during the measurements. The similarities of the curve shapes in Figure 3.5 a - c and the outliers in Figure 3.4 a, d strongly support our interpretation that these droplets indeed failed to develop a hydrate skin despite being exposed to hydrate forming conditions. Further evidence is shown in Figure 3.5 b, in which the outlying velocities of droplets exposed to hydrate-forming conditions plot quite well into the curve of data points gained at P -/ T -conditions prohibiting the formation of hydrate. Even though hydrate-coated droplets were observed to be the norm throughout the hydrate stability field as investigated, the observations reveal a growing uncertainty as to hydrate formation the closer pressure and temperature approach the phase boundary. Hydrate skin formation on individual droplets released into a large body of water, such as the real ocean, where background CO_2 concentrations remain low at the point of injection, should be hampered even more than in our laboratory experiments. In the limited volume of water in the experimental chamber (7.9 L), CO_2 concentrations quickly rose during the course of an experiment, though care was taken to maintain the CO_2 concentration far from saturation. Increased CO_2 concentration should decrease the average nucleation time. The situation might be different if leakage of sub-sedimentarily stored CO_2 occurs. Here, abundant seed crystals in the sediment should facilitate rapid formation of hydrate, as has been observed for the natural CO_2 vents at the NW Eifuku volcano, Mariana Arc, in 1600 m water depth (Lupton et al., 2006). With this work we were able to eliminate any uncertainty concerning the drag parameterization of hydrate covered CO_2 droplets in existing model calculations. To assess the environmental risks involved with large scale release of anthropogenic CO_2 in the deep ocean, we nevertheless recognize the need for further research in this field. Both, the effects of droplet dissolution within the field of hydrate stability and the effects of delayed hydrate crystallization have to be addressed experimentally to complement the existing data base currently in use for predicting the fate of droplets rising in oceanic waters.

Acknowledgments

This is publication no. GEOTECH-323 of the R&D Program GEOTECHNOLOGIEN funded by the German Federal Ministry of Education and Science (BMBF) and German Research Foundation (DFG), Grant 03G0600D). Furthermore, the work was supported by the European Union within the EU FP6 Integrated Project CARBOOCEAN (contract no. 511176). Special thanks go to our technical staff.

Supporting Information Available

Detailed description of the experimental set-up and its mode of operation; outline of procedure involving the optical measurement of CO₂ droplets; full data set of aspect ratios of droplets exposed to hydrate forming conditions (cf. Appendix B).

References

- Alendal, G.; Drange, H. Two-phase near-field modeling of purposefully released CO₂ in the ocean. *J. Geophys. Res.*, 106, **2001**, 1085–1096.
- Angus, S.; Armstrong, B.; de Reuck, K. M. *International thermodynamic tables of the fluid state*. Pergamon Press **1976**.
- Bozzano, G.; Dente, M. Shape and terminal velocity of single bubble motion: A novel approach. *Comput. Chem. Eng.*, 25, **2001**, 571–576.
- Brewer, P. G.; Chen, B.; Warzinski, R.; Baggeroer, A.; Peltzer, E. T.; Dunk, R. M.; Walz, P. Three dimensional acoustic monitoring and modeling of a deep-sea CO₂ droplet cloud. *Geophys. Res. Lett.*, 33, **2006**, L23607.
- Brewer, P. G.; Peltzer, E. T.; Friederich, G.; Rehder, G. Experimental determination of the fate of rising CO₂ droplets in sea water. *Environ. Sci. Technol.*, 36, **2002**, 5441–5446.
- Chen, B.; Song, Y.; Nishio, M.; Akai, M. Large-eddy simulation of double cloud formation induced by CO₂ dissolution in the ocean. *Tellus*, 55, **2003**, 723–730.

- Clift, R.; Grace, J.; Weber, M. *Bubbles, Drops, and Particles*. Academic Press, New York **1978**.
- Gangstø, R.; Haugan, P. M.; Alendal, G. Parameterization of drag and dissolution of rising CO₂ drops in seawater. *Geophys. Res. Lett.*, **32**, **2005**, L10612, doi:10.1029/2005GL022637.
- Hirai, S.; Okazaki, K.; Tabe, Y.; Hijikata, K.; Mori, Y. Dissolution rate of liquid CO₂ in pressurized water flows and the effect of clathrate films. *Energy*, **22**, **1997**, 285–293.
- Holder, G. D.; Cugini, A. V.; Warzinski, R. Modeling clathrate hydrate formation during carbon dioxide injection into the ocean. *Environ. Sci. Technol.*, **28**, **1995**, 276–278.
- IPCC, . *IPCC Special Report on Carbon Dioxide Capture and Storage*. Cambridge University Press, Cambridge, New York **2005**.
- Leifer, I.; Patro, R. K. The bubble mechanism for methane transport from the shallow seabed to the surface: A review and sensitivity study. *Cont. Shelf Res.*, **22**, **2002**, 2409–2428.
- Lupton, J.; Butterfield, D.; Lilley, M.; Evans, L.; Nakamura, K.; Chadwick, W.; Resing, J.; Embley, R.; Olson, E.; Proskurowski, G.; Baker, E.; de Ronde, C.; Roe, K.; Greene, R.; Lebon, G.; Young, C. Submarine venting of liquid carbon dioxide on a Mariana Arc volcano. *Geochem. Geophys. Geosyst.*, **7**.
- Maini, B. M.; Bishnoi, P. R. Experimental investigation of hydrate formation behaviour of a natural gas bubble in a simulated deep sea environment. *Chem. Eng. Sci.*, **36**, **1981**, 183–189.
- McGinnis, D. F.; Greinert, J.; Artemov, Y.; Beaubien, S. E.; Wüest, A. Fate of rising methane bubbles in stratified waters: How much methane reaches the atmosphere? *J. Geophys. Res.*, **111**, **2006**, C09007, doi:10.1029/2005JC003183.
- Ohmura, R.; Mori, Y. H. Critical conditions for CO₂ hydrate films to rest on submarine CO₂ pond surfaces: A mechanistic study. *Environ. Sci. Technol.*, **32**, **1998**, 1120–1127.

- Ozaki, M.; Minamiura, J.; Kitajima, Y.; Mizokami, S.; Takeuchi, K.; Hatakenaka, K. CO₂ sequestration by moving ships. *J. Mar. Sci. Technol.*, 6, **2001**, 51–58.
- Radhakrishnan, R.; Demurov, A.; Herzog, H.; Trout, B. L. A consistent and verifiable macroscopic model for the dissolution of liquid CO₂ in water under hydrate forming conditions. *Energy Convers. Manage.*, 44, **2003**, 771–780.
- Rehder, G.; Brewer, P.; Peltzer, E. T.; Friederich, G. Enhanced lifetime of methane bubble streams within the deep ocean. *Geophys. Res. Lett.*, 29, **2002**, 1731, doi: 10.1029/2001GL013966.
- Rehder, G.; Steffen, H.; Gust, G. Towards investigation of CO₂ phase transition processes using advanced pressure lab technology. In *UNESCO/SCOR International Science Symposium*. Paris **2004**.
- Schlitzer, R. Ocean Data View **2007**.
- Siedler, G.; Peters, H. Properties of seawater, physical properties (general). In Sündermann, J. (ed.), *Landolt-Börnstein Oceanography; New Series V/3a*, vol. New Series V/3a. Springer-Verlag, Berlin **1986**, 233–264.
- Sloan, E. D. J. *Clathrate Hydrates of Natural Gases*. Marcel Dekker, Inc., New York, New York, 2nd ed. **1998**.
- Teng, H.; Yamasaki, A. Hydrate formation on surfaces of buoyant liquid CO₂ drops in a counterflow water tunnel. *Energy Fuels*, 13, **1999**, 624–628.
- Zhang, Y. Fate of rising CO₂ droplets in seawater. *Environ. Sci. Technol.*, 39, **2005**, 7719–7724.

4 Terminal velocities of pure and hydrate coated CO₂ droplets and CH₄ bubbles rising in a simulated oceanic environment

Nikolaus K. Bigalke^{*1}, Lars Inge Enstad², Guttorm Alendal², Gregor Rehder³

Leibniz Institute of Marine Sciences at the University of Kiel, Wischhofstr. 1-3,
24114 Kiel, Germany

nbigalke@ifm-geomar.de

Abstract

Understanding the upward motion of CO₂ droplets or CH₄ bubbles in oceanic waters is prerequisite to predicting the vertical distribution of the two most important greenhouse gasses in the water column. A key parameter governing the fate of droplets or bubbles dissolving into the surrounding seawater as they rise is the terminal velocity. The latter is strongly influenced by the ability of both compounds to form skins of gas clathrate, if pressure and temperature satisfy thermodynamic framework conditions. Experimental efforts aiming to elucidate the rise properties of CO₂ droplets and CH₄ bubbles and specifically the influence of clathrate skins open the possibility to obtain a parameterization of the terminal velocity applicable to both clathrate coated and pure fluid particles of CH₄ and CO₂. With the present study, we report on experimentally determined terminal velocities of single CH₄ bubbles released to pressurized and thermostatted seawater. Clathrate skins were identified by high bubble sphericities and changed motion characteristics. Based on

¹phone: +49 431 600-1410, fax:+49 431 600-1400

²Bergen Center for Computational Science, UNIFOB AS, Allegaten 70, N-5007 Bergen, Norway

³Leibniz Institute for Baltic Sea Research at the University of Rostock, Seestr. 15, 18119 Rostock, Germany

these experiments as well as published data on the rise of hydrate coated and pure liquid CO₂ droplets and physical principles previously successfully used for clean bubbles, a new parameterization of the terminal velocity is proposed. Comparison of the experimental data with model predictions is satisfactory in case of CH₄ and excellent in case of CO₂.

4.1 Introduction

Understanding bubble and droplet motion in oceanic waters is a prerequisite to quantify the net flux of greenhouse gases from marine sediments into the atmosphere. Methane (CH₄) is probably the most significant species in this respect since marine sediments naturally hold vast quantities of CH₄ in ice-like compounds known as gas clathrates or gas hydrates (Kvenvolden, 1998; Buffett and Archer, 2004; Milkov, 2004). Gas hydrates are not stable at elevated temperatures; hence, CH₄ at greater sediment depths takes the state of a free gas. This latter reservoir is estimated to be of similar magnitude as that of the gas hydrates (Buffett and Archer, 2004). The absorption of infrared radiation by CH₄ is by far more effective as that of carbon dioxide (CO₂) (26 × on a mole-per mole basis and in the current atmosphere; Lelieveld and Crutzen, 1998); therefore, the destabilization of gas hydrate deposits by rising seawater temperatures and large-scale release of CH₄ to ocean and atmosphere could potentially cause a rapid rise of global temperatures. Discharge of CH₄ due to gas hydrate destabilization could occur for example by slumping of continental slopes and release of large amounts of the trapped gas below (Paull et al., 2003). Rapid decomposition of large amounts of gas hydrates and subsequent release of CH₄ to ocean and atmosphere are held responsible for repeated negative δ¹³C-anomalies in the geological record of the Phanerozoic (Dickens et al., 1995; Hesselbo et al., 2000; Kennett et al., 2000) and indicate periods of a rapid climate change.

Interest in studying the rise properties of CO₂ droplets has initially been fueled by suggestions to disperse liquid CO₂ in the open ocean as a means to mitigate adverse climate effects arising from the industrial combustion of fossil fuels. Due to ecological concerns, direct ocean storage is

becoming increasingly unpopular and considerable efforts are currently being made to internationally ban this type of sequestration. With respect to scenarios involving the storage in terrestrial geologic formations the marine environment nevertheless offers several advantages. Because of the negative thermal gradient in oceanic waters, the temperature at depth is usually lower than the critical temperature of CO_2 . Under general oceanic conditions CO_2 transforms into the liquid state at depths between 400 and 500 mbsl. The high compressibility of liquid CO_2 compared to seawater leads to a density ratio inversion at water depths between 2500 and 3000 mbsl, depending on ambient temperature. In saturated

water and at favorable P -/ T -conditions CO_2 crystallizes into the sI hydrate structure and is thus structurally isotypical with CH_4 hydrate (Sloan and Koh, 2008). The phase diagram in Figure 4.1 shows that, depending on the local hydrothermal gradient, P and T allow hydrate formation at depths >500 mbsl in the case of CH_4 and >400 mbsl in the case of CO_2 . A recent suggestion of storing anthropogenic CO_2 in deep marine sediments combines the advantages of a geological storage with favorable thermodynamic framework conditions (House et al., 2006). Sub-sea storage in geological formations is explicitly tolerated in the 2006 Amendment of the 1996 Protocol of the London Convention (IMO, 2006) provided it is intended for permanent storage and a risk analysis has been made with adequate remediation plans. A proper risk analysis includes an environmental impact assessment following potential leakage and propagation of liquid CO_2 to marine waters.

Since seawater is generally strongly under-saturated in both CH_4 and CO_2 , bubbles and droplets (“particles” in the following) of the respective compounds dissolve during their ascent in the water column. The distance individual particles travel

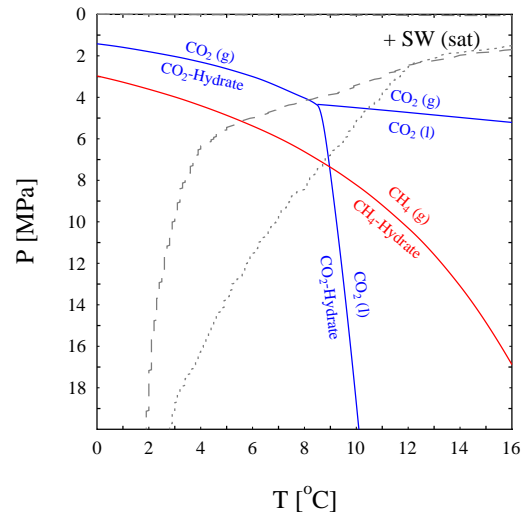


Figure 4.1: Phase diagram of seawater and excess quantities of CH_4 (red lines) and carbon dioxide (blue lines). 1 MPa hydrostatic pressure corresponds to a water column of approximately 100 m height. Dashed and dotted lines denote two exemplary P -/ T -profiles from localities in the Pacific (35°N , 142°E) and Indian (5°N , 77°E) Ocean, respectively (Schlitzer, 2007). Phase boundaries calculated after Sun and Duan (2005).

depends on dissolution speed, particle size and rise velocity. The properties are interrelated and further modified if hydrate crystallizes at the particle interface. While the change of the dissolution speed following hydrate skin formation has been observed for example in deep-sea experiments by Brewer et al. (2002) and Rehder et al. (2002) the influence of hydrate skins on the rise velocity could be highlighted in tank experiments by Bigalke et al. (2008).

A large number of model calculations (Sato et al., 2000; Chen et al., 2003; Alendal and Drange, 2001; Zhang, 2005; Gangstø et al., 2005; McGinnis et al., 2006; Leifer and Patro, 2002; Zhang, 2003), laboratory (Hirai et al., 1996; Ozaki et al., 2001; Haljasmaa et al., 2005; Maini and Bishnoi, 1981) and ocean (Brewer et al., 2002; Tsouris et al., 2004; Brewer et al., 2006; Rehder et al., 2002) experiments have been performed to assess the fate of the particles rising in the water column. The experiments are complemented by mostly hydro-acoustic investigations at natural CH₄ bubble seep sites, which have been identified at various depths and locations worldwide (Judd, 2003). In contrast to CH₄ bubble seepage, natural venting of liquid CO₂ is a rare phenomenon associated with seafloor hydrothermal systems (Sakai et al., 1990; Lupton et al., 2006; Shitashima et al., 2008). Despite the wealth of information published on the matter, until recently, predictions of the lifetimes of CO₂ droplets or CH₄ bubbles had to rely on simplifying assumptions and empirical approximations concerning both rise velocity and dissolution kinetics. This is essentially due to the unavailability of detailed experimental observations on the nature of the hydrate skin.

As a first step in predicting the lifetime of CH₄ bubbles or CO₂ droplets in oceanic waters, this work presents a numerical model describing the terminal velocities of particles rising at hydrate forming conditions. A recently published compilation of rise velocities of CO₂ droplets (Bigalke et al., 2008) and previously unpublished data on the rise rates of CH₄ bubble serves as data base for the model. The data reported in (Bigalke et al., 2008) confirm a parameterization by Chen et al. (2003) who included empirical equations in their model to estimate terminal rise velocities. The model presented here is derived from physical principles. It is a function of non-dimensional numbers thought to affect the shape and friction of particles. It has the advantage of being at least universal enough to be applicable to hydrate coated CH₄ bubbles and CO₂ droplets using the same formula framework.

4.2 Experimental

The experiments were conducted in a stainless steel tank (1.3 m \times 0.3 m inner height and diameter) rated to a maximum pressure of 55 MPa and capable of maintaining a homogeneous minimum temperature of 1 °C inside. The vessel was filled with tap water to convey the selected pressure and temperature to the experimental apparatus inside. Central part of the latter was a seawater-filled (S=35) Plexiglas tube of 100 mm diameter and 1000 mm length. Droplets and bubbles were generated individually at a nozzle fixed in the bottom of the tube. CO₂(*l*) or CH₄(*g*) were provided from a pressurized supply connected to the bottom of the tube. Three cameras, two internal, one external, were read out synchronously to record shape, size and velocity of each droplet or bubble rising in the stagnant seawater inside the tube. Details of the experimental set-up, method and data analysis are given in Bigalke et al. (2008) and associated auxiliary information.

4.2.1 CO₂ droplets

The CO₂ droplet data reported in (Bigalke et al., 2008) were obtained at *P*-/*T*-conditions both within and outside the hydrate stability field (HSF). Inside the HSF experiments were carried out at seven different pressures and temperatures along a simulated oceanic hydrotherm. The majority of the droplets rising along the hydrotherm were found to be coated with a hydrate skin. Exceptions were identified at conditions closest to hydrate dissociation. These pure liquid droplets were found to rise at the same velocities as equally buoyant droplets outside the HSF and up to 50% faster than their equally buoyant hydrate-coated counterparts. Hence, close to the hydrate phase boundary, delayed hydrate formation around the droplets and consequently, changed rising dynamics must be taken into consideration when estimating the fate of droplets rising in oceanic waters.

4.2.2 CH₄ bubbles

Rather than simulating *P*-/*T*-conditions along a natural hydrotherm CH₄ bubbles were generated at 4 and 14 °C and at discrete pressures ranging from 60 to 400 bar. Start and end of each experimental run were at the low and high pressure limits, respectively. The seawater was not exchanged during an experimental run. While the

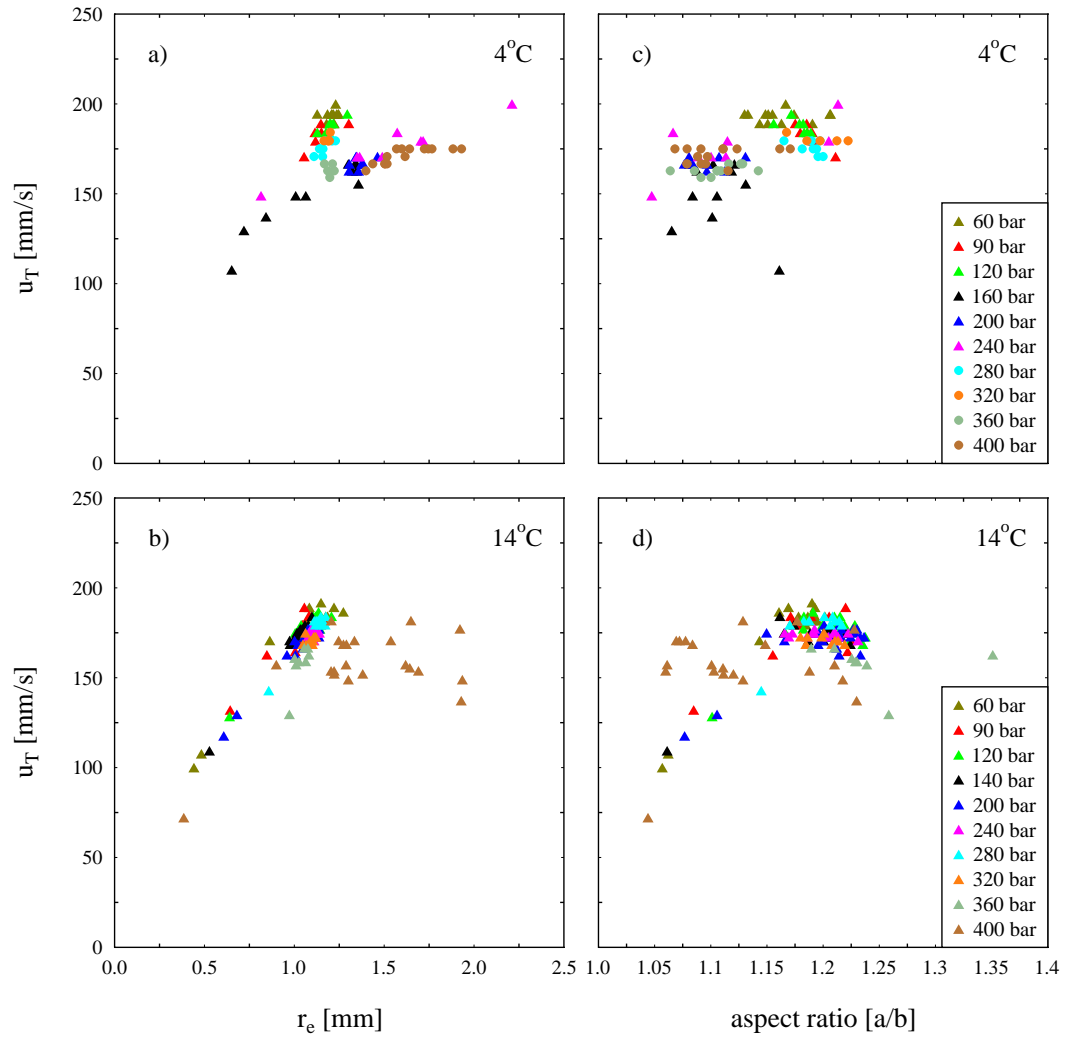


Figure 4.2: Terminal rise velocities plotted against equivalent bubble radii (a, b) and ratios of major (a) and minor (b) bubble semi axes (c, d)). The sphericity of a bubble increases with $a/b \rightarrow 1$. At 4 °C data was obtained in two experimental runs identifiable by triangles (1st) and circles (2nd run).

data at 14 °C was gained in one experimental run, the experiment at 4 °C consisted of two runs with a de-pressurization to atmospheric pressure and an exchange of the water between the 240 and 280 bar data sets. According to the procedure by Tishchenko et al. (2005), the dissociation pressures (P_{diss}) for CH₄ hydrate at 4 and 14 °C is 44 and 136 bar, respectively. Therefore, hydrate could not have formed at the three lowest pressures of the 14 °C experiment. Experimental results are shown

in Figure 4.2. In diagrams a) and b), the terminal velocities, u_T , are plotted against the equivalent radii, r_e for the two experimental temperatures. r_e is defined by $\sqrt[3]{a^2b}$, where a and b are major and minor semi axes of the imaged bubbles, respectively. Due to the narrow nozzle orifice of 0.5 mm diameter, the majority of the bubbles fell into the rather narrow r_e -range of 1-2 mm. The choice of orifice diameters was restricted to 0.5 mm or less, since wider diameters allowed water to enter the tubing connecting internal gas supply and rising tube. CH₄ hydrate subsequently forming inside the tubing frequently clogged the pathway for the gas, requiring either de-pressurization below P_{diss} or breaking off the experimental run. In the size range shown in Figure 4.2, no significant dependence of the velocity on the CH₄ density (which at constant temperature is a function of pressure only) can be observed. The dependence of the velocity on the radius is more conspicuous. Here, two trends can be observed: at both temperatures the dependence of velocity on radius is much more sensitive at early stages of the experimental runs than at later stages. In the experiment at 4 °C for example, data gained between 60 and 120 bar follows a distinctly steeper trend than the data gained between 160 and 240 bar. This bimodal behavior is also observable in the second run of this experiment, between the 280-320 and the 360-400 bar data sets. In the 14 °C a similar although less defined behavior is visible between the 60-360 and 400 bar data sets. The comparison of equally sized bubbles within an experimental run reveals high sphericities at final and lower sphericities at early stages (Figure 4.2). This observation is most apparent by comparison of the 280 and 360 bar data sets of the 4 °C experiment. At 14 °C the jump in sphericity occurs within the 400 bar data set. In conclusion, bubbles with higher sphericity appear to rise at lower velocities than equally sized but more deformed bubbles.

4.3 Mathematical Approach

The steady state or terminal velocity u_T of a spheroid dispersed in a continuous medium is determined by the balance of buoyant and friction forces. Thus u_T is given by

$$u_T = \sqrt{\frac{8gr_e(\rho_{\text{SW}} - \rho_{\text{P}})}{3C_d\rho_{\text{SW}}}}. \quad (4.1)$$

While gravitational acceleration (g), densities of continuous (ρ_{SW}) and dispersed (ρ_{P}) phases are easily accessible variables of Equation 4.1, the drag coefficient (C_{d}) of hydrate coated bubbles and droplets is essentially unknown. The mathematical deduction of the obtained drag parameterization for hydrate coated bubbles and droplets as well as lean droplets used in the present treatment follows the same procedure used by Bozzano and Dente (2001). The latter found a drag parameterization of bubbles rising in a variety of liquids at atmospheric pressures. Accordingly, C_{d} is given by

$$C_{\text{d}} = f \left(\frac{a}{r_{\text{e}}} \right)^2 = f \text{DEF}, \quad (4.2)$$

where f is the friction factor of the hydrate coated spheroid and DEF its deformation factor. The mathematical approach to find DEF builds on two main assumptions. The first states that the hydrate coated particle attains a shape that minimizes its energy. The second uses the approximated generalization of C_{d} . In accordance to experimental observations summarized in Clift et al. (1978), the shape of dispersed spheroids can be approximated by combining two semi-spheroids of different heights at their identical base areas. The upper minor semi axis of the obtained object is equal to b_1 , the lower equal to b_2 . Here, $b_1 \geq b_2$. The major semi axis is given as a . The total energy, E_{ttl} , of the spheroid is given by

$$E_{\text{ttl}} = E_{\text{pot}} + E_{\text{sup}} + E_{\text{kin}}, \quad (4.3)$$

where the potential energy E_{pot} is

$$E_{\text{pot}} = (\rho_{\text{SW}} - \rho_{\text{P}})gV_{\text{B}}(3b_1 + 5b_2)/8. \quad (4.4)$$

Here, V_{B} is the volume of the particle defined by $\frac{2}{3}\pi a^2(b_1 + b_2)$. The surface energy E_{sfc} is given by

$$E_{\text{sfc}} = \sigma \left(2\pi a^2 + \frac{1}{2}\pi \frac{b_1^2}{e_1} \ln \left(\frac{1+e_1}{1-e_1} \right) + \frac{1}{2}\pi \frac{b_2^2}{e_2} \ln \left(\frac{1+e_2}{1-e_2} \right) \right), \quad (4.5)$$

with σ denoting the interfacial tension and e_1 and e_2 the eccentricities of the two semi-spheroids defined by $e = \sqrt{1 - b^2/a^2}$. The kinetic energy E_{kin} is given as

$$E_{\text{kin}} = \frac{2}{3}\pi\rho_L a^3 u_T^2. \quad (4.6)$$

In accordance to Bozzano and Dente (2001), the first step toward minimizing E_{ttl} (Equation 4.3) is to express the total energy as a function of the two non-dimensional parameters $x = b_1/r_e$ and $y = b_2/r_e$. In this process, the definitions of the dimensionless Eötvös, $\text{Eo} = (\rho_{\text{SW}} - \rho_{\text{P}})gr_e^2\sigma^{-1}$, and Morton, $\text{Mo} = g\mu_{\text{SW}}^4(\rho_{\text{SW}} - \rho_{\text{L}})\rho_{\text{P}}^{-2}\sigma^{-3}$, numbers emerge, in which μ_{SW} denotes the dynamic viscosity of the continuous phase. To estimate Eo and Mo of hydrate coated particles, a physical analogue to the interfacial tension has to be found. If we treat the hydrate layer as a mathematically infinitesimal layer and look at the energy/area ratio of this layer in a macroscopic perspective, it should be appropriate to regard this as an interfacial tension. By investigating waves on a hydrate covered pool of CO_2 in the deep ocean (Brewer et al., 2005), Hove and Haugan (2005) derived an analogous interfacial tension of 0.075 N m^{-1} for CO_2 hydrate. This value is used in the subsequent development of the drag parameterization. The minimization of E_{ttl} is done by numerically solving the derivatives of Equations 4.4-4.6 for a range of Eo and Mo numbers sufficiently wide to cover the shape regimes of bubbles and droplets encountered in the experiments (Table 4.1). E_{ttl} is a function of x and y and its minimum is a single point in each computation. DEF is defined as $2/(x + y)$ (Bozzano and Dente, 2001), so to find DEF as a function of Eo, both coordinates (x, y) giving minimum energy are individually represented in terms of Eo and Mo. In this manner, the energetically most favourable DEF can be found as a function of Eo for the ranges of Eo and Mo given in Table 4.1. The deformation factor obtained by this method is

$$\text{DEF} = \left(\frac{a}{R_0}\right)^2 = \frac{2}{x + y} \approx \frac{2}{1.4903 + 0.019(\text{Eo} - 0.6)^2 - 0.143\text{Eo}^{8.25/7}}. \quad (4.7)$$

The friction factor is deduced by studying the bubble motion at low and high Reynolds numbers. For example, the friction factor for fluid particles without a hydrate skin was found to approximate $48/\text{Re}$ at low Re numbers and 0.9 at high Re. Other constants in the equation are adjusted to fit the trend of the experimental data. Thus, the friction factor for particles without a hydrate skin is

Compound	Hydrate skin	Pressure [MPa]	Temperature [°C]	Mo	Eo	
					min	max
CO ₂	Yes	8.3	3.6	1.5×10^{-11}	0.012	1.2
CO ₂	Yes	9.9	3.2	1.3×10^{-11}	0.0099	0.99
CO ₂	Yes	11.9	2.8	1.1×10^{-11}	0.0082	0.82
CO ₂	Yes	14.7	2.5	9.0×10^{-12}	0.0062	0.62
CO ₂	Yes	17.5	2.0	6.7×10^{-12}	0.0044	0.44
CO ₂	Yes	20.2	1.9	4.6×10^{-12}	0.0030	0.30
CO ₂	No	18.3	13.1	1.5×10^{-10}	0.032	3.2
CO ₂	No	22.0	13.9	1.1×10^{-10}	0.026	2.6
CO ₂	No	24.8	13.1	9.2×10^{-11}	0.020	2.0
CH ₄	Yes	16.0	4.0	1.4×10^{-10}	0.030	0.47
CH ₄	Yes	24.0	4.0	1.3×10^{-10}	0.027	0.44
CH ₄	Yes	40.0	4.0	1.1×10^{-10}	0.024	0.39
CH ₄	Yes	40.0	14.0	3.7×10^{-11}	0.025	0.39

Table 4.1: Eo and Mo of fluid particles used as data base in the present drag parameterization. Eo numbers are given for a minimum and maximum r_e of 1 and 10 mm, respectively in case of CO₂ droplets and 0.5 and 2.0 mm in case of CH₄ bubbles.

$$f = \frac{48}{\text{Re}} + 0.9 \frac{\text{Eo}^2 + 0.07}{\text{Eo}^2 + 1}. \quad (4.8)$$

When particles are coated with hydrate, the boundary condition at the interface is different from that of clean particles, i.e. the boundary condition changes from free slip to no slip. The friction factor obtained for this case reads:

$$f = \frac{12}{\sqrt{\text{Re}}} + 0.9 \frac{\text{Eo}^2 + 0.03}{\text{Eo}^2 + 0.35}. \quad (4.9)$$

The drag coefficient of hydrate coated CO₂ droplets or CH₄ bubbles can now be calculated by substituting f and DEF in Equation 4.2 for Equations 4.9 and 4.7, respectively. Substituting C_d in Equation 4.1 for the previously generated expression yields an explicit function to calculate the terminal rise velocity of hydrate coated CO₂ droplets or CH₄ bubbles. Calculation of u_T for pure liquid CO₂ droplets involves using Equation 4.8 instead of 4.9 but is analogous otherwise.

4.4 Discussion

4.4.1 CH₄ Bubble Data

In accordance to observations by Bigalke et al. (2008) a flattening of the velocity trends can be explained by the formation of hydrate skins around the bubbles. Thus, the observed change in the velocity/radius relationship during each experimental run indicates a change of hydrodynamic boundary conditions caused by the formation of hydrate skins around the bubbles. The decrease of rise rates due to hydrate formation around the bubbles in the experiments described here is strongly supported by the coinciding shift of bubble shapes from lower to higher sphericity (Figure 4.2). The shift of shapes to higher sphericities due to hydrate skin formation is a recognized tool to discriminate between particles with and without a hydrate skin (Brewer et al., 2002; Rehder et al., 2002). The effect of a (lacking) hydrate skin on sphericity and rise velocity is specifically highlighted in the 4 °C experiment, by comparison of the 280 and 320 bar data sets with the data gained at 200 bar. Bubbles rose faster at the higher pressures even though CH₄ is considerably denser and bubbles were larger than at 200 bar. Given the higher sphericities observed in the 200 bar data set the observed reduction in rise velocity can only be attributed to changed boundary conditions due to a formation of hydrate skins around the bubbles. At 4 °C hydrate skins first appeared at 160 bar in the first and at 360 bar in the second experimental run. Hydrate formation therefore required an overpressure of 116 and 316 bar, respectively. Likewise, for the 14 °C experiment the required overpressure calculates to 264 bar. The inferred hydrate formation preferentially occurred at the end of the experimental runs, since due to dissolution of previously ascending bubbles, CH₄ concentrations in the seawater were much higher at these stages than at the beginnings of each run. Apart from considerable over-pressures, high background concentrations of CH₄ were obviously needed to initiate the formation of hydrate skins around the CH₄ bubbles. The great difference between the required over-pressures in the 4 °C data set illustrates the significance of the concentration of dissolved CH₄ in the seawater on the formation of stable hydrate nuclei, in accordance with observations by Maini and Bishnoi (1981).

The decrease in velocity due to development of a hydrate skin is in contrast to observations by Rehder et al. (2002), who did not notice reduced velocities in bubbles rising in a natural ocean environment after a sudden shift toward lower dissolution

rates clearly indicated crystallization of hydrate at the interface of the bubbles. CH₄ concentrations in oceanic waters far from geological sources are very low, in the order of 1 nmol L⁻¹ (Rehder et al., 1999). Thus, in contrast to the limited volume of seawater in our experiments (7.9 L; Bigalke et al., 2008), where the CH₄ concentration rapidly increased with progressing experimental time, hydrate crystallization in the ocean is considerably delayed. Constant rise velocities yet changed dissolution kinetics therefore suggest that in the ocean experiment formation of hydrate skins was restricted to the downstream side of the bubbles, covering an area small enough to leave the hydrodynamic boundary conditions and thus the drag largely unchanged.

4.4.2 Data Simulations

Figure 4.3 shows the comparison of the rise velocity for hydrate coated CO₂ droplets (blue symbols) together with the rise velocity computed according to the new drag parameterization (blue lines). There is good agreement between model and experiments, especially at greater simulated seawater depths. At lower pressures and larger r_e , predicted u_T fall into the lower range of observed velocities (Figure 4.3 a-c)). This could be due to the fact that droplets were not entirely coated with hydrate due to lower thermodynamic forcing and longer induction times for hydrate crystallization. Thus, a considerable part of the surface of these droplets remained mobile. As reasoned above, the boundary condition in this case leans toward a free-slip case allowing higher rise velocities than predicted by the presented theory. This interpretation agrees well with observations by Bigalke et al. (2008), who observed delayed hydrate formation around a rising population of pure liquid droplets (i.e. droplets without a hydrate skin), the closer P -/ T -coordinates were to dissociation conditions.

In Figure 4.3 b-d) data for clean CO₂ droplets are displayed (red symbols and lines). There is a favorable agreement between the drag parameterization presented in Equations 4.7 and 4.8 and the experimental data performed outside the hydrate stability field. The main difference between this case and the two others are the free slip condition at the interfacial boundary in absence of hydrate.

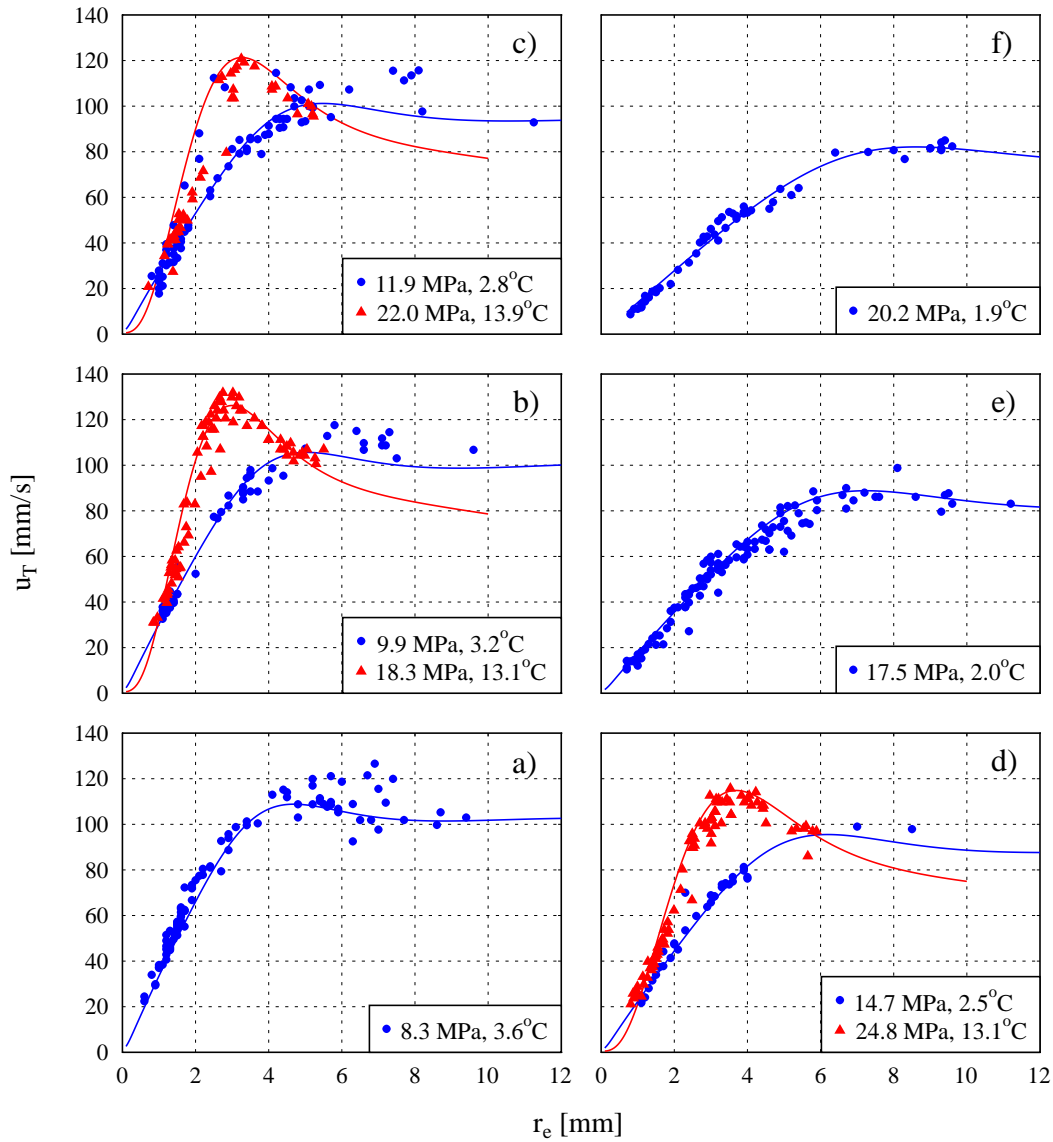


Figure 4.3: Comparison of parameterized and observed rise velocities of hydrate coated (blue) and pure liquid (red) CO₂ droplets as a function of the equivalent radius. Buoyancies of droplets at P -/ T -pairs given in the keys of diagrams b)-d) are identical.

The correspondence between hydrate coated CH₄ bubbles and the new drag parameterization is displayed in Figure 4.4. The experiments are conducted for a smaller range of r_e than in the CO₂ case, but experiments have been performed at a broad range of pressure conditions. Although most of the experiments were

performed inside the hydrate stability field, the evaluation of the aspect ratio (Figure 4.2) shows that hydrate did not form in all cases. Figure 4.4 illustrates the good agreement between experimentally and computationally obtained rise velocities for hydrate coated CH_4 bubbles. Using the fixed value of 0.075 N m^{-1} as interfacial tension of hydrate coated CH_4 bubbles (and CO_2 droplets) does not seem to affect the agreement of predicted and observed velocities. This indicates, that the surface tension of a seawater/hydrate interface does not vary much in the P and T ranges considered here and furthermore underlines the similar mechanical properties of CH_4 and CO_2 hydrates.

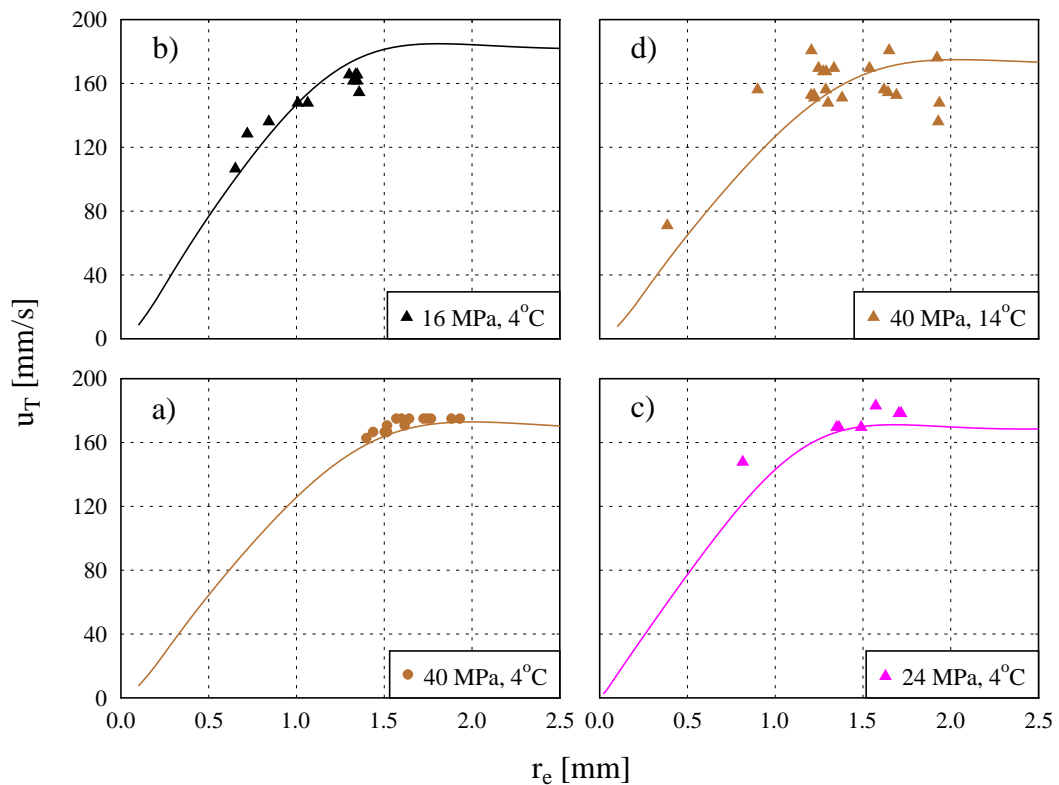


Figure 4.4: Comparison of parameterized and observed rise velocities of hydrate coated CH_4 bubbles. Color coding identical to Figure 4.2

4.5 Summary

Based on the approach by Bozzano and Dente (2001), a new model to predict the drag coefficient of CO₂ droplets and CH₄ bubbles rising in pressurized seawater is presented. The theory is a combination of two factors characterizing friction and shape as functions of the dimensionless Morton and Eötvös numbers to provide a universal parameterization of the terminal velocity of CH₄ bubbles and CO₂ droplets rising in the ocean. By including an analogon for the surface tension of a hydrate-seawater interface, the model specifically accounts for shifting hydrodynamics following crystallization of hydrate skins around CO₂ droplets and CH₄ bubbles. Terminal velocities computed based on the parameterization are evaluated by comparison with rise velocities of CO₂ droplets and CH₄ bubbles gained in tank experiments. The experiments clearly prove a previously unnoticed difference in rise velocities of hydrate coated and hydrate free CH₄ bubbles, which has similarly been observed for CO₂ droplets (Bigalke et al., 2008). A comparison of the experimental data with model predictions shows a good agreement for various pressure and temperature conditions. The good match furthermore demonstrates the feasibility of using the fixed value of 0.075 N m⁻¹ as the interfacial tension of hydrate covered CO₂ droplets *and* CH₄ bubbles dispersed in oceanic waters at depths of 4000 mbsl at least.

The ability to predict the rise history of the two most important greenhouse gasses discharged to oceanic waters within their respective hydrate stability fields is important for assessing their relevance to past and future climate change. Further efforts should aim at implementing the present parameterization into propagation models simultaneously treating CH₄ bubble or CO₂ droplet dissolution within their respective hydrate stability fields.

Acknowledgments

We thank Andreas Meyer for his skillful technical support during the experimental work. Funding was provided by the German Federal Ministry of Education and Science (BMBF) and German Research Foundation (DFG) (Grant 03G0600D).

References

- Alendal, G.; Drange, H. Two-phase near-field modeling of purposefully released CO₂ in the ocean. *J. Geophys. Res.*, *106*, **2001**, 1085–1096.
- Bigalke, N. K.; Rehder, G.; Gust, G. Experimental investigation of the rising behavior of CO₂ droplets in seawater under hydrate forming conditions. *Environ. Sci. Technol.*, *42*, **2008**, 5241–5246.
- Bozzano, G.; Dente, M. Shape and terminal velocity of single bubble motion: A novel approach. *Comput. Chem. Eng.*, *25*, **2001**, 571–576.
- Brewer, P. G.; Chen, B.; Warzinski, R.; Baggeroer, A.; Peltzer, E. T.; Dunk, R. M.; Walz, P. Three dimensional acoustic monitoring and modeling of a deep-sea CO₂ droplet cloud. *Geophys. Res. Lett.*, *33*, **2006**, L23607.
- Brewer, P. G.; Peltzer, E. T.; Friederich, G.; Rehder, G. Experimental determination of the fate of rising CO₂ droplets in sea water. *Environ. Sci. Technol.*, *36*, **2002**, 5441–5446.
- Brewer, P. G.; Peltzer, E. T.; Walz, P.; Aya, I.; Yamane, K.; Kojima, R.; Nakajima, Y.; Nakayama, N.; Haugan, P.; Johannessen, T. Deep ocean experiments with fossil fuel carbon dioxide: creation and sensing of a controlled plume at 4 km depth. *J. Mar. Res.*, *63*, **2005**, 9–33.
- Buffett, B.; Archer, D. Global inventory of methane clathrate: sensitivity to changes in the deep ocean. *Earth Planet. Sci. Lett.*, *227*, **2004**, 185–199.
- Chen, B.; Song, Y.; Nishio, M.; Akai, M. Large-eddy simulation of double cloud formation induced by CO₂ dissolution in the ocean. *Tellus*, *55*, **2003**, 723–730.
- Clift, R.; Grace, J.; Weber, M. *Bubbles, Drops, and Particles*. Academic Press, New York **1978**.
- Dickens, G. R.; O’Neil, J. R.; Rea, D. K.; Owen, R. M. Dissociation of oceanic methane hydrate as a cause of the carbon-isotope excursion at the end of the Paleocene. *Paleoceanography*, *10*, **1995**, 965–971.

- Gangstø, R.; Haugan, P. M.; Alendal, G. Parameterization of drag and dissolution of rising CO₂ drops in seawater. *Geophys. Res. Lett.*, 32, **2005**, L10612, doi:10.1029/2005GL022637.
- Haljasmaa, I. V.; Viperman, J. S.; Lynn, R. J.; Warzinski, R. P. Control of a fluid particle under simulated deep-ocean conditions in a high-pressure water tunnel. *Rev. Sci. Instrum.*, 76, **2005**, 025111.1–025111.11.
- Hesselbo, S. P.; Gröcke, D. R.; Jenkyns, H. C.; Bjerrum, C. J.; Farrimond, P.; Morgans Bell, H. S.; Green, O. R. Massive dissociation of gas hydrate during a Jurassic oceanic anoxic event. *Nature*, 406, **2000**, 392–395.
- Hirai, S.; Okazaki, K.; Araki, N.; Yazawa, H.; Ito, H.; Hijikata, K. Transport phenomena of liquid CO₂ in pressurized water flow with clathrate hydrate at the interface. *Energy Convers. Manage.*, 37, **1996**, 1073–1078.
- House, K. Z.; Schrag, D. P.; Harvey, C. F.; Lackner, K. S. Permanent carbon dioxide storage in deep-sea sediments. *Proc. Natl. Acad. Sci. U.S.A.*, 103, **2006**, 12291–12295.
- Hove, J.; Haugan, P. M. Dynamics of a CO₂-seawater interface in the deep ocean. *J. Mar. Res.*, 63, **2005**, 563–577.
- International Maritime Organization (IMO). 1996 Protocol to the Convention on the Prevention of Marine Pollution by Dumping of Wastes and Other Matter, 1972 (as amended 2006) **2006**.
- Judd, A. G. The global importance and context of methane escape from the seabed. *Geo-Mar. Lett.*, 23, **2003**, 147–154.
- Kennett, J. P.; Cannariato, K. G.; Hendy, I. L.; Behl, R. J. Carbon isotopic evidence for methane hydrate instability during Quaternary interstadials. *Science*, 288, **2000**, 128–133.
- Kvenvolden, K. A. A primer on the geological occurrence of gas hydrates. In Henriot, J. P.; Mienert, J. (eds.), *Gas Hydrates: Relevance to World Margin Stability and Climate Change*, vol. 137. Geological Society London, London **1998**, 9–30.

- Leifer, I.; Patro, R. K. The bubble mechanism for methane transport from the shallow seabed to the surface: A review and sensitivity study. *Cont. Shelf Res.*, **22**, **2002**, 2409–2428.
- Lelieveld, J.; Crutzen, P. J. Changing concentration, lifetime and climate forcing of atmospheric methane. *Tellus*, **50**, **1998**, 128–150.
- Lupton, J.; Butterfield, D.; Lilley, M.; Evans, L.; Nakamura, K.; Chadwick, W.; Resing, J.; Embley, R.; Olson, E.; Proskurowski, G.; Baker, E.; de Ronde, C.; Roe, K.; Greene, R.; Lebon, G.; Young, C. Submarine venting of liquid carbon dioxide on a Mariana Arc volcano. *Geochem. Geophys. Geosyst.*, **7**.
- Maini, B. M.; Bishnoi, P. R. Experimental investigation of hydrate formation behaviour of a natural gas bubble in a simulated deep sea environment. *Chem. Eng. Sci.*, **36**, **1981**, 183–189.
- McGinnis, D. F.; Greinert, J.; Artemov, Y.; Beaubien, S. E.; Wüest, A. Fate of rising methane bubbles in stratified waters: How much methane reaches the atmosphere? *J. Geophys. Res.*, **111**, **2006**, C09007, doi:10.1029/2005JC003183.
- Milkov, A. V. Global estimates of hydrate-bound gas in marine sediments: how much is really out there? *Earth-Sci. Rev.*, **66**, **2004**, 183–197.
- Ozaki, M.; Minamiura, J.; Kitajima, Y.; Mizokami, S.; Takeuchi, K.; Hatakenaka, K. CO₂ sequestration by moving ships. *J. Mar. Sci. Technol.*, **6**, **2001**, 51–58.
- Paull, C. K.; Brewer, P. G.; Ussler, W. I.; Peltzer, E. T.; Rehder, G.; Clague, D. An experiment demonstrating that marine slumping is a mechanism to transfer methane from seafloor gas-hydrate deposits into the upper ocean and atmosphere. *Geo-Mar. Lett.*, **22**, **2003**, 198–203.
- Rehder, G.; Brewer, P.; Peltzer, E. T.; Friederich, G. Enhanced lifetime of methane bubble streams within the deep ocean. *Geophys. Res. Lett.*, **29**, **2002**, 1731, doi:10.1029/2001GL013966.
- Rehder, G.; Keir, R. S.; Suess, E.; Rhein, M. Methane in the northern Atlantic controlled by oxidation and atmospheric history. *Geophys. Res. Lett.*, **26**, **1999**, 587–590.

- Sakai, H.; Gamo, T.; Kim, E. S.; Tsutsumi, M.; Tanaka, T.; Ishibashi, J.; Wakita, H.; Yamano, M.; Oomori, T. Venting of Carbon-Dioxide Rich Fluid and Hydrate Formation in Mid-Okinawa Trough Backarc Basin. *Science*, **248**, **1990**, 1093–1096.
- Sato, T.; Jung, R.-T.; Abe, S. Direct simulation of droplet flow with mass transfer at interface. *J. Fluids Eng.*, **122**, **2000**, 510–516.
- Schlitzer, R. Ocean Data View **2007**.
- Shitashima, K.; Maeda, Y.; Koike, Y.; Oshumi, T. Natural analogue of the rise and dissolution of liquid CO₂ in the ocean. *Int. J. Greenhouse Gas Control*, **2**, **2008**, 95–104.
- Sloan, E. D.; Koh, C. A. *Clathrate hydrates of natural gases.*, vol. 119 of *Chemical Industries*. CRC Press, New York, 3rd ed. **2008**.
- Sun, R.; Duan, Z. H. Prediction of CH₄ and CO₂ hydrate phase equilibrium and cage occupancy from ab initio intermolecular potentials. *Geochim. Cosmochim. Acta*, **69**, **2005**, 4411–4424.
- Tishchenko, P.; Hensen, C.; Wallmann, K.; Wong, C. S. Calculation of the stability and solubility of methane hydrate in seawater. *Chem. Geol.*, **219**, **2005**, 37–52.
- Tsouris, C.; Brewer, P. G.; Peltzer, E. T.; Walz, P.; Riestenberg, D.; Liang, L.; West, O. R. Hydrate composite particles for ocean carbon sequestration: Field verification. *Environ. Sci. Technol.*, **38**, **2004**, 2470–2475.
- Zhang, Y. Fate of rising CO₂ droplets in seawater. *Environ. Sci. Technol.*, **39**, **2005**, 7719–7724.
- Zhang, Y.-X. Methane escape from gas hydrate systems in marine environment, and methane-driven oceanic eruptions. *Geophys. Res. Lett.*, **30**.

A Supporting Information to Chapter 2

Methane hydrate dissolution rates in undersaturated seawater under controlled hydrodynamic forcing

Nikolaus K. Bigalke, Gregor Rehder, Giselher Gust

2 Pages

List of auxiliary materials to the article:

Section A.1 Preparation of the experiments

A.1 Preparation of the experiments

The experimental chamber was filled with a scaled amount of artificial seawater (Tropic Marin) of a salinity of 35.0 PSU. Before mounting the experimental chamber and its periphery into the autoclave, the system was repeatedly flushed with methane gas to remove all air from the tubing and any remaining cavities. After closing the autoclave, a pressure of 10 MPa was established. The internal 400 mL storage cylinder was filled from an external high pressure methane supply. Downward motion of a motor-driven piston transferred the gas out of the internal storage cylinder into the microcosm through a bore-hole in the lid of the chamber (*Gust et al., in prep.*). Water being displaced during this process entered the flexible pouch attached to the bore-hole in the bottom of the microcosm. The fill level of the microcosm was controlled optically via camera mounted at the outside wall of the microcosm. The filling procedure was repeated until a total volume of 600 mL of gas (10 MPa) was fed to the microcosm. The gas accumulated under the lid of the microcosm, generating a smooth, even interface with the underlying seawater (cf. Figure 2.1). Pressure was raised to 35 MPa at which the system was left for a few

minutes to equilibrate the heat set free during the compression. To trigger hydrate formation, the system was depressurized to 20 MPa within a time frame of approximately 20 s. Hydrate formation started from isolated islands at the liquid/gas interface and spread at a rate of approximately 0.05 cm/s. The hydrate layer could be easily identified as an opaque cover on the seawater (cf. Figure 2.1). During these first steps, system temperature varied between 11 and 14 °C, depending on ambient conditions. Subsequently, the system was brought to the P -/ T -coordinates selected for the experiment. P and T could be controlled to a precision of ± 0.1 bar and ± 0.1 °C, respectively. Steady experimental temperatures were reached within a time frame of 12 h.

B Supporting Information to Chapter 3

Experimental investigation of the rising behavior of CO₂ droplets in seawater under hydrate forming conditions

Nikolaus K. Bigalke, Gregor Rehder, Giselher Gust

4 Pages, 2 Figures

List of auxiliary materials to the article:

- Section B.1** Description of experimental set-up and mode of operation
- Section B.2** Procedure involving the optical measurement of CO₂ droplets
- Section B.3** Aspect ratios of liquid CO₂ droplets rising within the field of hydrate stability.

B.1 Description of experimental set-up and mode of operation

A schematic diagram of the inner assembly is shown in Figure B.1. A 100 cm long, 10 cm i.d. acrylic glass tube served as rising chamber for the CO₂ droplets. Tapering attached on top of the tube focused the droplets to a rectangular 2 cm x 2 cm wide conduit. CO₂ entered the rising chamber through a 0.5 mm orifice of PTFE placed axially at the bottom of the rising tube. Two monochromatic PAL cameras (25 frames/s, 628 x 582 pixels, 51° x 43° field of view) in a pressure-resistant housing were installed next to the tube wall in a vertical distance of 34 cm from each other to monitor the ascent of the droplets. The distance between the lower camera and the nozzle was > 20 cm to allow droplets to reach their terminal rise velocities. The cameras were connected to an x86-platform PC equipped with a Matrox MOR-2VD video capture card for synchronous capturing and archiving of two uncompressed video streams. The acquisition software was written in C using Matrox

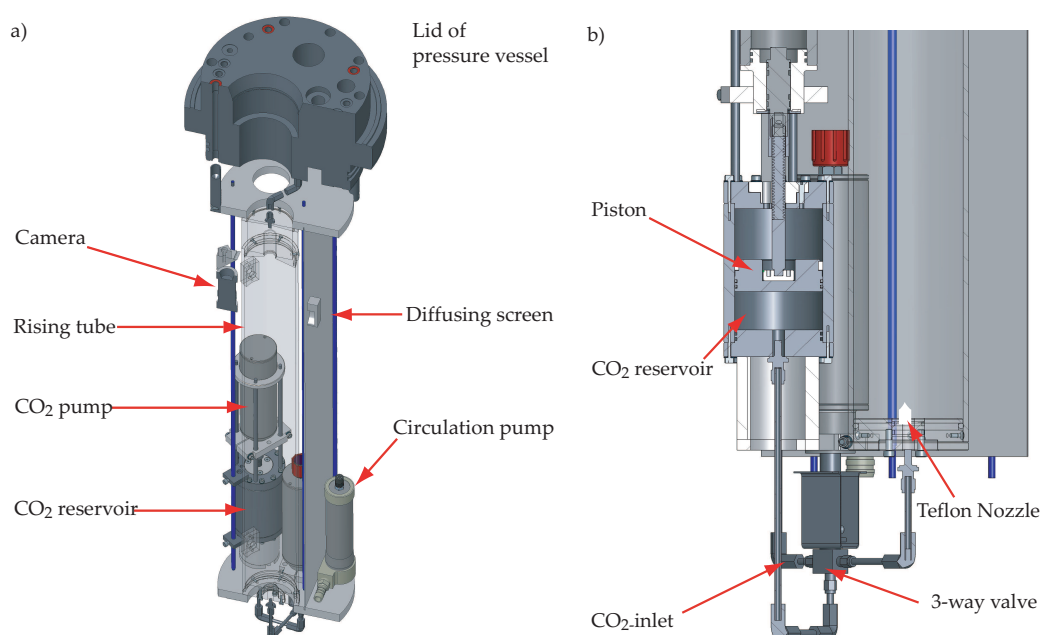


Figure B.1: Schematic diagram of the inner assembly. (a) Overview of the whole experimental set-up. (b) Detailed view of the CO₂ inlet system.

Imaging Library version 8.0. At the bottom of the rising tube a 90 cm scale was fixed to allow determination of the rise velocities of the droplets. For droplet size determination they were filmed a third time while passing through the narrow conduit at the top of the rising chamber. This filming was done through a sight glass in the lid of the pressure vessel with a Sony HDR-HC39P camcorder mounted externally on top of the lid. The optical path was deflected by two mirrors adjusted to ensure frontal imaging of the droplets. The camcorder recorded video streams on DV tape. In-focus images covered an area of 48 mm x 36 mm at a resolution of 768 pixels x 576 pixels. Illumination was provided by LED panels fixed oppositely of the three cameras, behind the rising tube. This caused droplets to appear as dark rings. A diffuser screen placed between light sources and rising tube evenly distributed the light across the cameras' field of view. Thermocouples inside and outside of the tube allowed temperature control to an accuracy of ± 0.1 K during experiments. A deep-sea rated pump recirculating the tap water within the pressure vessel was used to evenly distribute the temperature in the system. Pressure was controlled to an accuracy of ± 0.1 MPa. Pressure differences between rising chamber and au-

toclave were equilibrated by a 3 L flexible pouch connected to the rising chamber. Seawater of 35.0 PSU was produced from de-mineralized water and commercial sea salt (Tropic Marin) and used to fill the rising chamber of the inner assembly, which then was mounted in the pressure vessel. The system was sealed and left to cool down and equilibrate to experimental temperatures for more than 12 hours. Before raising the pressure to experimental conditions, liquid CO₂ was filled from an external dip-tube carbon dioxide container into the 400 mL stainless steel reservoir cylinder of the inner assembly. Transfer of CO₂ into the rising chamber was done by downward motion of a piston inside the cylinder (Figure B.1 b)). The piston was actuated by a deep-sea rated electric motor via threaded steel pin. The droplet size could be controlled by the speed of the downward moving piston. The aim was to continuously increase droplet radii from 0.75 mm radius initially to 10 mm at the end of an experiment. Time between generation of individual droplets was generally > 15 s. These measures were taken to minimize effects of a changed flow field acting upon a droplet's velocity.

B.2 Image analysis

Processing and analysis of the camcorder video was done using VirtualDub and ImageJ, which are available on the internet at <http://www.virtualdub.org> and <http://rsb.info.nih.gov/ij>, respectively. The procedure in general conforms to Leifer et al. (2003). The images were recorded by interlacing and had to be extracted. In each frame, field 2 was discarded and replaced by bi-cubic interpolation. From each video stream, a background frame was subtracted to level out uneven illumination and to remove scale markings fixed to the 2 cm × 2 cm rectangular conduit. Binary images were produced by thresholding a video five intensities below its average background intensity. Thus, droplets appeared as black and white rings. These were replaced by best fitting ellipses which were measured automatically.

B.3 Aspect ratios of droplets rising within the field of hydrate stability.

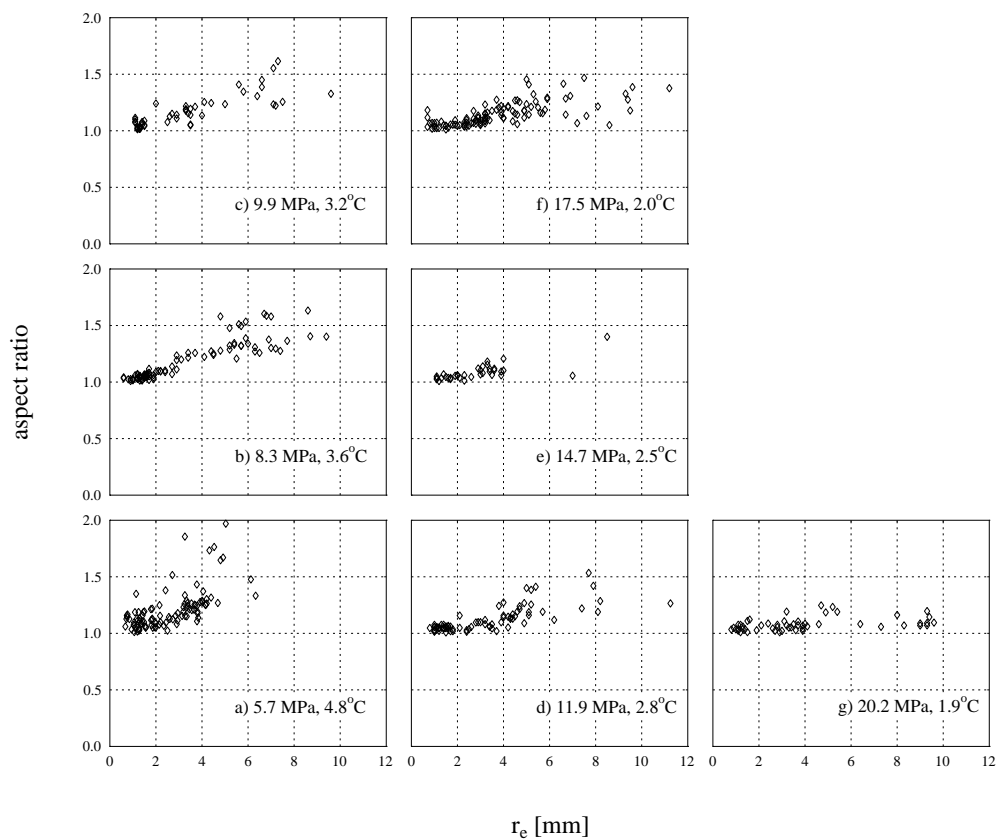


Figure B.2: Aspect ratios of droplets rising within the field of hydrate stability.

References

Leifer, I.; de Leeuw, G.; Kunz, G.; Cohen, L. H. Calibrating optical bubble size by the displaced-mass method. *Chem. Eng. Sci.*, **58**, 2008, 5211-5216.

Nikolaus Karl Bigalke

Adresse: Harmsstr. 84, 24114 Kiel
Tel: +49 179 730 2223
E-mail: nbigalke@ifm-geomar.de

Geburtsdatum: 30.12.1974
Geburtsort: Aachen
Staatsangehörigkeit: deutsch

- Juni 1995** Abitur am Ernst-Barlach-Gymnasium, Unna
- April 2000** Vordiplom in Mineralogie am Institut für Geowissenschaften der Christian-Albrechts Universität zu Kiel
- Dezember 2004** Diplom in Geologie-Paläontologie am Institut für Geowissenschaften der Christian-Albrechts Universität zu Kiel
- seit April 2005** Wissenschaftlicher Angestellter am Leibniz-Institut für Meereswissenschaften an der Christian-Albrechts Universität zu Kiel